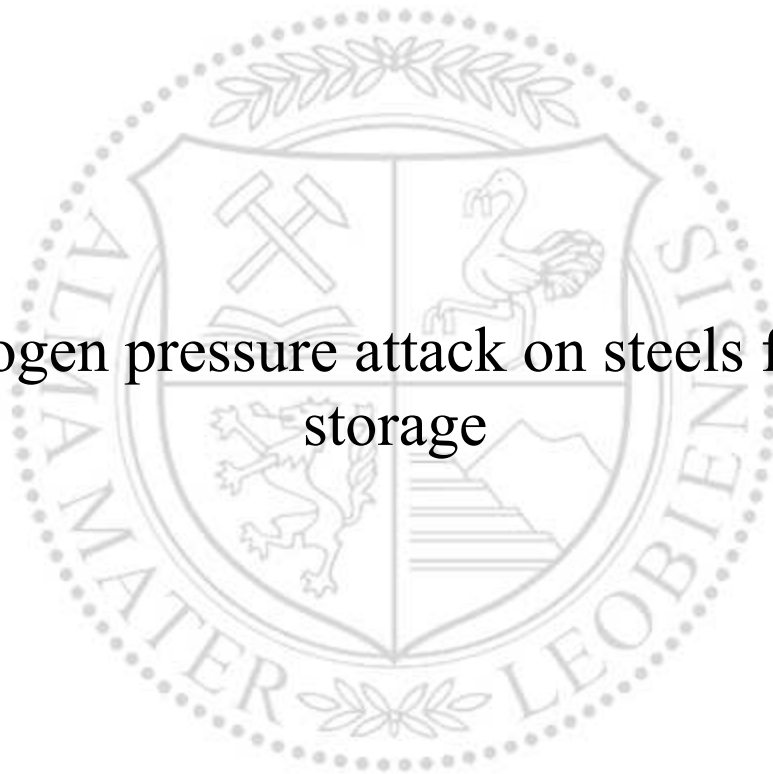Chair of General and Analytical Chemistry

Doctoral Thesis

Hydrogen pressure attack on steels for gas storage

Dipl.-Ing. Bernd Loder, BSc

July 2023

AFFIDAVIT

I declare on oath that I wrote this thesis independently, did not use other than the specified sources and aids, and did not otherwise use any unauthorized aids.

I declare that I have read, understood, and complied with the guidelines of the senate of the Montanuniversität Leoben for "Good Scientific Practice".

Furthermore, I declare that the electronic and printed version of the submitted thesis are identical, both, formally and with regard to content.

Date 06.07.2023

_____
Signature Author
Bernd Loder

Kurzfassung

Im Zuge des Horizon 2020-Projekts HyStories wird europaweit die Möglichkeit der Wasserstoffspeicherung in alten, erschöpften Erdgaslagerstätten und Erdgasspeichern untersucht. Im Rahmen dieses Projekts hat sich das Arbeitspaket "Materialien und Korrosion" zum Ziel gesetzt, die Einsetzbarkeit ausgewählter Rohrmaterialien im Hinblick auf Wasserstoffversprödung zu testen. Zu diesem Zweck wurden verschiedene Kohlenstoffstähle, darunter auch geschweißte Stahlgüten, sowie korrosionsbeständige Werkstoffe mit Hochdruck-Hochtemperatur-Autoklaventests, Permeationstests und Analysen des absorbierten Wasserstoffs untersucht. Die Autoklavenversuche umfassten Zugproben, die mit einer Feder bei 90 % der Streckgrenze belastet wurden sowie unbelastete Proben zur Bestimmung der Wasserstoffabsorption. Nach Abschluss der Tests wurde die Wasserstoffaufnahme durch thermische Desorptionsspektroskopie analysiert. Für die Autoklaventests wurden vier Hauptgaszusammensetzungen verwendet: 120 bar H_2, 120 bar H_2 + 15 bar CO_2, 120 bar H_2 + 1 bar H_2S und 120 bar H_2 + 15 bar CO_2 + 1 bar H_2S. Die Experimente wurden trocken und mit Elektrolyten mit unterschiedlicher Salinität durchgeführt. Die Prüfungen erfolgten bei Raumtemperatur und 120 °C sowie einer Versuchsdauer von 720 Stunden. Vor den Autoklavenversuchen wurde der effektive Diffusionskoeffizient bestimmt, um das Diffusionsverhalten von Wasserstoff durch die untersuchten Stahlgüten zu charakterisieren. Die Ergebnisse der Autoklaventests zeigen, dass die Wasserstoffaufnahme auch unter scharfen Bedingungen relativ hoch ist. Dennoch führte eine konstante Belastung der Proben nur beim gehärteten Material sowie beim Duplex 2205 zum Werkstoffversagen. Keiner der anderen Werkstoffe wies am Ende der Prüfung Risse oder andere Formen mechanischer Schädigung auf. Außer bei den hochfesten Kohlenstoffstählen kam es unter scharfen Bedingungen zu einem lokalisierten Korrosionsangriff. Es wurden Anwendungsgrenzen für alle getesteten Werkstoffe für den Einsatz in unterirdischen Wasserstoffspeichern festgelegt.

Abstract

The possibility of hydrogen storage in various types of caverns and depleted reservoirs is currently under investigation in whole Europe. One of the projects dealing with this topic is HyStories. The investigation of the applicability of various pipe materials with regard to hydrogen embrittlement was one of the tasks of this project and is the focus of this work. For this purpose, various carbon steels, including welded steel grades, as well as corrosion-resistant materials were investigated with high-pressure high-temperature autoclave tests, permeation tests and analyses of the absorbed hydrogen. The autoclave tests included tensile specimens loaded with a spring at 90% of yield strength and a unloaded sample was examined to determine hydrogen absorption. After successful conduction of the tests, hydrogen uptake was analyzed by thermal desorption spectroscopy. Four main gas compositions were investigated in the autoclave tests: 120 bar H_2, 120 bar H_2 + 15 bar CO_2, 120 bar H_2 + 1 bar H_2S and 120 bar H_2 + 15 bar CO_2 + 1 bar H_2S. Test were done in dry conditions as well as with the addition of electrolytes with varying salinity. In addition, the tests were carried out at room temperature and 120 ° C. The duration of the experiments was 720 hours. Before the autoclave test, the effective diffusion coefficient was determined to characterize the diffusion behavior of hydrogen by selected steel grades. The results of the autoclave tests show that hydrogen absorption is relatively high even under severe conditions. Nevertheless, constant loading of the samples led to material failure only in the case of the quenched material and Duplex 2205. None of the other materials showed cracks or other forms of mechanical damage, except for the high-strength carbon steels, some localized corrosion attack occurred under sharp conditions. For this reason, application limits were defined for all tested materials for use in underground hydrogen storage.

Acknowledgment

Last but not least, I would like to mention my family, who have supported me a lot throughout my time in Leoben.

Table of contents

1 Introduction

In corrosive environmental conditions, mechanical properties of metallic materials can significantly decrease. At the Chair of General and Analytical Chemistry, there are individual experimental investigation and analysis methods available for the evaluation of various materials under the influence of high pressure hydrogen. Hydrogen technologies will facilitate decarbonization, as a consequence research in this field will play an essential role for hydrogen storage. Therefore, it is important to progress research in this area to counter hydrogen embrittlement (HE). The highest susceptibility of steels to hydrogen embrittlement is at room temperature, although hydrogen uptake from the gas phase increases sharply at higher temperatures [1]. Increased hydrogen absorption due to the presence of an electrolyte was also previously reported in the literature. Other influencing factors mentioned are the hydrogen partial pressure, pH value of the electrolyte and the presence of a recombination inhibitor [2].

The possibility of hydrogen storage in depleted natural gas reservoirs and natural gas storage facilities was evaluated for many locations in the European Union within EU project HyStories. The aim of project, work package Materials and Corrosion was to test the resistance of selected pipe materials to hydrogen embrittlement by performing autoclave tests, analysing the diffusion and trapping behaviour of steels and investigate fatique behavior(the later by Institute de la Corrosion, Brest).

A scheme of underground hydrogen storages (UHS) is illustrated in Figure 1. While pure hydrogen storage has been carried out in salt caverns in Europe since the 1970s, the storage of pure hydrogen in depleted fields or aquifers has not been carried out before anywhere. The Hystories project partners investigated the potential of aquifers and depleted fields for UHS [3].
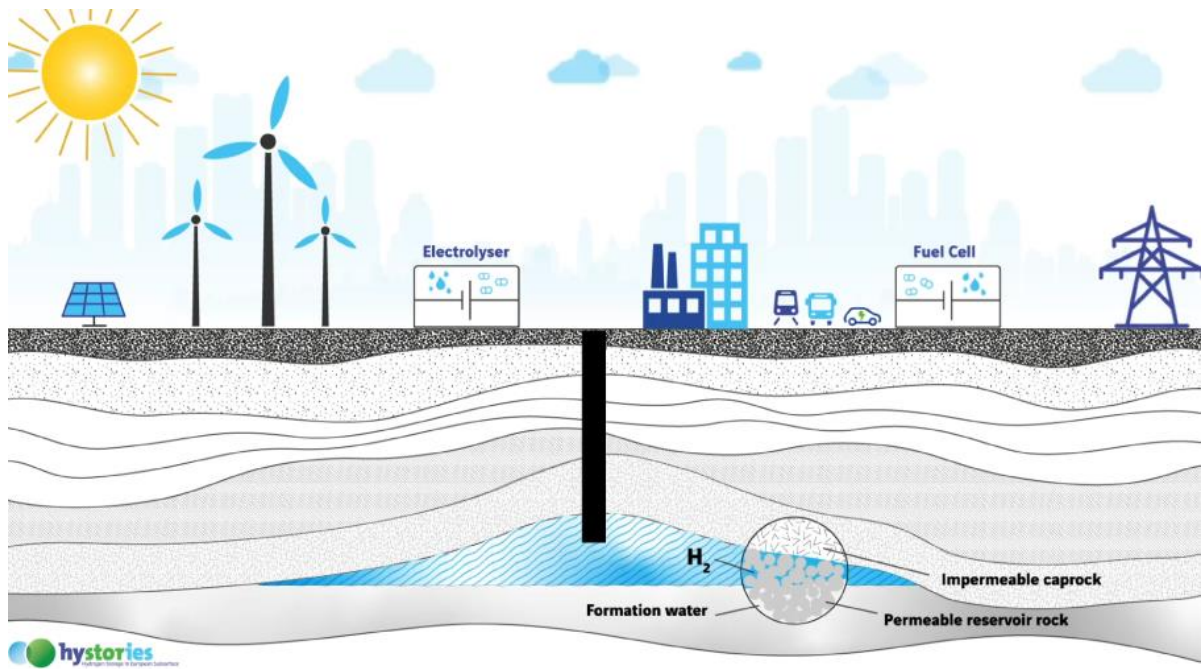
Figure 1: Schematic illustration of modification of underground gas storage for hydrogen [3]

The main research questions for this thesis are:

Are the materials used in gas storage sites resistant to hydrogen embrittlement under the operating conditions encountered and what are their susceptibility limits?

Why are certain materials more susceptible than others?

2 Theoretical overview

Hydrogen is the most abundant element in the Universe, but does not occur in its elemental form on Earth [4]. Due to the need of stopping global warming, there is a tremendous driving force to develop renewable energy technologies. Climate neutrality initiatives are being implemented worldwide, aiming to reduce greenhouse gas emissions to zero by 2050. In 2022, global energy-related CO_2 emissions increased by 0.9 % or 321 million tons (Mt), reaching a new record of 36.8 giga tons (Gt). After two years of exceptional fluctuations in energy consumption and emissions, partly caused by the Covid 19 pandemic, last year's growth was much lower than the increase of over 6 % in 2021. These CO_2 emissions can be separated as follows and amounted to 15.65 Gt CO_2 from electricity generation, 9.15 Gt CO_2 from industry, 7.98 Gt CO_2 from transport, 2.97 Gt CO_2 from the building sector and 1.14 Gt for all other sectors. Several initiatives have been proposed to reduce these emissions. The energy mix will face a considerable increase of shares of renewable energies such as wind power, solar power, geothermal power and biomass. The share of water power is believed to stay constant over next decades due to limited access of dams for rivers. By 2050 total amount of renewable energies will exceed fossil fuels worldwide to teach the Paris goals. Around 90 % of the global electricity growth is generated from renewable energies. Renewable energy, including solar, wind, biofuels and others, are in the focus of this transition from fossil fuels to a lower-carbon and more sustainable energy system. The generation of solar and wind energy increased by around 275 TWh in both cases, helping to avoid around 465 Mt of emissions in the power sector. In 2022, global water-powered electricity generation increased by 52 TWh compared to the previous year [5–9].

Currently, hydrogen is becoming a new and widely accepted part of many national and international climate strategies. For this reason, various industrial processes are being investigated for the production of hydrogen, which release different amounts of CO_2 depending on the technology used [10]. Water is the cheapest and most renewable raw material in the electrolysis process, which has been strongly developed in the last few years.

There are many uses for hydrogen, which can be seen in Figure 2. Hydrogen is used in chemical industry for production of ammonia and methanol, in metallurgical industry for reduction of specific metals such as molybdenum and tungsten, and in the petrochemical industry. Furthermore it is often applied in the refining process in the refinery sector and is also used for production of hydrogen peroxide [11]. In 2018, the EU consumed 8.3 million t of hydrogen that is 13 % of the global production, mainly in refineries (3.7 million t or 45 % of the total) and in the chemical sector mainly for the production of ammonia (2.8 million t or 34 %) and methanol (12 %). Nearly 100% of the hydrogen produced in the EU today is "grey" hydrogen; only less than 1% of the production is renewable hydrogen [12].
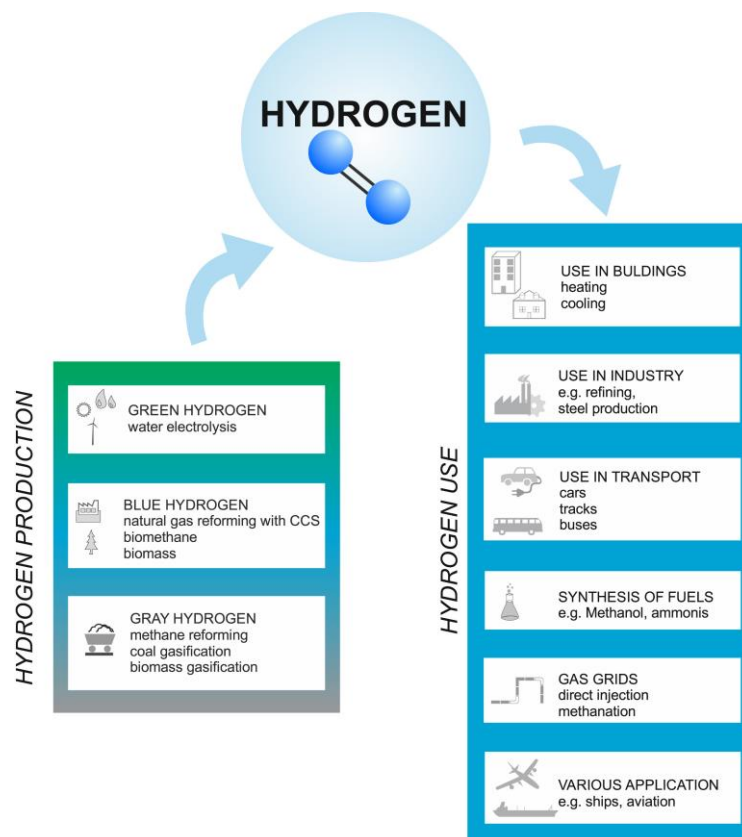
Figure 2: Hydrogen production and its use [13]

Hydrogen is available in abundance and it occurs almost exclusively as part of another compound, like water H_2O or methane CH_4. Its color refers to the method the pure H_2 is produced. Figure 3 shows a diagram of the different hydrogen colors. Green hydrogen is defined as hydrogen produced using electricity generated by a combination of renewable energy sources and a water electrolyser [14]. An electrolyser processes pure water by means of electricity to hydrogen and oxygen [10]. At the moment, natural gas reforming, steam methane reforming (SMR), is the typical method to produce blue and grey H_2. This method of the blue H_2 production has an energy efficiency of 65 to 85 % [9,15]. Blue hydrogen is generated from fossil fuels coupled with carbon capture and storage (CCS) technologies to reduce a large portion of greenhouse gas (GHG) emissions. Therefore blue hydrogen is more cost effective than green hydrogen, and the implementation of CCS results in technical challenges in addition to those

related to social acceptance. There is no standard definition for the CO_2 capture rate required to classify grey and blue hydrogen. Grey H_2 is produced from natural gases, usually methane, by a process called steam methane reforming. Turquoise hydrogen is produced from methane pyrolysis. In the USA mainly brown hydrogen is produced. This is the most conventional way by generating hydrogen from either black or brown coal. This releases large amounts of CO_2 and carbon monoxide into the atmosphere. These methods generate clean, emission-free hydrogen fuel, but they generate significant amounts of CO_2, which are warming the earth, so they are less than optimal for a truly clean future for hydrogen. There are also other technologies of production that are not so well known although they should be mentioned. The orange H_2 is produced from bioenergy. The pink H_2 is generated by electrolysis from nuclear energy. White H_2 is naturally produced hydrogen that occurs in underground deposits and can be extracted by fracking. Yellow H_2 is a form of green H_2 which is produced by the process of electrolysis using solar energy [10,14,16].
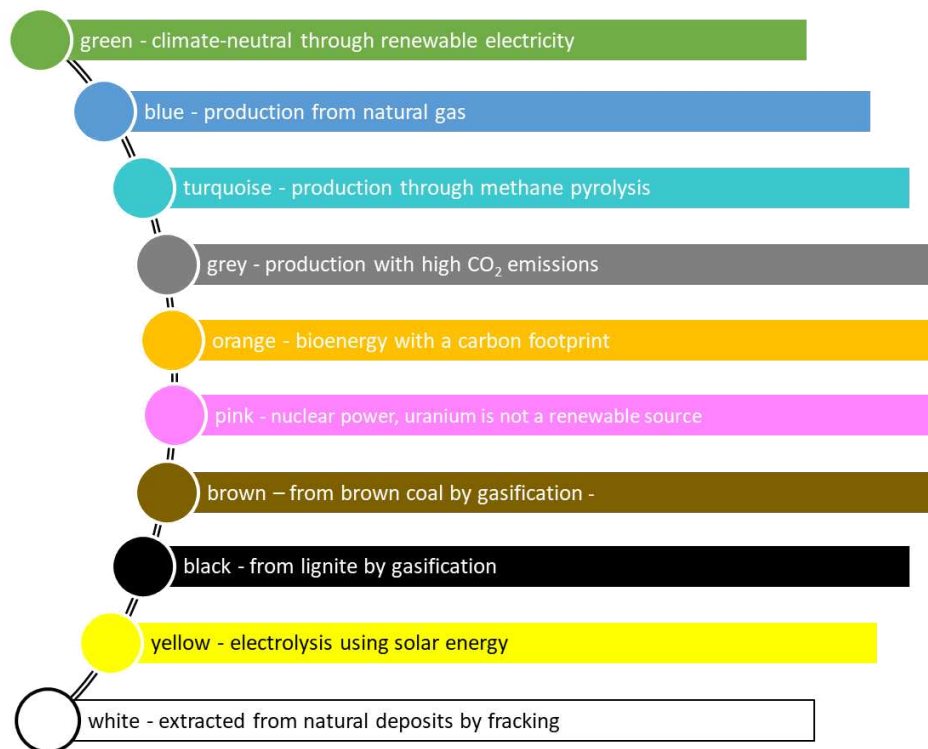
Figure 3: The colors of hydrogen, modified from [17]

Regarding the distribution of the forms of energy used in modern times, a clear trend can be seen in Figure 4. The civilization is performing a transition from carbon based, chemically complex energy systems to cleaner, chemically simpler, sustainable energy systems. By 2050 hydrogen is believed to replace natural gas and solid fuels as the main energy source. Nevertheless a certain portion of fossil fuels will remain important until the mid of the century. It is expected to find large applications for hydrogen in the chemical industry, metallurgy, transport and in long term also in aerospace and marine sectors [13,18].

In Figure 4 a currently realistic time schedule of the energy transition is shown indicating that peak oil has closely passed or is soon to be passed.

Figure 4: Energy transition from 1850 to 2150, hydrogen can possibly replace fossil energy carriers [13], based on [18]

In order to push the green energy to the next level, more hydrogen storage facilities are needed. This is an essential component for the success of hydrogen as a future energy source. It is of major importance that a reliable storage system is available for the respective application to meet the hydrogen market and possible future demand. Hydrogen has roughly only one third of the calorific value of methane and a much lower portion when compared to liquid and sol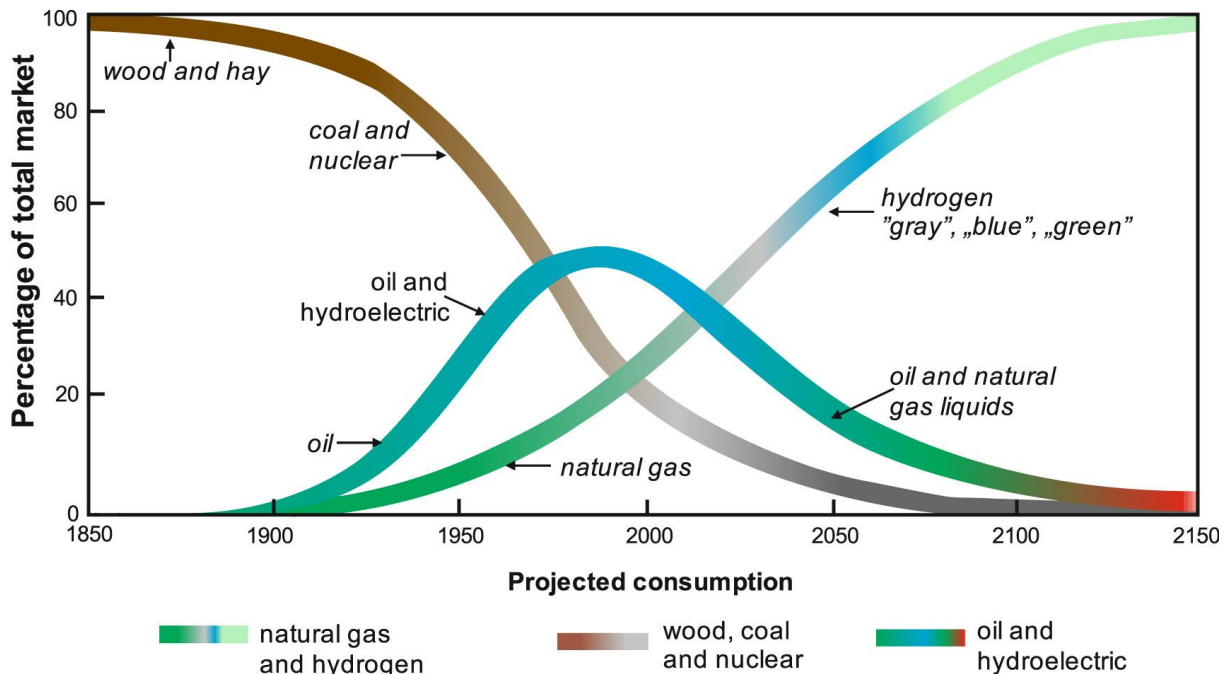id fossil fuels [19-21]. The density of hydrogen gas is the lowest of all molecules, and at ambient pressure and temperature, 1 kg of the hydrogen gas occupies up to 11 m^3 [22]. Therefore, the storage density of hydrogen has to be increased to make it economically usable and an appropriate storage method in large quantities (three times larger than for natural gas currently existing) has to be found. Several techniques are available for storage of hydrogen at higher densities. All these methods require some kind of energy input. The hydrogen storage systems can be categorized into two main groups the material-based and the physically-based hydrogen storage systems (Figure 5). The physical hydrogen storage involves compressed gas storage, liquid H_2 storage and cryo-compressed storage [20,21]. In material-based storage, hydrogen molecules are split into atoms and enter into the chemical structure of materials such as metals or some organic substances. Among all materials that can be applied for chemisorption, metal hydrides are known best [23,24].
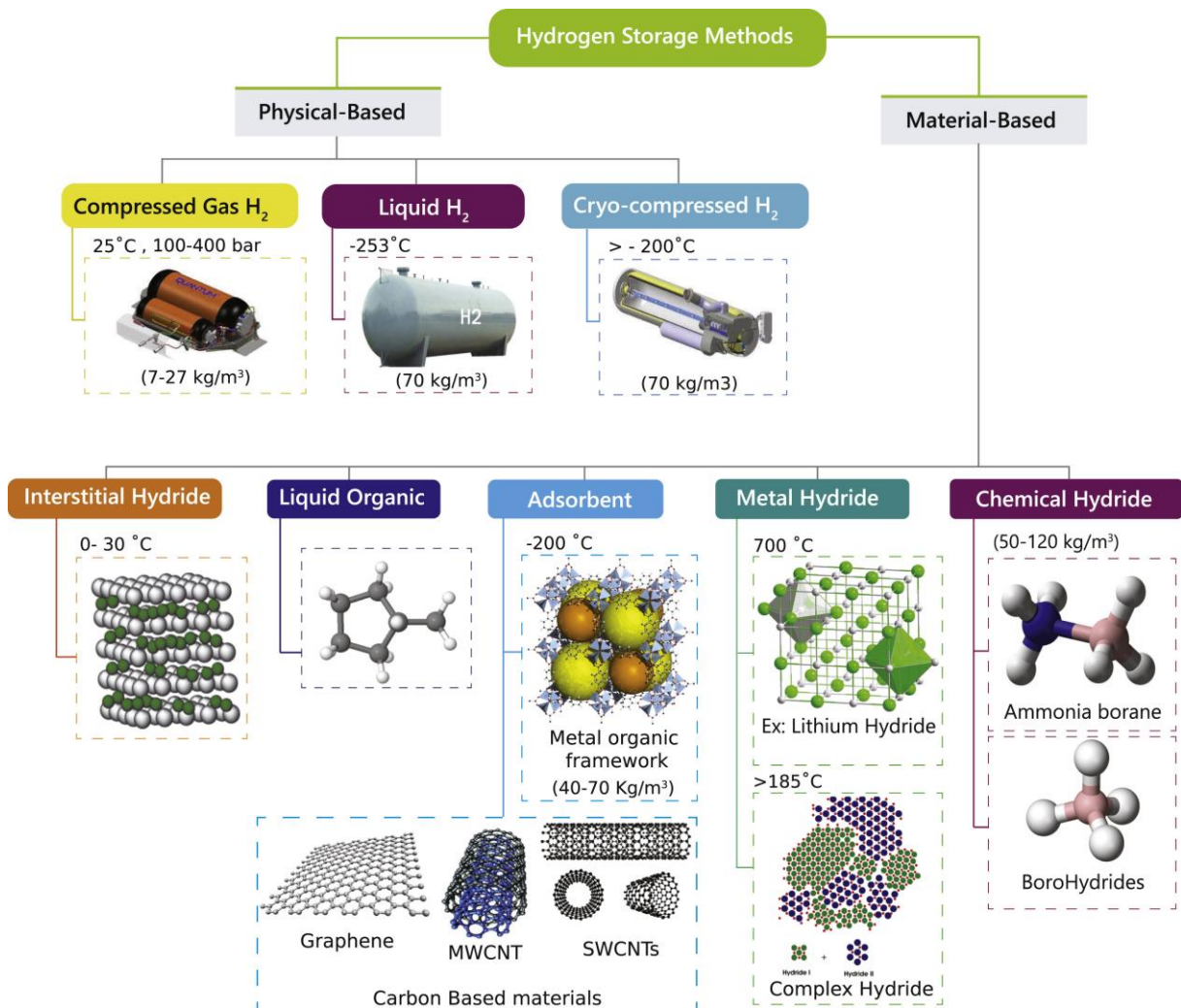
Figure 5: Hydrogen can be stored in physical based (compressed H₂, liquid H₂ and cryo compressed H₂) or material based (Hydrides, Liquid organics and adsorbed materials) methods [23]

An improved volumetric hydrogen storage capacity can be expected in material-filled gas cylinders compared to cylinders without any materials, taking into consideration of the adsorption effect. The storage system is based either on physisorption for porous materials and on chemisorption in the case of metal hydrides. The physisorption implies a weaker binding energy and weak van der Waals forces, whereby the chemisorption implies a stronger binding energy. In the case of complex hydrides and metal hydrides, hydrogen molecule first dissociates at the surface and subsequently diffuses into the metal lattice in its atomic state [25].

Because of the low interaction energy and the fast adsorption and desorption kinetics, physisorption processes are easier to handle than chemisorption processes [26]. As Broom [27] considered, hydrogen is physically adsorbed on the surface of pores in porous materials such as zeolites, porous carbon structures and metal-organic frameworks (MOFs) and the capacity is mainly influenced by the surface area, pore volume, pressure and

temperature. At cryogenic temperatures at 77 K and high pressures, many physisorption-based materials have acceptable hydrogen storage capacities. At room temperature and pressures between 50 and 100 bar, their capacities decrease to less than 1 wt%. So a further issue requiring clarification is the economic sustainability of hydrogen storage by physisorption at cryogenic temperatures. 6 kilograms of hydrogen produce 30 MJ of heat when the binding energy of hydrogen on the surface of a given material is $10 \text{ kJ} \cdot \text{mol}^{-1} \text{ H}_2$. If liquid nitrogen is being used to maintain the temperature at 77 K and the heat of vaporization is $5.6 \text{ kJ} \cdot \text{mol}^{-1}$, 5400 mol N_2 (150 kg) is circulating in the cylinder. Using such a large amount of liquid nitrogen for cooling purposes would be problematic for engineering. The synthesis of hydrogen compounds often takes place under increased hydrogen pressure as a result of chemisorption with larger binding energies, and heat is generated in the exothermic reaction. For hydrogen release a lower pressure is adjusted and the system is heated to higher temperatures. The gravimetric hydrogen storage capacity of some metal hydrides is less than 3 wt.%, although they can operate close to room temperature [28]. Some of the complex and light metal hydrides have significant gravimetric storage capacities, such as 7.6 wt.% for MgH_2 and 18 wt.% for $LiBH_4$. However, high temperatures are required for these hydrides to release their hydrogen. MgH_2, for example, requires a temperature of about 573 K. In the case of complex hydrides, the release of hydrogen is somewhat more complicated, requiring several steps at different temperatures [29]. In order to enable the storage of hydrogen in a solid-based system at room temperature with an acceptable storage density, different strategies were investigated and evaluated. In physisorption systems based on porous materials, the research focuses on improving hydrogen storage capacities at room temperature. In chemisorption systems based on metal/chemical hydrides, this research focuses on improving the kinetics and thermodynamics of the materials [30].
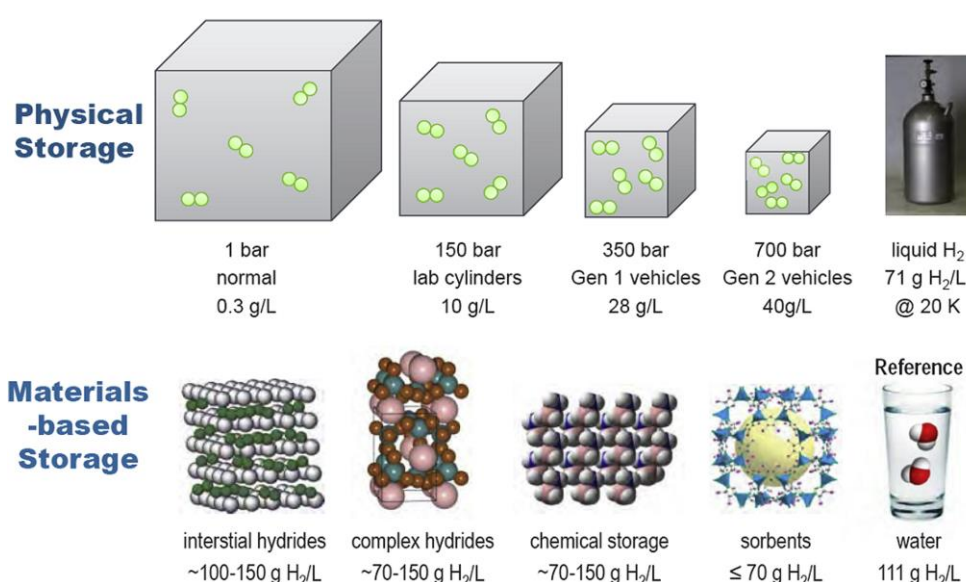

Figure 6: Compressed hydrogen in physical storage vs. material-based storage facilities with their corresponding storage capacities [31]

Compressed gas can be used, for instance, in tanks as illustrated in this chapter, but only for smaller quantities. For larger quantities, pipelines as well as natural storage facilities such as salt caverns, depleded fields or aquifers are used, which is explained in detail in chapter 2.4. To maximize energy efficiency, hydrogen can be safely transported and stored in large quantities. The impact of HE is more pronounced in the presence of increased hydrogen pressure [32].

Hydrogen as the smallest atom, may easily enter into metals and reduce their ductility, which is particularly apparent in steel. In 1874, Johnson had already investigated the remarkable changes in their mechanical properties of iron and steels when immersed in hydrogen and acids. With this work, he founded the field of HE research with many open questions remaining [33].

In compressed hydrogen gas, it is possible for HE to occur, however. For this reason, effects for hydrogen traps are described in more detail in the next chapters.

2.1   Hydrogen in steel

In the following chapter the absorption, diffusion, trapping and damage mechanisms of hydrogen in steel will be explained.

2.1.1   Hydrogen absorption

There are two major sources of hydrogen uptake in the material, one is compressed hydrogen gas and the other is electrolytes such as corrosive media [1]. Hydrogen occurs in nature mainly as gaseous H_2. The gas molecule is too large to cross the boundary between gas and metal or to diffuse interstitially through solid metals. Hydrogen can only in atomic form enter a metal. For metals exposed to a gaseous hydrogen atmosphere, the gas-solid interaction is described by three steps: Physisorption, chemisorption and absorption. The process is shown schematically in Figure 7 [34–36].
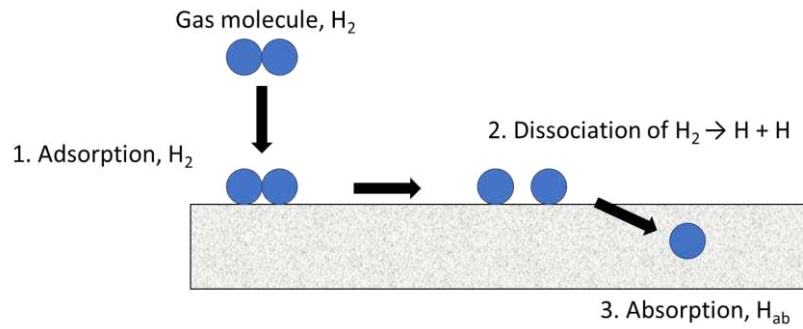
Figure 7: Steps of pressure hydrogen uptake into a metal, modified, original [37]

Van der Waals forces are the basis for physisorption, taking place between the metal surface and an adsorbed molecule. Physisorption is completely reversible and it is usually immediately effective. Chemisorption is a chemical reaction between a metal surface atom and the adsorption molecule. This sorption is generally slow and can be either reversible or irreversible. With the formation of covalent bonds between an atom or adsorbent molecule, this process can lead to direct dissociation of the molecules to atomic hydrogen. [36,38].

The hydrogen molecule is dissociated either directly or by surface diffusion following physisorption with subsequent dissociation. Dissociation is a chemical reaction and part of chemisorption. The reaction takes place if it is energetically more favorable to split H_2, which is still attracted to the metal surface due to the Van der Waals forces, into two individual atoms, which can now stick even closer to the surface [35,39,40]. The reaction equation of dissociation is known as Tafel reaction, see Eq. (1) [41,42]:

$$2M + H_2 \Leftrightarrow MH_{ads} + MH_{ads} \tag{1}$$

M denotes an atom of the metal surface and H_{ads} denotes a hydrogen atom that is adsorbed on the surface. Absorption is a gas-solid reaction in which the chemisorption products are diffused into the crystalline lattice of the steel. Hydrogen absorption can take place in atomic or ionic H^+ [36,38] state.

A metal's hydrogen solubility S can be calculated with the help of Sieverts' law, in Eq. (2) [43]:

$$S = S_0 \cdot \sqrt{p} \cdot e^{-\frac{\Delta H}{R \cdot T}} \tag{2}$$

with S_0 representing the solubility constant, p the hydrogen partial pressure, ΔH the enthalpy of solution, T the absolute temperature and R the general gas constant. Eq. (2) above describes pressure and temperature dependence of hydrogen solubility as first described by Sieverts [44]. The hydrogen solubility of pure iron as a function of temperature is shown in Figure 8. From this graph, it can be seen that the hydrogen solubility in liquid iron is very high. In solid iron, the solubility is higher in the γ form also known as austenite compared to the α form also often referred to as ferrite, bainite or martensite. In high temperature processes, a large amount of hydrogen can diffuse into the steel although only a low solubility of hydrogen in iron is given at room temperature

and cracking and embrittlement can happen. The solubility of a given material is a function of its microstructure and chemical composition [45].
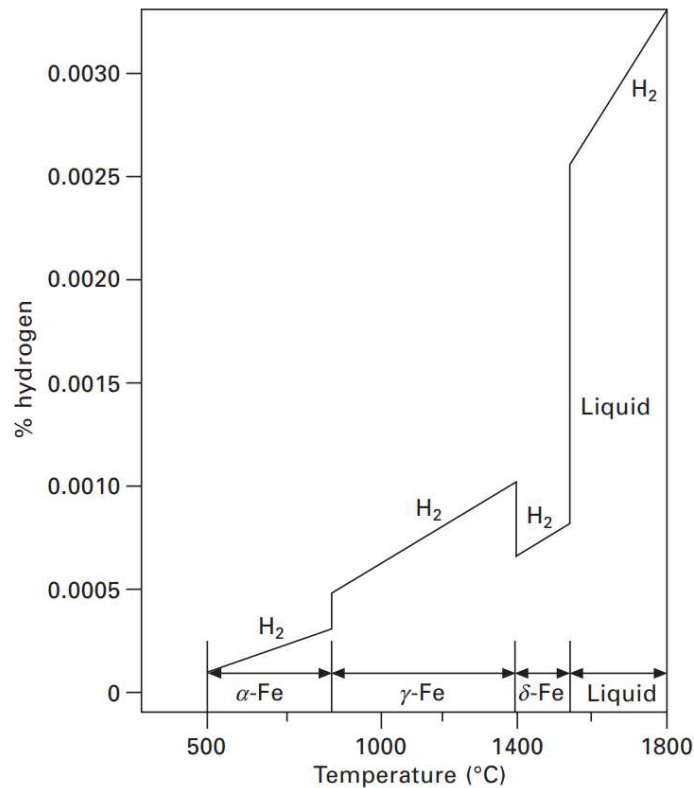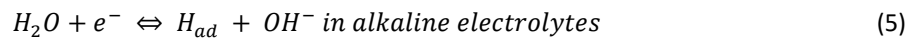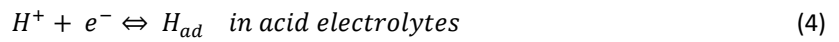

Figure 8: Hydrogen solubility of pure iron versus temperature, the H-content is given in wt.% [45]

Hydrogen stabilization of austenite has been found to not depend on the amount of hydrogen, but on the way, it is introduced into the austenite before it is transformed to martensite. Stabilization is understood as a decreasing tendency to martensite transformation. Due to the higher solubility in γ-Fe, the hydrogen stabilizes the austenite, which is shown by a decreasing tendency to martensite transformation. The test results show that with cathodic charging, austenite stabilization is clearly observable. At room temperature, the hydrogen solubility in pure iron is very low [46,47].

Hydrogen absorption in aqueous media, is the second important way of hydrogen absorption. While carbon steel absorbs less than 1 ppm hydrogen in 1 bar H_2 at room temperature, corrosion attack by acids, H_2S or simply water can result in hydrogen uptake of several ppm [37]. When metals are in solution during the corrosion process, they donate electrons (e-) during oxidation. The anodic partial reaction of this electrolytic corrosion of Fe is given in Eq. (3) [1]:

$$Fe + 2H^+ \rightarrow Fe^{2+} + 2H \tag{3}$$

In a redox reaction, a reduction must also take place at the cathode, which consumes the released electrons. In connection with hydrogen absorption and embrittlement, this is taken over by the partial reactions. The corrosion attack is mainly influenced by the first partial reaction the Volmer reaction, which is described in Eq (4) for acidic and (5) for neutral electrolytes below [1,48]:

$$H^+ + e^- \Leftrightarrow H_{ad} \quad in\ acid\ electrolytes \tag{4}$$

$$H_2O + e^- \Leftrightarrow H_{ad} + OH^- \ in\ alkaline\ electrolytes \tag{5}$$

where H_{ad} is the designation of the adsorbed hydrogen atom. Electrolytic hydrogen absorption takes place via the Volmer reaction, in this process, adsorbed, atomic hydrogen is formed on the metal surface by either an external, cathodic current or by a corrosion attack, which is absorbed into the material or recombines on the surface according to Tafel or Heyrovsky. The H_{ad} can then be absorbed by the material or reacts further by one of the two reactions according to Heyrovsky, for acidic and basic electrolytes, shown as Eq.s (6) and (7) [1,34,36,49]:

$$H_{ad} + H^+ + e^- \Leftrightarrow H_2 \ in\ acid\ electrolytes \tag{6}$$

$$H_{ad} + H_2O + e^- \Leftrightarrow H_2 + OH^- \ in\ alkaline\ electrolytes \tag{7}$$
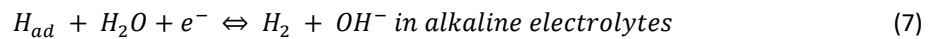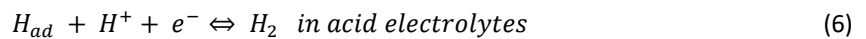
The adsorbed hydrogen atoms can also recombine into H_2 according to Eq. (1). This is also known as chemical desorption. H_2S acts as a recombination poison and promotes the Volmer reactions. Recombination inhibitors promote hydrogen uptake by inhibiting, the Tafel or Heyrovsky reaction [37]. The partial reactions can be seen in Figure 9 [1,34,50]:
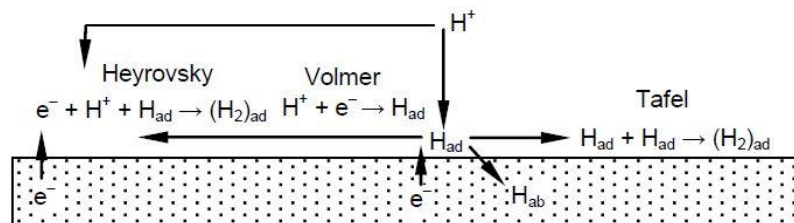

Figure 9: Three most Important reactions for the hydrogen uptake [51]

Hydrogen atoms are generated during corrosion in oil and gas by the help of H_2S and CO_2. The effect of the main corrosive species during storage in old reservoirs for gases containing H_2S and CO_2 and are given in the following Eq.s (8) to (10) [52]:

$$CO_2 + H_2O \Leftrightarrow H_2CO_3 \tag{8}$$

$$H_2CO_3 \Leftrightarrow H^+ + HCO_3^- \tag{9}$$

$$H_2S \Leftrightarrow H^+ + HS^- \tag{10}$$

Therefore, two types of corrosion are distinguished in tubing and casing materials: sweet corrosion in the presence of CO_2 and sour corrosion when H_2S is present. Sweet corrosion occurs in pipeline steels when CO_2 reacts with H_2O to produce carbonic acid. The dissociation of H_2CO_3 hydrogen ions for the cathodic reaction and lowers the pH. The second, but severe type of corrosion of pipeline steels takes place in the presence of H_2S [53-55].

H_2S dissociates into H^+ and HS^-. The HS^- ion acts as a hydrogen recombination poison and prevents the formation of hydrogen molecules [53–55].

H_2S accelerates the Volmer reaction and reduces the recombination rate, and increases the degree of surface coverage with hydrogen atoms [56]. Therefore, it is a strong promoter of hydrogen uptake and consequently hydrogen embrittlement. As shown in Figure 10, H_2S is stable especially at low pH values and thus effective as an electrode poison. When corrosion occurs in the presence of H_2S, the steel forms an iron sulfide layer (FeS), which can reduce hydrogen absorption [57–60].
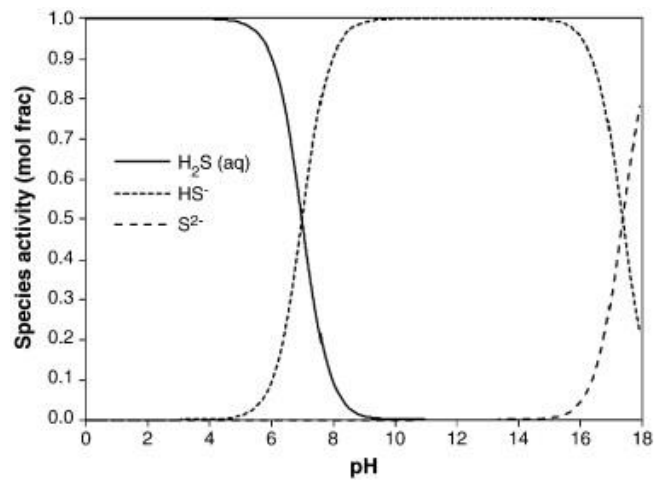

Figure 10: Species activity of H_2S, HS^- and S^{2-} as a function of the pH value [57]

In general a low pH value results in an increased absorption of hydrogen into the material, as illustrated in Figure 11 [52].
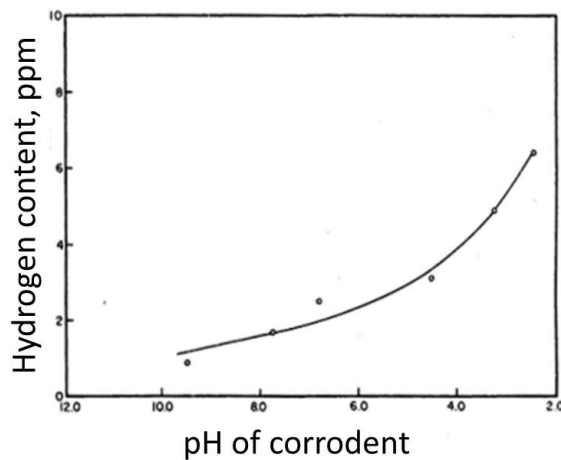

Figure 11: Influence of the pH value on the hydrogen content [61]

2.1.2 Hydrogen diffusion

For steels, it is important to understand hydrogen transport. Diffusion is affected by microstructure [62]. In 1855, Fick [63] found that a concentration gradient leads to a material flow that will attempt to compensate for this imbalance. He observed that the particle flux j_D in the present case of hydrogen flux is proportional to the concentration gradient, a relationship known as Fick's first law, see Eq. (11). In absence of hydrogen interactions with lattice defects, this can be described in a one dimensional formula as [64]:

$$j_D = -D \frac{d_c}{d_x} \tag{11}$$

where D is the diffusion coefficient, c is the concentration and x is the characteristic length. Diffusion's driving force is the concentration gradient, and hydrogen flow in metals is given by Fick's first law, in Eq. (11). Second Fick's law, for nonstationary diffusion, Eq. (12) explains the change of the hydrogen concentration into a volume. As the diffusivity is constant and is independent of location and concentration, the following applies [64,65]:

$$\frac{\partial c}{\partial t} = D \frac{\partial^2 c}{\partial x^2} \tag{12}$$

for multidimensional forms resulting in Eq. (13):

$$\frac{\partial c}{\partial t} = D\Delta c = D \left(\frac{\partial^2 c}{\partial x^2} + \frac{\partial^2 c}{\partial y^2} + \frac{\partial^2 c}{\partial z^2} \right) \tag{13}$$

where Δ is the Laplace operator and t is the time. In the equations, the diffusion coefficient is a value derived from the frequency of jumping of atoms in the crystal lattice, but macroscopically observed diffusion and transport of hydrogen is usually mediated by diffusion paths. Hydrogen atoms can be trapped in various lattice defects and detrapped, therefore Fick's laws must be modified for such processes. McNabb and Foster [66] provide a general formulation of diffusion involving trapping and detrapping. The effective diffusion coefficient (D_{eff}) is dependent on temperature and additionally is strongly influenced by microstructure, mainly by the distribution and density of the different traps [64,65].

For diffusion of hydrogen in pure and undeformed α-iron from 25 to 800 °C, D is of the order of $10^{-5} \frac{cm^2}{s}$ to $2 \cdot 10^{-4} \frac{cm^2}{s}$ compared to about 10^{-10} to $8 \cdot 10^{-4} \frac{cm^2}{s}$ for nickel from 25 to 1200 °C. The hydrogen diffusion rates in pure metals at room temperatures depend in particular on the crystal structure. The hydrogen diffusion coefficients D are generally four to five orders of magnitude higher for body-centred cubic (bcc) metals such as Cr, Mo, V, W, Nb or α-Fe compared to face-centred cubic (fcc) metals such as Cu, Ni or Al or hexagonal close-packed (hcp) metals such as Mg, Zn or Ti at room temperature, see Figure 12. The hydrogen diffusion distance is $\sqrt{2 \cdot D \cdot t}$ in bcc iron with a D_{eff} value of about $10^{-5} \frac{cm^2}{s}$ at 25 °C is about 45 µm in a time of 1 second, while for nickel with a D_{eff} value of about $10^{-10} \frac{cm^2}{s}$ the corresponding distance is about 0.1 µm. For alloys with a complex

microstructure, D_{eff}-values at room temperature decrease as the number and strength of the traps increase. D_{eff} at 20 °C for ferritic steels vary by 3 to 4 orders of magnitude for different microstructures. For higher strength steels, D_{eff} values have a tendency to be lower due to a larger volume of carbide phases and a higher dislocation density. The hydrogen diffusion rates increase with temperature, see Figure 12. An increase of temperature will increasingly activate hydrogen from traps with rising trapping energies and more and more hydrogen will be released from the lattice [67–70].
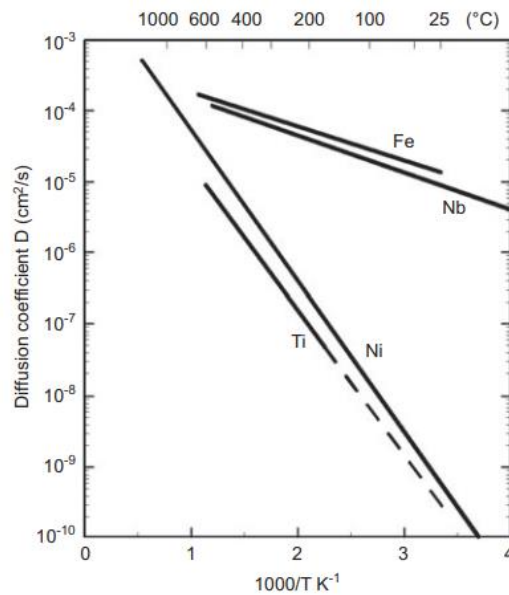

Figure 12: Hydrogen diffusion coefficients plotted as a function of inverse temperature for Fe and Nb (bcc), Ni (fcc) and Ti (hcp), from [67,70] modified from [71]

Hydrogen diffuses through the lattice as a response to 1) the hydrogen concentration, 2) the temperature and 3) the hydrostatic stress fields, where the third factor is the most important with respect to HE. Transport of hydrogen through mobile dislocations can be faster than through lattice diffusion. Transportation of hydrogen through dislocations could play an important role in moving hydrogen from the inside of the grain to the grain boundaries, promoting intergranular fracture. In some cases, hydrogen may also diffuse faster along grain boundaries than through the lattice, although if the trap density is higher at boundaries compared to elsewhere, the diffusion of hydrogen at grain boundaries could be slower than through the lattice [71].

In the permeation test, the D_{eff} of hydrogen in steel is determined. Which provides information about the trapping behaviour of the material. Multiple charging of the same specimen can distinct deep traps from shallow hydrogen traps and one can derive which type of trap is dominating. Complex sample preparation of the thin membrane, including the palladium coating, is mandatory to avoid corrosion on the oxidation side [72–75].

In 1920, Daynes was already working on the effect of diffusion and a formulation to describe the transport through a rubber membrane. Daynes specified the time delay as the value of the integrated current's value at the crossing point of the time [76]. To determine the effective diffusion coefficient the standardized time-lag-method according to Eq. (1) was used. The effective diffusion coefficient is represented as D_{eff}, the time to 63% of the maximum current as t_{Lag} and the sample thickness as L [74]:

$$D_{eff} = \frac{L^2}{6 \cdot t_{lag}}$$ (14)

2.1.3 Dissolved hydrogen

Dissolved hydrogen is located at interstitial sites in an ideal single crystal. In Figure 13 only two types of interstitial sites – octahedral (O) and tetrahedral (T) are shown, because they are the only ones that can be occupied by H atoms. In close-packed lattices for face centered cubic (fcc) and hexagonal close packed (hcp), there is one octahedral and two tetrahedral gaps for each metal atom, whereby the octahedral gaps are the larger ones. The body centered cubic (bcc) lattice has three octahedral and six tetrahedral sites acting as possible traps. According to the Somenkov rule of 1979 [77], in all metals with an atomic radius of more than 1.4 Angstroms, the tetrahedral gaps are occupied by hydrogen, this applies to Sc, Ti, Y, Zr, Nb, La, Hf, Ta, W. In metals with smaller atomic radii such as Cr, Mn, Ni, Pd the octahedral gaps are occupied. In V, both interstitial sites can be occupied [77].
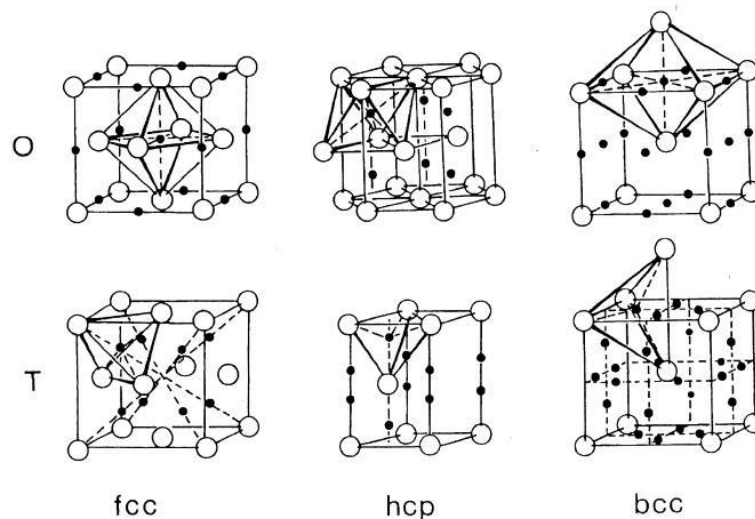

Figure 13: Interstitial sites at the octahedral or tetrahedral gap in the three most important metal lattices [78]

The high H mobility is caused by two reasons. Firstly H atoms are dissolved interstitially and no vacancy has to be formed to enable diffusion. Secondly, a change of location can occur via quantum mechanical tunnelling [79].

Hydrogen molecules who interact with a metal will dissociate at the surface and will dissolve as atoms inside the metal after the following reaction:

$$H_2 \ (gas) \ \rightarrow \ 2H \ (metal) \tag{15}$$

with its concentration according to Sieverts' law:

$$c_H \ = \ \sqrt{p_{H_2}} \, K_s \tag{16}$$

where c_H [mol/cm³] is the dissolved H atom concentration, K_s is the Sieverts constant and p_{H_2} is the partial hydrogen pressure in bar. Sieverts (1914) showed by the revelation of this relationship that hydrogen is dissolved atomically and that dissociation of the molecules is necessary prior to their absorption. [79].

Hydrogen uptake from the gaseous phase is determined by hydrogen partial pressure. With low hydrogen contents in the metal lattice, the solid solution can be described as an ideal Eq. and according to Sievert's law [44]. As a result, the concentration of hydrogen in bcc for ferritic steels or body centered tetragonal (bct) for martensitic steels can significantly increase the concentration of hydrogen at the interstitial sites. In general, the concentration of trapped hydrogen is in local balance with the concentration of dissolved hydrogen. This local balance can be maintained because hydrogen is mobile in the majority of metals, including those at room temperature. Due to this mobility, hydrogen atoms can move between interstitial sites [37].

2.1.4 Hydrogen traps

A trap for hydrogen is a place where the probability of a hydrogen atom to escape is lower than in an interstitial place. Trapping hydrogen is thermodynamically more beneficial than in the lattice itself because the atoms in the traps have a lower energy. The hydrogen concentration in steel can reach significantly higher values, especially at temperatures below 300 °C, than from Sieverts' law. The reason for this is that hydrogen is not only in solid solution in the lattice, there is also accumulation at lattice defects, which provide an energy favorable environment for hydrogen [34,45,80].

The main challenge for understanding the mechanisms behind hydrogen embrittlement is the mapping of hydrogen incorporation. Increasingly, Thermal Desorption Spectroscopy (TDS) is being used to obtain conclusions about local hydrogen traps. Voids, dislocations, grain boundaries, phase boundaries, precipitates and pores are some examples of potential lattice defects that can lead to hydrogen incorporation. The following chapter 2.2 describes the various types of hydrogen traps more detailed. The transferred hydrogen is shown in green in the following Figure 14, while the trapped hydrogen is shown in orange [81].
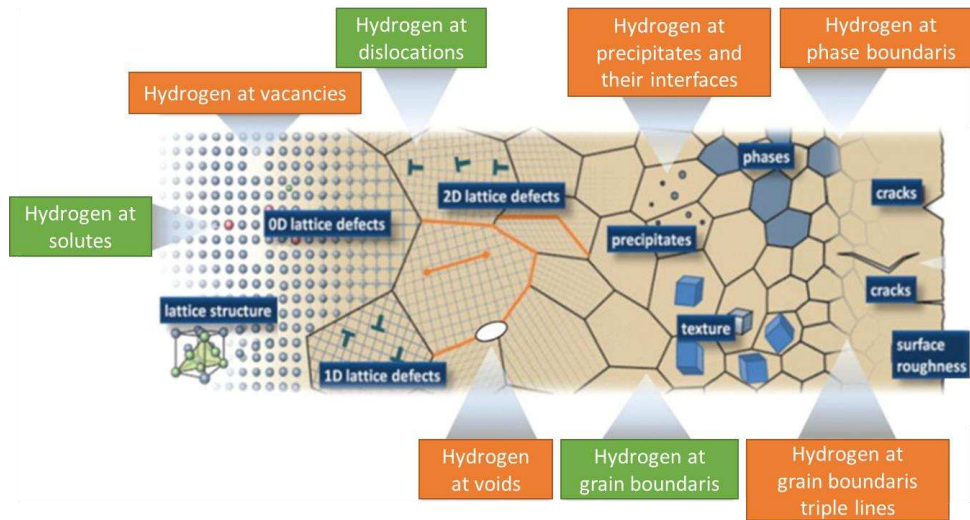
Figure 14: Possible hydrogen trapping and transport at various types of defects, adapted, originally from [81]

In TDS measurements, the samples are preloaded and discharged at different heating rates. These different critical heating rates lead to shifts in hydrogen discharge. Traps with different binding enthalpies will release hydrogen at different temperatures. The resulting peak temperatures change with the heating rate during discharge. In Arrhenius plots, the resulting hydrogen peaks at different temperatures are plotted ln(Φ/Tp2) versus 1/Tp corresponding to the Kissinger Eq. (17) for different heating rates. The binding enthalpy of a trap for hydrogen can be determined from the resulting straight lines' slope, and the type of trap can be determined from the knowledge of the microstructure [82].

$$\frac{d ln(\frac{\Phi}{T_p{}^2})}{d(\frac{1}{T_p})} = -\frac{E_A}{R} \tag{17}$$

Binding energy EB and trap density NT characterize each trap in the lattice. Traps with a binding energy EB > 60 kJ/mol can be considered as very strong or deep and irreversible and those with EB < 30 kJ/mol as weak or flat and reversible. There are usually several traps that interact with the lattice hydrogen and influence the overall behaviour of the steel. In fact, irreversible traps will always act as a sink for hydrogen. Li et al. [83] investigated different trap states and it was found that hydrogen can be trapped in multiple locations. Substitutional atoms, ferrite-cementite interfaces and various incoherent carbides can act as traps [84,85].

A further very important method for a better understanding of the hydrogen behaviour in the material is hydrogen permeation. Performing permeation tests determines the effective hydrogen diffusion coefficient. Permeation tests are performed according to the standard ISO 17081 [74] using a Devanathan-Stachursky cell [73]. The method can also be used to determine the presence of trapped hydrogen. A complex sample preparation with palladium coating is used to avoid corrosion and to act as a recombination blocker for H_2 on the oxidation side [72].

Based on their geometric properties, lattice defects can be classified in three geometric dimensions according to Table 1. From their microstructure and their defects, the HE of steels is significantly influenced [64,86].

Table 1: The classification of the lattice defects by their geometric dimensions [86,87]

Geometric Dimension	Specific type	Density	Energy
0-dimensional	Vacancies, interstitial atoms and substituted atoms	m^{-3}	J
1-dimensional	dislocations	m^{-2}	$J \cdot m^{-1}$
2-dimensional	grain boundaries, twin boundaries and stacking faults	m^{-1}	$J \cdot m^{-2}$
3-dimensional	segregations, pores and inclusions	m	$J \cdot m^{-3}$

The diffusible hydrogen in steels is on the one side determined by the total hydrogen content in the steel and on the other side on the distribution and concentration of the various traps in the lattice [84,88].

To understand the interaction of hydrogen with dislocations and cracks, it is necessary to examine the solubility and diffusivity of hydrogen, although theories and results are different. Therefore, consideration of the interstitial sites for hydrogen in iron, solubility, diffusivity, hydrogen trapping and the interaction of hydrogen with dislocations and cracks is of high importance [88].

The most common defects and their hydrogen trapping ability are explained in detail in the following subsections.

Vacancies

Lattice defects that are not filled with an atom are called vacancies, these are point defects (0-dimensional defects), see Figure 15. The concentration in which vacancies occur, the so-called vacancy density, depends on temperature. At room temperature it is lower (ca. 10^{-12} representing 1 vacancy per 10^{12} atoms). At higher temperatures close to the melting point the vacancy density reaches values near 10^{-4} representing 1 vacancy per 10000 atoms. The concentration of vacancies essentially influences the course of thermally activated space exchange mechanisms in metals, which means that a much greater density of vacancies can be expected at high temperatures. This can be controlled by the cooling rate, whereby fast cooling leads to an increased vacancy

density. The vacancy density influences significantly the course of thermally activated processes, such as diffusion. It is possible for the crystal to be in thermodynamic equilibrium when vacancies are present, which is not possible for all other lattice defects [69,86].
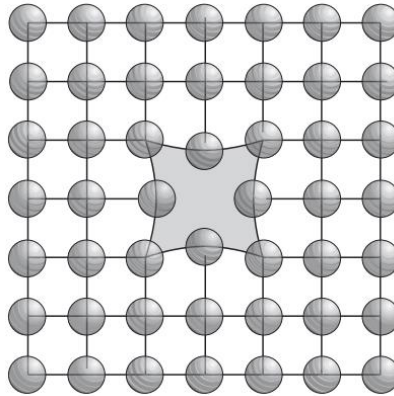

Figure 15: Schematic visualization of a vacancy [69]

When a hydrogen atom donates its electron to the electron gas of the metal, electron vacancies will attract hydrogen to achieve local neutrality. Therefore alloying elements that are electron donators (elements on the left side of the periodic table of the elements) favor hydrogen uptake [89].

Interstitial and substitutional atoms

Both interstitial and substitutional atoms are point defects (0-dimensional defects). If an atom is not located in a lattice position, but in between, then it is an interstitial atom, which can be seen in Figure 16. An interstitial atom is often created when an atom moves out of its lattice place and leaves a vacancy there [69].
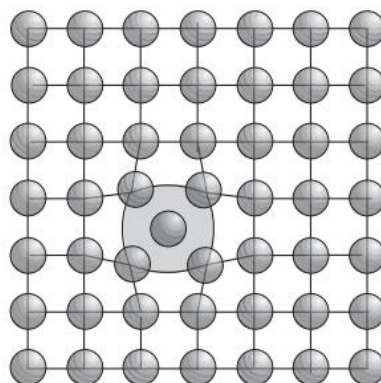

Figure 16: Schematic visualization of a interstitial atom [69]

Foreign atoms are often dissolved in the lattice and a solid solution is present. When these atoms move into lattice places they are called substitutional atoms, as shown in Figure 17 [69].
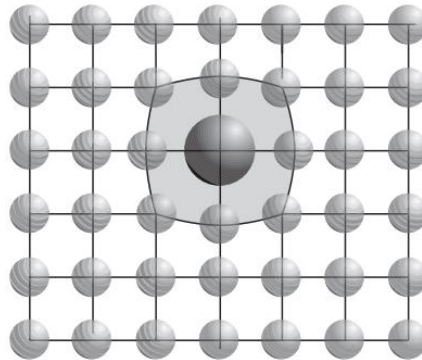

Figure 17: Schematic visualization of a substitution atom [69]

In case a small atom is located on an interstitial site, it is also called insert atom, which can be seen in Figure 18. If large amounts of different atoms are dissolved in the lattice, the resulting crystals are called mixed crystals. These are important components of metallic alloys. The tension in the lattice caused by these atoms in the solid solution, leads to a pronounced increase in strength [69].
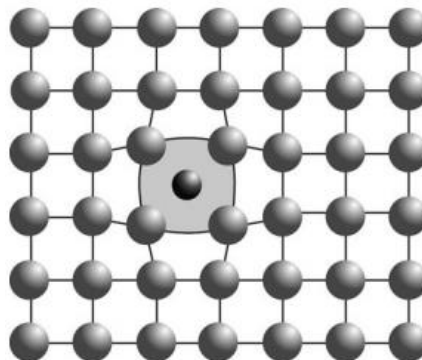

Figure 18: Schematic visualization of an insert atoms [69]

Dislocations

Dislocations are linear lattice defects, they belong to the 1-dimensional defects. There are two different forms: Step dislocations and screw dislocations. Step dislocations, can be imagined as lattice planes ending in the crystal, see Figure 19 a). In screw dislocations, the lattice planes are screw twisted perpendicular to them in the area of the dislocation cove, see therefore Figure 19 b). In general they are a combination of both types of dislocations. Dislocations either start at the surface of the crystal and end inside the crystal or form closed rings, so-called dislocation loops [69,86].
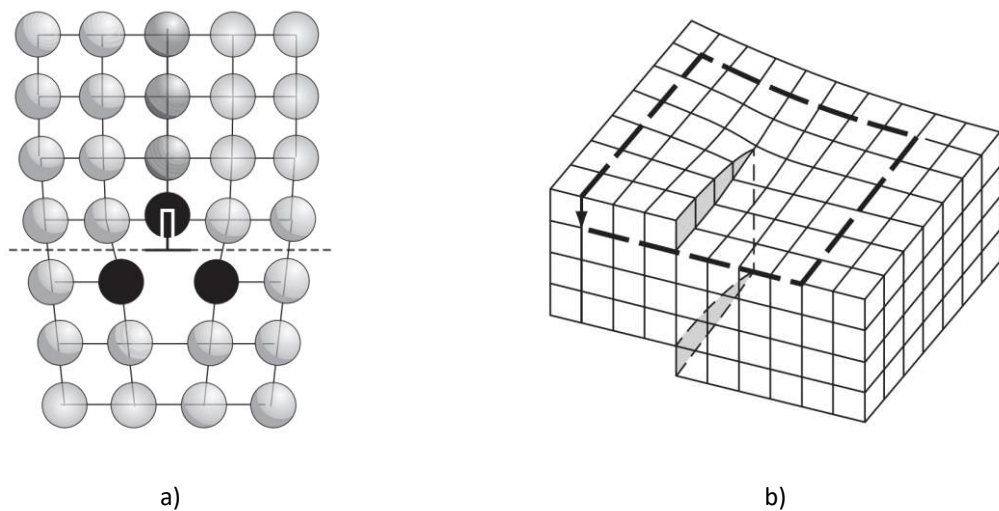
a)   b)

Figure 19: Schematic visualization of the different dislocation mechanism: a) step dislocation; b) screw dislocation [69]

Their concentration is indicated by the dislocation density that is the line length per volume unit. In a soft annealed metal, it is about $10^6 \frac{mm}{mm^3}$ which means that in a volume of $1mm^3$ there are dislocation lines up to 1 km. This length can increase to 10.000 km through cold deformation. Therefore, the stress fields of the dislocations influence each other because of their density [69].

A common mechanism for the fast transport rate of hydrogen in the lattice is transport by mobile dislocations [90]. The dislocations are inserted into the microstructure of steels by cold deformation. Dislocation density increases with increasing plastic deformation. Therefore the number of hydrogen traps increases as well [91]. The dislocation density in a cold worked austenitic phase is higher than for example in a solution-annealed one, which leads to a larger amount of transported hydrogen. If the amount of dislocation is high, hydrogen is transported in significant amounts over sufficient distances, which can lead to a failure of the material [92]. Transport of hydrogen through moving dislocations is the main transport mechanism, as it is significantly faster than diffusion and is also operative at lower temperatures [93].

Grain boundaries

Grain boundaries are the most important group of 2-dimensional lattice defects. The boundary between two crystals which are tilted against each other with a small angular difference is formed by a series of parallel step dislocations, as shown in Figure 20. Small-angle grain boundaries may also be known as subgrain boundaries [69].
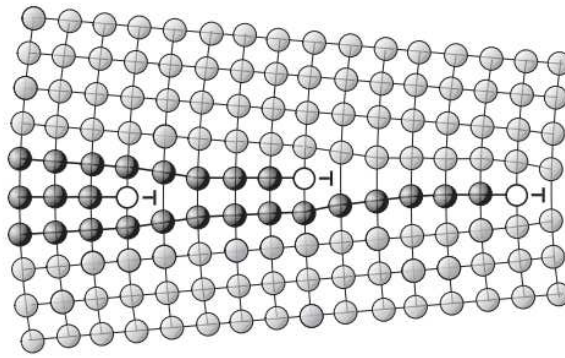
Figure 20: Small-angle grain boundary [69]

When a crystal in its growth process encounters another crystal, either during solidification or recrystallisation, the lattice planes of the crystals form larger angles to each other. If there is a large angular difference between two crystallites, a transition zone with an irregular atomic arrangement with a thickness of 2-3 atomic distances is usually formed, see Figure 21. The energy of the large-angle grain boundary is usually higher than that of the small-angle grain boundary and is between 30 and 50% of the surface energy, depending on the metal [69,86].
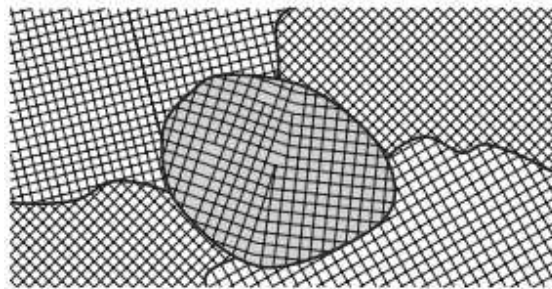

Figure 21: Large-angle grain boundaries [69]

Under certain conditions, two crystals can form an undistorted grain boundary. This is the case with twin boundaries, where the two crystals are arranged mirror-symmetrically to the grain boundary, such boundaries have the lowest energy content of all 2-dimensional defects. Twins are primarily found in fcc materials with low stacking fault energy such as brasses, bronze alloys, and austenitic stainless steels. Stacking faults are 2-dimensional lattice defects which disturb the stacking sequence of parallel planes [69,86].

Grain boundaries can positively or negatively influence the sensitivity of steels to HE, as they affect the diffusion behaviour [34]. Grain boundary engineering can reduce the sensitivity to HE [94]. A large proportion of grain boundaries with a high number of interfaces is considered to be most favourable for the resistance of steels against HE [95].

Phase boundaries

In the case of a phase boundaries, the crystal structure and the type of bonding changes. The differences of the crystal structures cause different two-dimensional structures at the phase boundaries: coherent, partially coherent and incoherent phase boundaries are shown in Figure 22, in the same order their energy increases. Partially coherent interfaces contain dislocations at regular intervals, so-called misfit dislocations. Interfaces exist as boundaries between two phases, in all phase transformations in the solid state and in composite materials. Boundaries between differently oriented crystallites of the same phase are grain boundaries.
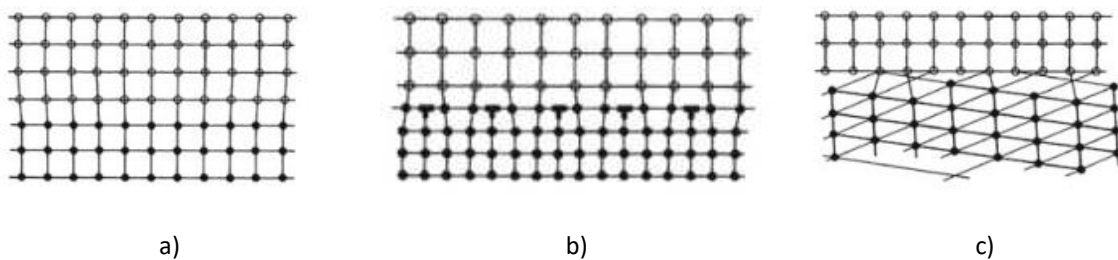

a)   b)   c)

Figure 22: Types of phase boundaries a) coherent, b) partially coherent, c) incoherent [86]

By molecular dynamic simulations it has been found that in pearlite, the thickness of the cementite phase and the ferrite grain orientation both affect hydrogen uptake. The amount of adsorbed H-atoms decreases with the cementite phase thickness. The strength of the cementite-ferrite interphase is increased after hydrogen uptake. It has been observed that hydrogen uptake and the formation of hydrogen clusters at or near the phase boundaries influence the mode of failure (towards the ferrite-ferrite boundaries) [96].

Other effects of traps influencing HE

Inclusions such as manganese sulphides, aluminum oxides, titanium oxides or iron carbides are very often the source of hydrogen-induced cracking in steel. In general, if the amount of inclusions is low, the resistance to hydrogen-induced cracking is high [97–100].

Ti, V and Nb can form carbides and/or nitrides in steels during heat treatment. These precipitates work as hydrogen traps and increase hydrogen absorption, therefore slowing down the effective diffusion coefficient of the material [64,101].

In the microstructure, retained austenite acts as a strong hydrogen sink due to its high solubility, slow diffusion and strong trapping at the interface [102,103]. Hydrogen embrittlement is retarded with an increased amount of retained austenite when the retained austenite is finely distributed [104]

2.1.5 Damaging mechanisms

The following mechanisms of HE are the most commonly acknowledged [37,71]:

- Hydrogen Enhanced Decohesion (HEDE)
- Hydrogen Enhances Localised Plasticity (HELP)
- Adsorption Induced Dislocation Emission (AIDE)

For decades, research has been conducted to determine which damage mechanism is predominant. Until now, this debate has not been settled, since it is unlikely that only one theory can applied to all hydrogen-induced embrittlement processes. The three most mechanisms are described below.

HEDE mechanism was first introduced by Troiano [105] in 1959, where the mechanism describes the effect of hydrogen on the atomic cohesion force in material and was subsequently further developed by Oriani, Wriedt and Josephic [106–108]. According to HEDE mechanism, hydrogen leads to a reduction of the cohesive bonding strength in steel. Troiano [105] proposed that the reduction of the cohesive strength is due to the transfer of the 1s electron of hydrogen to the incomplete 3d shell of the iron, which yields to decohesion of the atoms, see Figure 23. HEDE mechanism is widely accepted, although there is no direct experimental evidence that hydrogen leads to a decrease in strength. That is because there is no suitable technique for determination of cohesive bond forces between atoms [109,110].

Material failure occurs when a critical hydrogen concentration is locally exceeded. Consequently a decrease of hydrogen content is desirable for the prevention of hydrogen embrittlement [105,109].
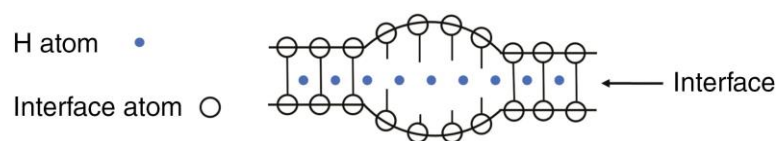

Figure 23: HEDE mechanism is shown schematically [111], adapted from [112]

Back in 1972, Beachem [113] developed a new model for hydrogen-assisted cracking (HAC) that explains the decrease in plasticity and the changes in fracture types with decreasing stress intensity at the crack tip of hardened and tempered steels. According to this model, the deformation processes in the microstructure is made possible by sufficient concentrated hydrogen being dissolved in the lattice shortly before the crack tip [113]. Robertson [114] developed this theory and suggested that hydrogen promotes local plastic deformation, which contributes to the deformation of the material and leads to fracture under load.

HELP mechanism primarily is related to dislocation movement [64]. In this mechanism, where hydrogen accumulates primarily at the crack tip, brittle crack growth is hindered when compared to hydrogen free conditions, leading to a process of microvoid coalescence in front of the crack tip [115]. This diffusion of hydrogen into the area in front of the crack is essential for the occurrence of the mechanism [71]. A presumption for plastification of the material is that the H atoms move with the dislocations. Depending on whether the hydrogen is more concentrated in the grains or at the grain boundaries the crack path can vary. Hydrogen increases the rate of dislocation sources and promotes dislocation reactions which result in the generation of vacancies and vacancy complexes [115,116]. HELP mechanism is schematically shown in Figure 24.
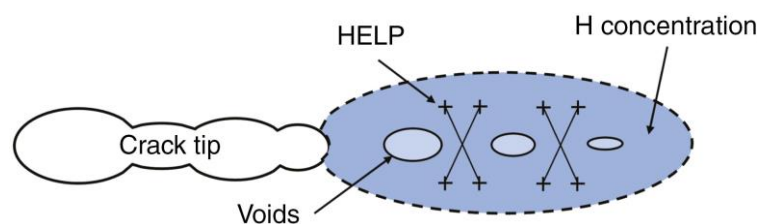
Figure 24: The HELP mechanism is shown schematically [111], adapted from [112]

AIDE mechanism was first proposed and developed by S. Lynch [117,118]. These theories of HE based on adsorbed hydrogen were suggested much earlier by others, such as Petch in 1956 [119], but the claims were explained by thermodynamic methods, with a reduction in surface energy. Clum [120] was the first to suggest in 1975, on the basis of ion microscopic field observations, that the adsorption of hydrogen could promote the nucleation of dislocations on the surface. There was no indication on his part of how such a process could cause embrittlement. The AIDE mechanism promotes enhanced local plasticity by hydrogen, in a similar way HELP mechanism describes it. The main difference between the two is that AIDE considers that the localized plasticity is due to adsorbed hydrogen on the surface, while HELP mechanism considers the dissolved hydrogen in the material playing the main role. Due to the absence of dissolved hydrogen, the occurrence of HELP mechanism is not possible, and HEDE mechanism could be excluded because localized plastic deformation was present [34,117,118].

The concept of AIDE mechanism is dislocation emission, involving both nucleation, which is promoted by hydrogen adsorption, and movement of dislocations away from the propagating crack tip shown in Figure 25. This nucleation of dislocations occurs through a process of shearing, which is a consequence of the weakening of interatomic bonds over several atomic distances in the near presence of high concentrations of hydrogen. The crack growth is assumed to occur by the same mechanism of dislocation emission and also by nucleation and assembly of voids prior to the ongoing crack. Dislocation emission is induced at a sufficiently high stress so that dislocation activity is induced at the plastic zone in front of the crack tip [34].
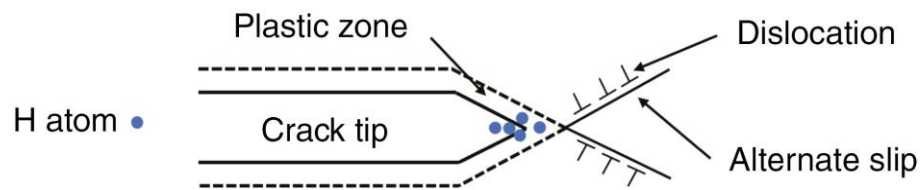
Figure 25: The AIDE mechanism is shown schematically [111], adapted from [118]

There are also other HE mechanisms such as Hydrogen Induced Phase Transformation (HIPT) shown in Figure 26. It has been proposed that some transition elements interact with hydrogen and form brittle hydrides. These brittle hydrides prevent the movement of dislocations and create a stress concentration at the crack tip, which usually occurs in titanium and other refractory metal alloys [121–124].
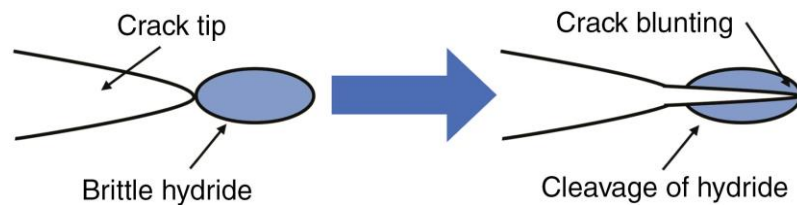

Figure 26: The HIPT mechanism is shown schematically [111], adapted from [112]

The simultaneous occurrence of several mechanisms is common in practice. Dislocations are formed by AIDE at the crack tip and can move away from the tip more easily thanks to HELP. As shown in Figure 27, the crack growth in the AIDE mechanism could be accelerated by HELP creating voids at slip bands or by HEDE splitting the particle matrix interface [71].
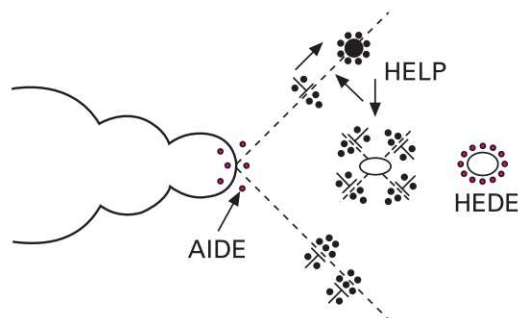

Figure 27: Schematic illustration of the mechanism AIDE with the contribution of HELP and HEDE [115]

For each fracture mode, the dominant mechanism is different, depending on many variables such as strength or microstructure of the examined material. AIDE process dominates in cases, where many voids occur along

transgranular and intergranular paths. HEDE dominates where fractures are brittle and intergranular, especially when additional embrittling precipitates are present at the grain boundaries. HELP makes a significant contribution to slip band fractures [125].

2.2 Types of gas reservoirs

The European natural gas transmission system operator ENTSOG together with several other partners have published an interactive map of all hydrogen infrastructure projects in Europe called H_2 Infrastructure Map Europe, see Figure 28. The map contains hydrogen infrastructure projects and shows the development of the projects up to the year 2050. The projects shown are divided into 5 categories, transport pipelines, distribution pipelines, platforms and ports, storage and production projects. By 2040, there will be one aquifer storage facility in Spain, and one in Latvia that will be operated with hydrogen. Depleted fields are also planned to be operational in Austria, Czech Republic, Hungary, Italy, Greece and Germany, Spain and Ireland by 2040. The main salt caverns are located in northern Germany, but there are also caverns in Ukraine, France, Portugal, Spain, Ireland, Netherlands and Slovakia. [126]. This project will contribute significantly to the climate targets of the EU as well as to the targets of the Austrian climate policy. Furthermore, the hydrogen energy pipelines will not only create transport capacities for green hydrogen, also significant hydrogen import opportunities for Austria. The changeover from fossil to renewable energy sources is strongly supported and the Austrian industry will be decarbonized in a sustainable way [127].
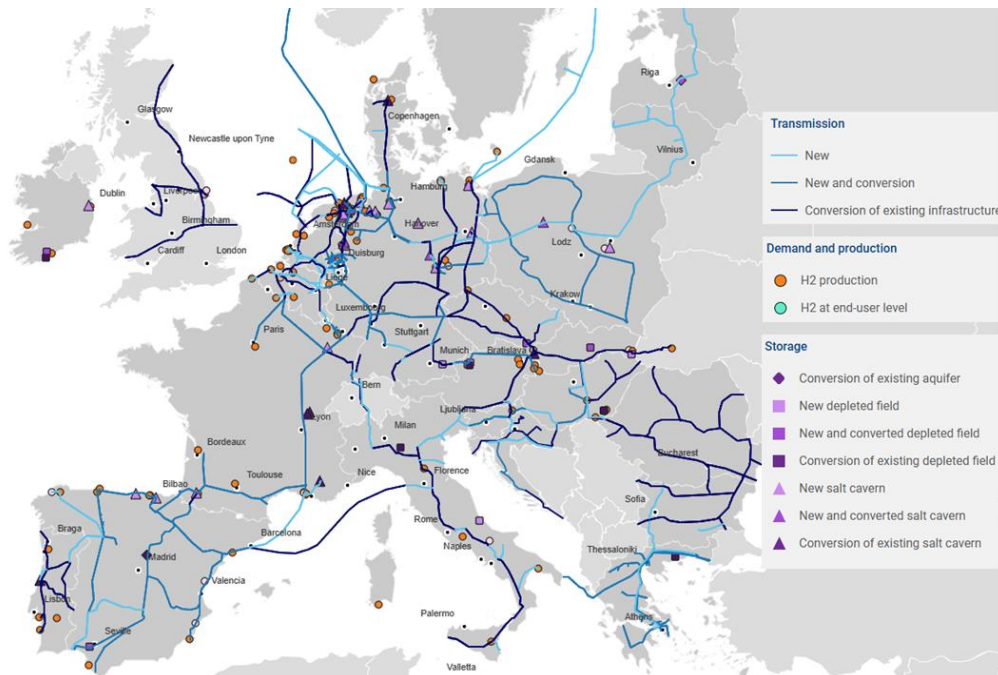

Figure 28: Infrastructure map for hydrogen in Europe [126]

Underground hydrogen storage (UHS) in geological structures can be categorized into three major groups. The main gas storage facilities include depleted gas/oil reservoirs, salt caverns and aquifers, which are illustrated in Figure 29. The above underground storage options are used for various types of gas storage, like CO2, methane and recently hydrogen. Hydrogen has the highest energy content per unit mass, which is 2.5 to 3 times higher than that of methane. In reservoir conditions, the density of hydrogen is about ten times lower compared to natural gas, which means that the storage volume for the same amount of energy has to be about 3 to even 4 times higher. Geological sites which can be used for underground storage of gases can be divided into two categories, firstly in permeable media, where the gas is stored in the pore spaces of sandstones or carbonate formations, or secondly in cavern storage, where the gas is stored in cavities created in a dense rock [19,128,129].
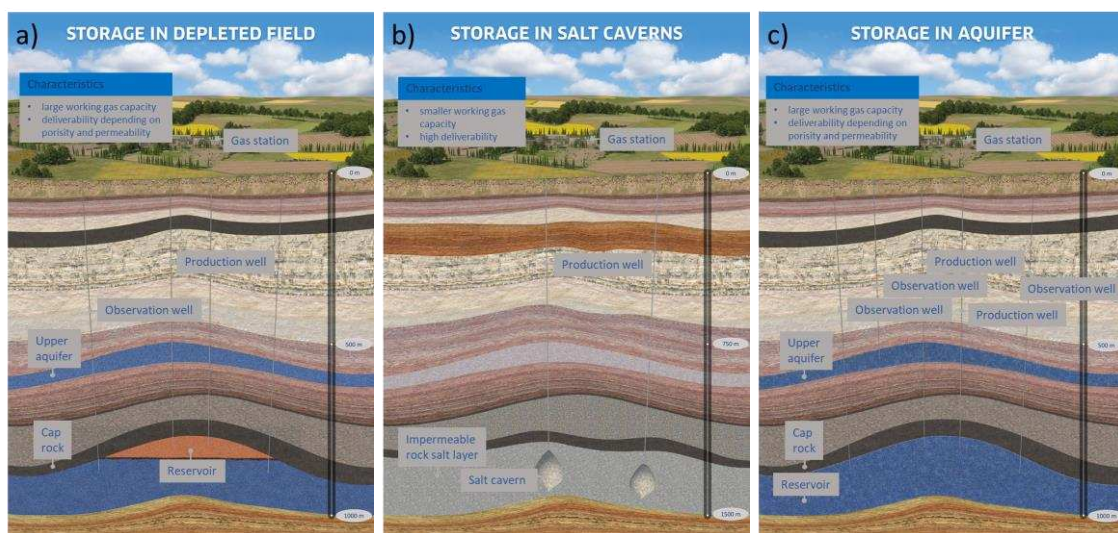

Figure 29: Various types of energy storage facilities, in a) storage in depleted field, in b) storage in salt caverns and in c) storage in aquifer [130]

2.2.1 Storage in depleted oil and gas reservoirs

Natural gas and oil deposits occur in so called geological traps, which are supported by an impermeable layer of hard rock (cap rock) that is additionally protected by an underlying aquifer. These traps usually consist of an accumulation of hydrocarbons in the pore space of sandstones. The cap rock that seals the reservoir has a very low permeability and keeps the hydrocarbons in the reservoir and prevents them from leakage [19,131].

The most common storage facilities for underground storage sites are depleted gas reservoirs. These types of reservoirs are usually equipped with the necessary above and underground devices that can be used for hydrogen storage. By adapting them to the requirements of UHS, the costs can be reduced. To enable a depleted hydrocarbon reservoir to be used as an underground hydrogen storage site, a number of geological criteria must

be fulfilled. A full evaluation of the processes involved in the implementation is required, including geological and technical aspects. The type of the used pipe, steel and cement, whether they are suitable for hydrogen and their facilities on the surface, with the safety aspect of storage being the most important issue [131].

The big advantage of depleted hydrocarbon reservoirs with respect to the others is that they have been well identified during their exploration. The impermeability of a depleted reservoir is guaranteed by its existence for millions of years. Typically, such storage facilities contain a certain amount of remaining gas that can be used as cushion gas. In 1979, Carden & Patterson [132] already discovered that the presence of cushion gas improves the performance of the storage and its efficiency. Furthermore, it was found that 1% per cycle of the injected hydrogen can be lost due to the operating process, while 0.4% of the injected hydrogen of the first cycle can be lost due to the dissolution of the hydrogen in the formation brine. Planning the establishment of a UHS in a depleted gas reservoir, the most important aspect is to stop production of gas at an optimal time. In this way, the reservoir can be established in a shorter time and at lower cost. In general, there are 5 years before newly constructed UGSs reach their perfect operating parameters. Reservoir formation water which has been injected into the gas reservoir after the shutdown of production is expelled during this time. The pressure in underground reservoirs located in depleted reservoirs suitable for UGS often exceeds the original reservoir pressure, which enables the storage of larger quantities of gas. Depleted oil reserves are rarely used for UHS, as large amounts of hydrogen can be converted into methane CH_4, dissolve in the oil and be irreversibly lost in chemical reactions with the residual oil [131].

2.2.2   Storage in salt caverns

Salt caverns are artificially constructed Chambers in salt reservoirs and are suitable for the storage of several substances, especially for gases at high pressure. By injecting water they are obtained, which dissolves a part of the salt over time. The brine is then removed. Then the gas is stored in the chambers that are leached in salt. Storage chambers in salt are used because of the geological conditions which create density in the reservoirs, the beneficial mechanical properties of the salt and its chemical resistance to reactions by most of the stored substances. Due to the thickness of the salt deposits it is also possible to build underground storage facilities with a large capacity. These specific properties of the salt guarantee a long stability and the impermeability of the storage. In the UK and the USA hydrogen has already been stored successfully in several salt caverns [130,131].

Form, depth, thickness of salt bed, its composition, distribution and dissolution of solid rocks are the main parameters for selection of a salt dome for underground storage. The tightness of the reservoir can be affected by inclusions of non-salt rock in the strata but also by easily soluble salts such as potassium-magnesium chlorides, which can provide an escape trail [131].

Sufficient water supply is another prerequisite for extraction of the cavern and to ensure the proper brine removal. OPEX are lowest for salt caverns among all other types of possible storage facilities. These storage sites are easily manageable and the gas can be injected and extracted several times during the year. They are well suited for storing gas for peak periods [131].

Salt caverns are made by human and they are usually cylindrically shaped cavities in thick salt deposits, constructed from above by injection of water into a drilled hole into the salt rock. This technology is so called solution mining. Depending on the design and technical feasibility these cavities can be created at depths of up to 2000 m, have geometric sizes up to 1 million m^3, typically a height of 300 to 500 m, and a diameter of 50 to 100 m. Due to different depths, it is possible to operate them with a pressure of up to 200 bar, which makes it possible to store very large quantities of gas. The physical properties of salt provide stability and density in the long term. These properties also make them ideal for short-term storage to cover peaks. They are the most cost-effective method of operating storage facilities. With several hundred meters of wall thickness, as well as decades of experience with this type of storage, the safety aspect during operation is also guaranteed [133].

2.2.3   Storage in aquifers

Aquifers consist of porous and permeable rock layers with pore volume occupied by water, freshwater or saline, located at greater depths. They are found in sedimentary reservoirs around the world and can be an alternative for underground hydrogen storage in areas, where depleted hydrocarbon reservoirs or salt caverns are unavailable. These facilities have been used safely as natural gas storage facilities since decades [131].

The storage of hydrogen in deep aquifers is quite comparable to the storage of hydrogen in depleted fields. Two geological prerequisites are necessary for establishment of an underground storage facility. On the one hand the selected rocks for injection must have good storage properties, and on the other hand the covering rock must be impermeable, which prevents the escape of the gas. When the pore space of the aquifer selected for storage is filled with water, this must be replaced and pushed to the side to create space for the storage. This requires a high pressure. The injected gas has to replace the water, which will return when the pressure drops. The boundary between gas and water shifts during operation and the water also seals the storage space downwards. A significant amount of gas remains in the aquifer. The amount of gas that can be stored depends on various parameters such as the volume, porosity, temperature and pressure in the reservoir [131].

Potential hazards exist related to the escape of hydrogen in aquifers like leakage along undetected faults or biochemical reactions and reactions of hydrogen with minerals in the reservoir. The tightness of an aquifer, in

comparison to depleted reservoirs is unknown and must first be determined. For this reason aquifer explorations will require drilling, which will require extensive and costly testing to determine the tightness of the total reservoir. This provision makes the establishment of such a storage unit more expensive. There is a low risk of hydrogen leaking through to the surfaces. A potential eruption can be prevented with the automatic closing system with a safety valve. Hydrogen stored in an aquifer cannot inflame due to the oxygen deficiency, this completely eliminates the possibility of the formation of a flammable composition [131].

2.3 Conditions in gas reservoirs

The interaction of hydrogen with chemicals present in underground reservoirs is a factor that needs to be taken into account. On the one side toxic gases can be formed and on the other side hydrogen can be lost due to these chemical processes. With the exception of salt these deposits or excavated caverns are generally composed of stable nonreactive minerals. The potential presence of sulfide, sulfate, carbonate and oxide minerals at the surface of the minerals is of great importance. However, the deposit temperatures studied by Foh in 1979 [134] are not high enough to initiate a reaction. Therefore, a reaction with these chemical substances is considered unlikely at 298 K and a pressure of 2000 psi (equal to 137.9 bar) [134,135].

There is a possibility of hydrogen contamination when working gas mixes with cushion gas and dissolved gases in the brine such as H_2S, CO_2 and CH_4 in porous media. Potential anaerobic metabolic processes caused by dissolved gases in the formation brine are major aspects that must be considered. Such brine is often saturated with CH_4 and H_2S, and if these gases interact with the injected hydrogen, the resulting chemical equilibrium disruption can result in the release of H_2S, CH_4 or CO_2. The possible release of such gases could lead to contamination of the injected hydrogen and eventual leakage of more toxic gases such as H_2S [136–138].

In underground storage facilities, large amounts of hydrogen loss have been observed, which can be caused by geochemical, biochemical or microbial growth reactions of hydrogen. The microbial interaction is the most dominant cause on the loss of hydrogen in underground reservoirs and therefore a critical factor for UGS [139]. During hydrogen injection, there are four important biotic chemical interactions that can occur, shown in Figure 30. Pore water may provide a suitable environment for the microbial activity resulting in accumulation of hydrogen [140–142].
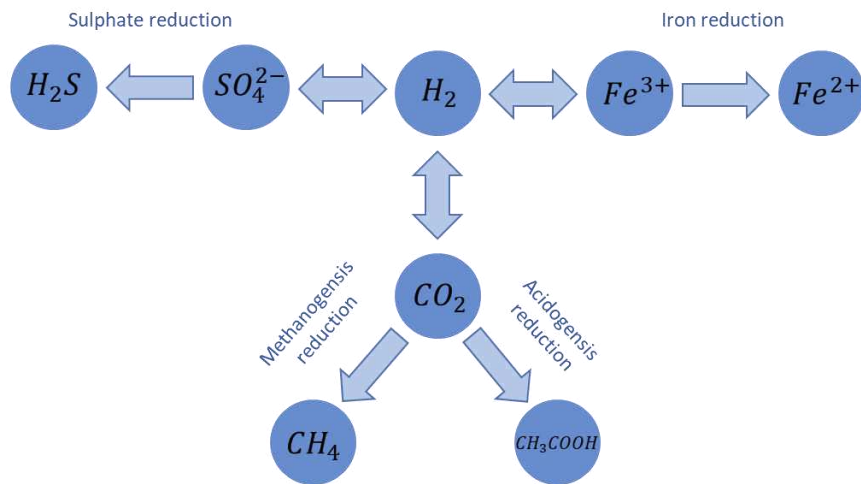
Figure 30: Four major reactions that can occur during underground hydrogen storage, modified from [141]

Sulphate reduction

When sulphate is present in a reservoir, hydrogen can be transformed into hydrogen sulfide as an electron donator when sulfate reducing bacteria are present, see Eq. 18. Anaerobic bacteria such as these are very adaptable and have been detected in many underground gas reservoirs. Consequently, this reaction can be expected in a hydrogen storage facility. Besides the loss of hydrogen, this interaction results in other significant problems including the formation of a corrosive sour environment which leads to corrosion of well casings and tubings. There may also be plugging near the borehole of the reservoir area due to sulfide precipitation, which subsequently causes problems with hydrogen storage and injection. For a typical gas storage facility, the amounts of H$_2$S and carbonyl sulfide (COS) should not exceed a value of 5 $\frac{mg}{m^3}$ to avoid problems caused by corrosion [143]. Due to the effect of these sulphate reduction reactions, this amount can easily be exceeded [141,144].

$$SO_4^{2-} + 5H_2 \rightarrow H_2S + 4H_2O \tag{18}$$

Iron reduction

The iron reduction reaction uses iron oxide that is present in the mineral part of the rock. Slobodkin [145] discovered a significant $Fe_2^+O_3$ reduction and $2Fe_3^+O_4$ increase by iron reducing bacteria in deposit rock at temperatures ranging from 55 to 87 °C based on experiments with injection of pure hydrogen, see Eq. 19. Different microorganisms have different threshold concentrations for the induction of these reactions, whereby iron reducing bacteria have the lowest threshold. Therefore, this reaction has the highest chance of occurrence. Nevertheless, as the microorganisms can increase in the presence of excess hydrogen during the storage phase, also other reactions can occur at the same time. This reactions are sulphate reduction, methanogenesis and acidogenesis [19,141].

$$3Fe_2^{3+}O_3 + H_2 \rightarrow 2Fe_3^{2+}O_4 + H_2O \tag{19}$$
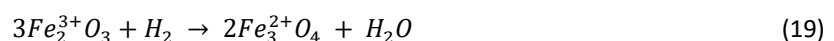
Methanogenesis reaction

Methanogenesis occurs in its presence of methanogenic bacteria and generates methane by the consumption of CO_2 and H_2, see Eq. 20. This leads to large hydrogen losses, nevertheless it can also be used as a CO_2 capture mechanism due to its ability to consume CO_2 and produce methane. The resulting CH_4 has a greater energy capacity than hydrogen. Such an approach is cheaper than the existing industrial process, which requires the use of high temperature and costly catalysts. The methanogenesis can take place at low pressures and temperatures by the activity of methanation bacteria [141,146].

$$CO_2 + 4H_2 \rightarrow CH_4 + 2H_2O \qquad (20)$$

Panfilov [146] describes this reaction as resulting in a significant decrease of the reservoir pressure, as the number of molecules decreases at constant pressure and temperature, and a significant amount of gas is converted into water. This decrease of the pore pressure may look like a leakage of the gas in a reservoir. Specifically, under typical reservoir storage conditions of depleted gas reservoirs at a pressure of 10 MPa and a temperature of 35 to 40 °C with natural pH the reaction rate is optimal [141,147,148].

Acidogenesis reaction

In this metabolic reaction hydrogen and carbon dioxide are used up by homoacetogenic bacteria, producing methane and acetate, which can be readily converted to acetic acid through protonation, can be seen in Eq. (21). Although it is difficult to predetermine the possibility of the presence of these reactions at a specific deposit, these can always take place if a suitable storage environment and the corresponding organisms are present. Both methanogenesis and acetogenesis can take place at the same storage facility [149].

$$2CO_2 + 4H_2 \rightarrow CH_3COOH + 2H_2O \qquad (21)$$
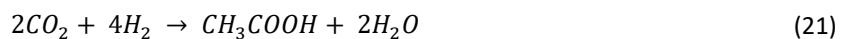
These studies have all indicated that biotic reactions lead to mineralogical variations and changes in flow properties in the reservoirs under typical storage conditions at temperatures above 130 °C and pressures above 35 MPa during regular storage cycles of more than once a year. Therefore, the impact of these reactions should not be underestimated for any underground hydrogen reservoir [141].

The following points summarize the parameters that are important for microorganisms in UHS. The permeability is significant only for porous rock deposits. All other parameters are relevant for porous rock formations as well as for salt caverns [150].

Temperature

Temperature for underground storage ranges from 30 to 150 °C, except salt caverns which have a lower temperature range of 20 to 60 °C for recommended depths of 500 to 2000 m. Microorganisms can be classified according to their temperature of maximum growth. The upper temperature, where they can liven is 122 °C. This

indicates that reservoirs with temperatures above 122 °C can be considered as sterile for microbial activities, as long they stay above this temperature during the entire operation period [150,151].

Salinity

The salinity range relevant for UHS is between 0 and 5 M, which corresponds to 292 g/l NaCl, in which very diverse communities can be found. There are methanogens and acetogens existing in saline environments of up to 4.4 M. It seems that the composition of the brine, and not salinity alone, can limit microbial growth [150,151].

pH

The pH of the brine can influence the microorganism growth via a direct effect on the growth metabolism and an impact on the redox reaction. The majority of methanogens and sulphur species reducing microorganisms (SSRM) cannot grow outside the pH range of 4 to 9.5. Nevertheless, 18 known SSRM are tolerant to a pH value higher than 10, 9 known SSRM grow below a pH value of 1 and 6 known acetogenic organisms have critical pH values of 10. A neutral pH value promotes a greater diversity of microbes [150].

Pressure

High pressure occurring in UHS generally is less inhibiting to microbial cell action in comparison to high temperatures. No upper pressure limit for microbial life has been established so far, but at 30 to 50 MPa the growth of various atmospheric pressure adapted microorganisms would be inhibited. Extremely fast pressure changes will cause microbial cells to die [150].

Mineralogy

Mineralogy has a significant direct effect on water chemistry. Species that can puffer the brine can stabilize pH and favor growth of specific microorganisms. Often, minerals are the source of macro and micro elements needed by microbes. Mineral surfaces are often inhabited by microbes that tend to form biofilms to protect themselves [150].

Permeability

Permeability is a factor for microbial life in the underground within porous rock formations. When reservoirs are very tight, there is not enough space for microbes. In reservoirs with higher permeability, in general, more microbes are living [150,152,153].

Economic factors and costs

Levelised Cost of Storage (LCOS) and Capital Costs (CAPEX) per kWh and per kg H_2 are shown below (Table 2). All data are compared on the basis of same amount of hydrogen storage [142].

Table 2: LCOS and CAPEX costs for the three main hydrogen storage options [142,154]

Storage Type	LCOS ($/kg H_2)	LCOS ($/kWh)	CAPEX ($/kg H_2)	CAPEX ($/kWh)	Working Gas Volume (t H_2)
Salt cavern	0.28 – 1.40	0.01 – 0.04	27.2 – 51.5	0.82 – 1.55	500 – 1912
Depleted reservoirs	0.88	0.03	18.4	0.55	1912
Aquifer	0.89	0.03	19.3	0.58	1912

Salt caverns have highest CAPEX of all types of Underground Storage Systems but very reasonable LCOS. It appears that there is a wide range of costs related to UHS and should be evaluated separately for each storage site. Storage costs are difficult to standardise as there is a wide variation in sizes, operating conditions and number of injection and removal cycles [142].

3 Experimental investigations

3.1 Materials

Within the scope of the present work, low-alloyed steels, four chemically resistant steels and one nickel-based alloy were investigated experimentally.

The following materials (steels) were investigated:

Carbon steels:

- 20MnV5,
- J55 welded,
- K55,
- K55 welded,
- L80,
- P110,
- quenched material (not commercially available).

Corrosion resistant alloys:

- 13% Cr steel,
- 316L (from two different suppliers),
- Alloy 625,
- Duplex 2205.

Chemical analysis, mechanical properties and microstructure were characterized for all materials.

3.1.1 Chemical analysis

The chemical composition was determined by optical emission spectroscopy. The composition of all supplied carbon steels and corrosion resistant alloys (CRA) is given in Table 3:

Table 3: Chemical composition of all investigated materials

Category	Material	C	Si	Mn	P	S	Cu	Cr	Ni	Mo
	20MnV5	0.180	0.20	1.12	0.016	0.0040	0.16	0.08	0.07	0.02
	J55 BM*	0.320	0.21	1.31	0.013	0.010	0.01	0.24	0.01	<0.01
	J55 WM*	0.070	0.61	1.35	0.007	0.010	0.10	0.05	0.86	<0.01
	K55	0.370	0.21	1.19	0.014	0.0060	0.11	0.18	0.09	0.09
Carbon steels	K55 BM*	0.180	0.43	1.54	0.016	0.004	0.09	0.16	0.14	<0.01
	K55 WM*	0.120	0.65	1.29	0.008	0.009	0.14	0.05	0.04	<0.01
	L80	0.240	0.20	1.00	0.014	0.0010	0.03	0.31	0.05	0.02
	P110	0.270	0.24	1.05	0.010	0.0040	0.21	0.28	0.07	0.02
	quenched material	0.250	0.19	1.01	0.017	0.0012	0.02	0.31	0.04	0.02
	13% Cr	0.190	0.25	0.64	0.010	0.0009	0.09	12.78	0.13	0.01
	316L (supplier 1)	0.012	0.35	1.61	0.025	0.0019	0.23	16.92	11.27	2.11
CRAs	316L (supplier 2)	0.020	0.38	1.59	0.027	0.0020	0.24	16.66	11.34	2.17
	Duplex 2205	0.019	0.48	1.73	0.025	0.0010	0.13	22.38	5.09	3.40
	Alloy 625	0.019	0.10	0.21	0.007	0.0006	0.01	19.65	57.79	7.56

*BM = base material; WM = weld metal

Continued Table 3: Chemical composition of all investigated materials

Category	Material	W	V	Nb	Ti	Co	B	Al	Sn	N2
Carbon steels	20MnV5	<0.01	0.06	-	-	0.01	0.0001	0.024	0.013	0.0069
	J55 BM*	<0.01	0.0020	-	0.001	<0.01	-	0.026	0.002	0.0053
	J55 WM*	<0.01	0.0010	-	0.036	0.01	-	0.002	0.006	0.0048
	K55	0.01	-	-	-	0.03	0.0002	0.020	0.009	0.0092
	K55 BM*	<0.01	0.1050	-	0.003	0.01	-	0.015	0.003	0,0124
	K55 WM*	<0.01	0.024	-	0.002	0.01	-	0.003	0.004	0.0038
	L80	<0.01	-	-	-	0.01	0.0019	0.039	0.004	0.0042
	P110	<0.01	-	-	-	0.01	0.0008	0.028	0.011	0.0083
	quenched material	<0.01	-	-	-	0.01	0.0013	0.041	0.012	0.0040
CRAs	13% Cr	<0.01	0.05	-	-	0.02	-	0.007	0.005	-
	316L (supplier 1)	0.03	0.11	-	-	0.13	0.0007	0.005	0.007	0.0710
	316L (supplier 2)	0.03	0.06	0.02	0.008	0.14	0.0014	0.004	0.007	-
	Duplex 2205	0.04	0.03	-	-	0.07	0.0017	0.009	0.006	0.1650
	Alloy 625	0.02	0.03	3.10	0.175	0.01	0.0008	0.080	0.003	0.0110

*BM = base material; WM = weld metal

The chemical composition of the materials studied is in accordance with their specification, with the exception of nickel-based alloy 625. For this material, the content of C, Cr, Ni, Mo and Nb are slightly too low, which could be due to the cladding process (oxidation of these elements). Specimens from Alloy 625 have been manufactured from a Alloy 625 cladded carbon steel. The CRAs are classified according to increasing alloy content.

3.1.2 Mechanical properties

The mechanical properties of the materials have been determined Beta 50 universal tensile testing machine from Zwick Roell. Each material was tested twice. Mechanical properties were carried out twice at room temperature in air and in glycerine at 120 °C for K55, L80 and the welded J55 steel. All other materials were tested in air at

room temperature. Table 4 summarizes the mechanical properties of all investigated materials. The carbon steels are ranked by increasing yield strength.

Table 4: Mechanical characteristics of all investigated materials

Material	Temperature [°C]	Environment	Yield strength [MPa]	Tensile strength [MPa]	Fracture Elongation [%]	Reduction of Area [%]
20MnV5	RT	in air	361 ± 16	517 ± 6	21.3 ± 3.3	61.7 ± 0.2
J55 welded	RT	in air	371 ± 7	593 ± 5	16.3 ± 1.2	70.1 ± 0.1
	120	in glycerine	321 ± 5	583 ± 5	16.4 ± 0.2	68.0 ± 0.5
K55	RT	in air	407 ± 2	682 ± 8	15.4 ± 0.2	54.2 ± 0.8
	120	in glycerine	380 ± 5	673 ± 8	10.75 ± 0.3	41.3 ± 3.3
K55 welded	RT	in air	446 ± 8	606 ± 4	16.4 ± 0.0	75.1 ± 0.6
L80	RT	in air	549 ± 11	636 ± 1	18.7 ± 0.3	63.5 ± 1.5
	120	in glycerine	494 ± 4	607 ± 0	14.5 ± 0.0	48.1 ± 1.1
P110	RT	in air	894 ± 6	958 ± 10	11.8 ± 0.1	60.5 ± 0.2
quenched material	RT	in air	1225 ± 15	1606 ± 31	8.3 ± 0.3	51.2 ± 1.4
13% Cr	RT	in air	525 ± 3	698 ± 0	17.2 ± 0.5	64.0 ± 0.6
316L (supplier 1)	RT	in air	202 ± 7	469 ± 5	53.1 ± 1.4	79.9 ± 0.6
316L (supplier 2)	RT	in air	236 ± 9	547 ± 3	57.9 ± 3.0	83.3 ± 0.2
Duplex 2205	RT	in air	517 ± 27	654 ± 47	23.2 ± 0.1	68.9 ± 0.7
Alloy 625	RT	in air	427 ± 12	540	31	43.0

The steel with the highest strength (1606 ± 31 MPa) is the quenched steel grade. The material with the lowest strength (469 ± 5) is stainless steel 316L from supplier 1.

Hardness testing of welds requires a series of indentations to be made over a large sample area. For this reason a hardness mapping was done for both welded materials (J55 and K55) using a Qness Q60A+ hardness testing

machine at the Chair of Material Science in Leoben. The test method according to Vickers [HV1] was chosen for the measurement of the hardness curve.

Figure 31 shows the hardness mapping for welded steel J55. The maximum value was 458 HV, which is located in the heat affected zone (HAZ) of the last welding of the top layer. Figure 32 shows the hardness mapping of the welded material K55, where the highest measured hardness is 316 HV. When comparing the two materials, it is noticeable that the welded steel J55 has a more pronounced hardness in the upper layer of the weld with higher values up to 460 HV1.
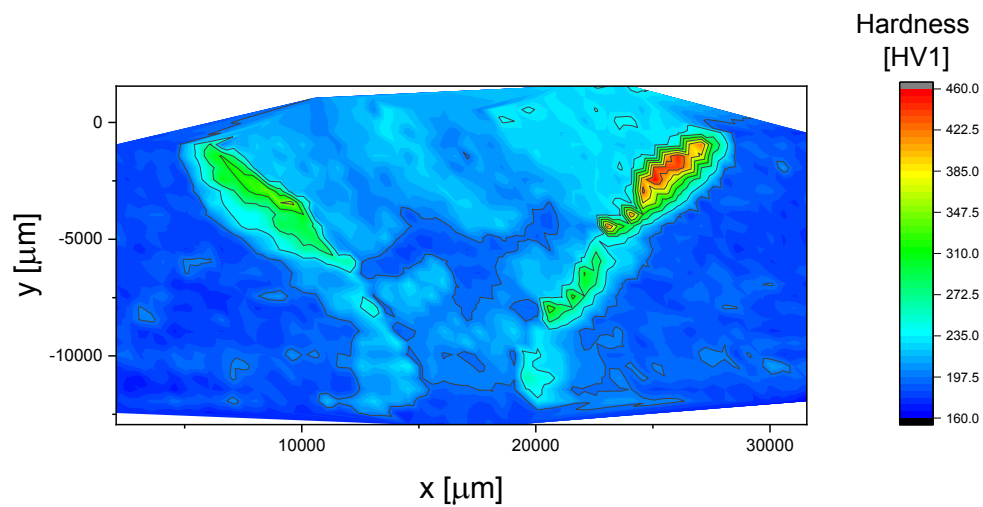
Figure 31: Vickers hardness mapping [HV1] for welded material J55
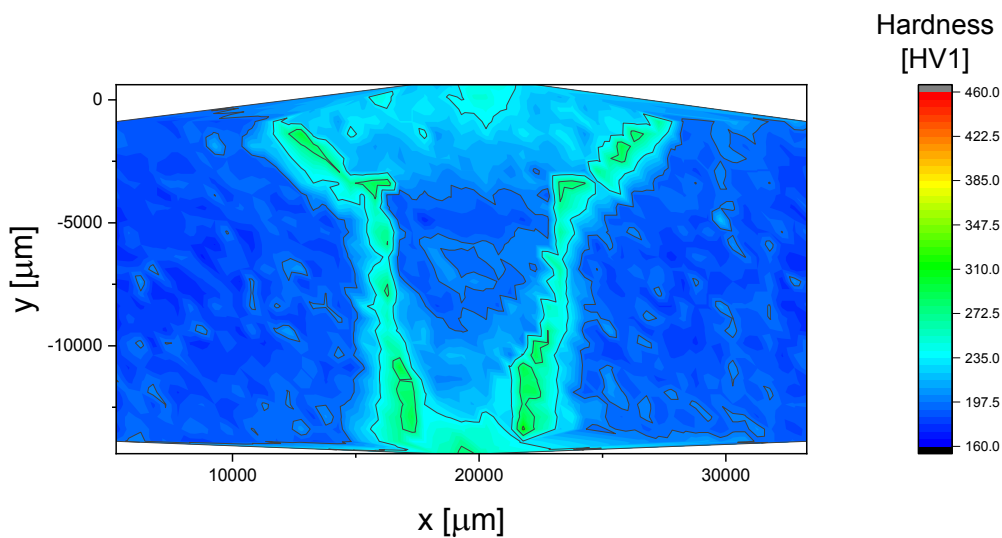
Figure 32: Hardness mapping according to Vickers [HV1] for the welded material K55

3.1.3 Microstructure

To investigate the microstructure, metallographic cross sections were prepared from all materials. The microstructure was examined with an Olympus optical microscope, model AX70.
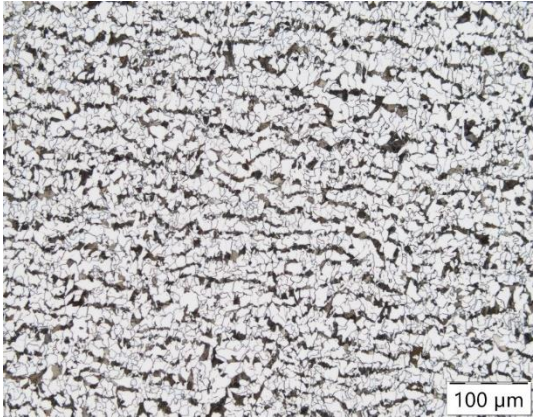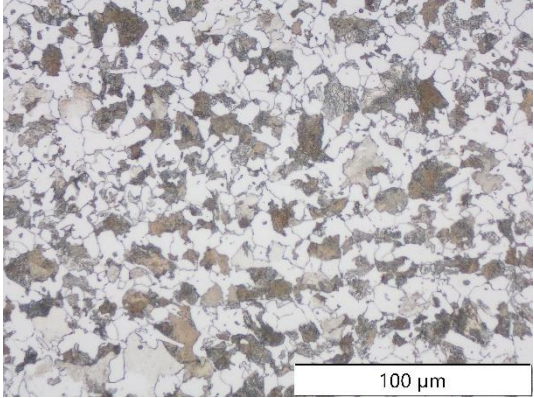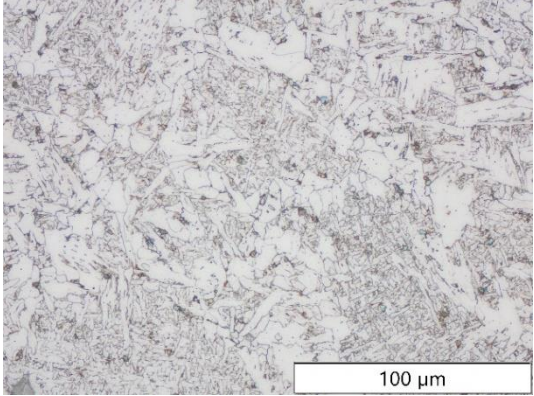
All martensitic structures were etched with etching solution after Bechet-Beaujard to visualize grain boundaries of the previous austenite grains. The grain size measurement was carried out according to EN ISO 643. The other carbon steels were etched with Nital solution (2 % HNO_3). The 316L stainless steel and duplex 2205 steel were etched with a Beraha color etching agent. The nickel-based alloy (Alloy 625) was electrochemically etched (Maerkisches Werk, consisting of 850 ml H_2O, 50 ml HF and 100 ml glycerin) at 4 V for 40 seconds.

Table 5 shows the microstructure, grain diameter and etching process of all materials examined. The carbon steel 20MnV5 shows a ferritic-pearlitic structure with an average ferrite content of 75.8 ± 2.1% and an average grain size of 11 µm. The welded steel J55 consists of ferrite and perlite with an average ferrite content of 31.5 ± 2.4% and an average grain size of 6 µm, whereby the weld material has a ferritic-bainitic structure. The steel K55 shows a ferritic and pearlitic microstructure with an average ferrite content of 26.1 ± 2.4% and a average grain size of 30 µm.
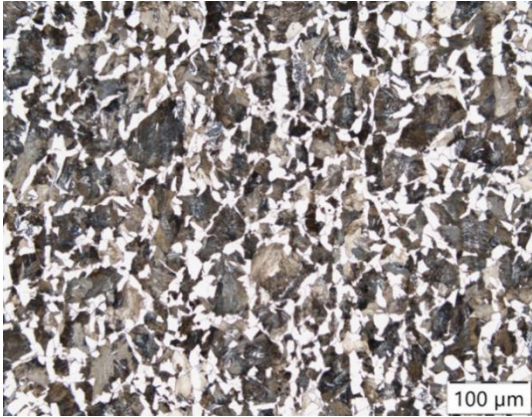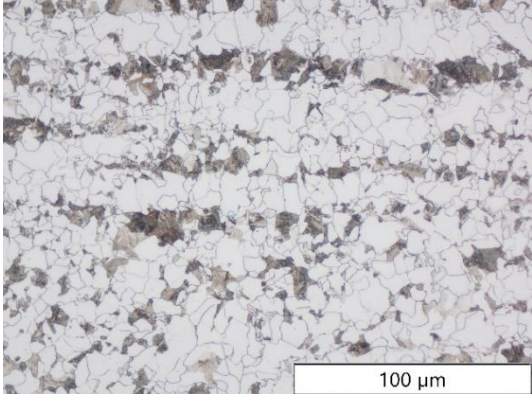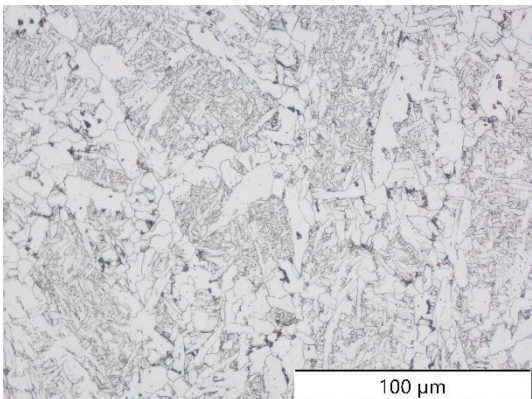
The welded steel K55 has a ferritic-pearlitic microstructure with an average ferrite content of 48.4 ± 3.3% and an average grain size of 4 µm. The weld of K55 has a ferritic-bainitic microstructure. The analysis of the microstructure of L80 shows a tempered martensitic structure with an average grain size of 20 µm. The microstructure of steel P110 consists of tempered martensite and has an average grain size of 16 µm. The structure of the quenched material consists of martensite and has an average grain size of 16 µm.

The analysis of the microstructure of the 13% Cr steel shows a tempered martensite microstructure with an average grain size of 19 µm. The austenitic stainless steel 316L produced by supplier 1 has an average grain size of 88 µm. From Supplier 2 the austenitic stainless steel 316L has an average grain size of 64 µm. The structure of a duplex steel 2205 consists of ferrite and austenite, with an average austenite content of 39.5 ± 3.1%. The average grain size of duplex stainless steel is 20 µm. The microstructure of the deposition welded Alloy 625 is dendritic.
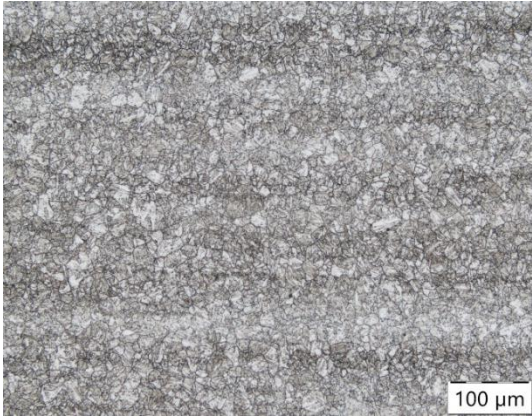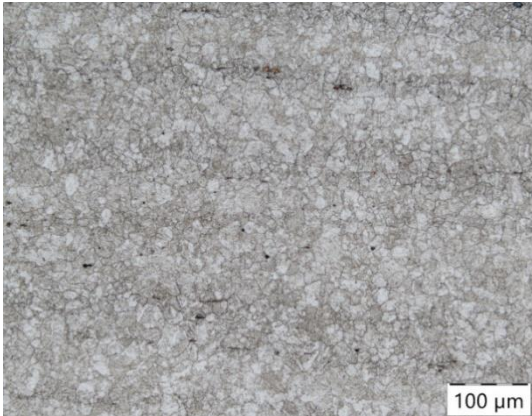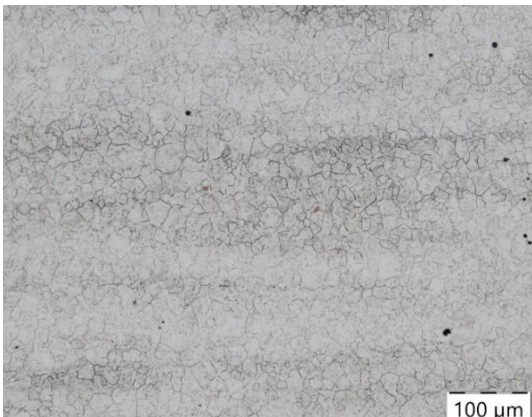
Table 5: Microstructure of the investigated steels

Material	Microstructure	Average Grain size [µm]	Description
20MnV5-1		11	Nital – Etching Ferrite + Pearlite
J55 BM*		6	Nital – Etching Ferrite + Pearlite
J55 WM*		10 - 40	Nital – Etching Ferrite + Bainite
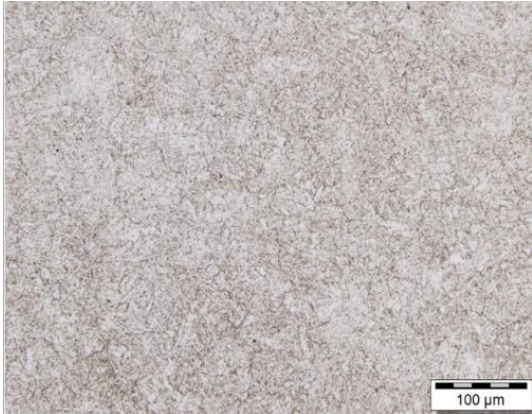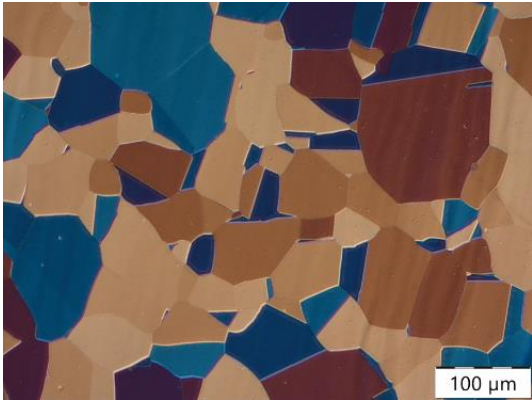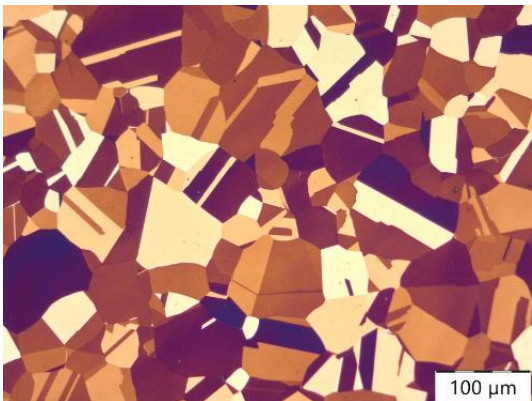
Continued Table 5: Microstructure of the investigated steels

Material	Microstructure	Average Grain size [µm]	Description
K55		30	Nital – Etching Ferrite + Pearlite
K55 BM*		4	Nital – Etching Ferrite + Pearlite
K55 WM*		10 - 60	Nital – Etching Ferrite + Bainite
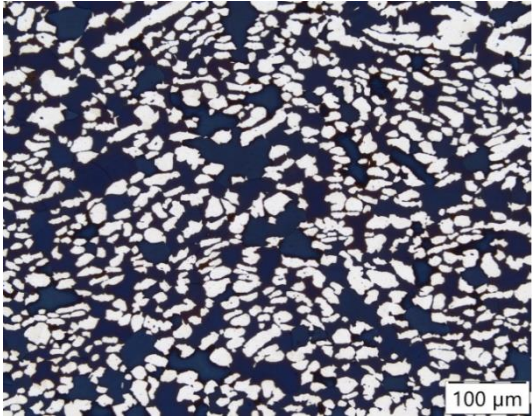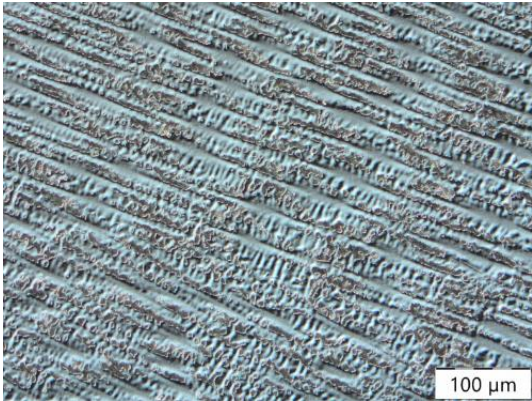
Continued Table 5: Microstructure of the investigated steels

Material	Microstructure	Average Grain size [μm]	Description
L80		20	Bechet-Beaujard – Etching tempered martensite
P110		16	Bechet-Beaujard – Etching tempered martensite
quenched material		16	Bechet-Beaujard – Etching Martensite

Continued Table 5: Microstructure of the investigated steels

Material	Microstructure	Average Grain size [µm]	Description
13%Cr		19	Nital – Etching tempered martensite
316L supplier 1		88	Color etching according to Beraha Austenite
316L supplier 2		64	Color etching according to Beraha Austenite

Continued Table 5: Microstructure of the investigated steels

Material	Microstructure	Average Grain size [µm]	Description
Duplex 2205	100 µm	20	Color etching according to Beraha Ferrite + Austenite
Alloy 625	100 µm	>100	electrolytically etched at 4 V and 40 sec. Nickel-based alloy

*BM = base material; WM = weld metal

All materials with exception of nickel-based alloy Alloy 625 correspond to the current state of the art in terms of purity, grain size, composition, mechanical properties and microstructure. The highest strength steel naturally is the quenched steel grade. Of course this material is not used in practice but only has been produced and investigated to verify the sensitivity of the experimental setup (fractures had to occur for this material during autoclave testing at constant loads).

The material with the lowest strength is 316L austenitic stainless steel of supplier 1. Non austenitic materials all showed a fine microstructure below 50 µm.

3.2   Test conditions

Conditions that can be present in underground storage facilities are summarized in the following points:

- Temperatures in underground reservoirs or aquifers can vary between 40 and 100 °C. At the wellhead, lower temperatures around 25 °C can occur.
- The pressure in storage facilities can vary between 50 and 200 bar.
- The humidity is about 100 %.
- Brine with a salinity between 1 (condensate water) and 200 g/l NaCl (formation water in very saline aquifers) can be present.
- In addition to H_2 the gas atmosphere may also contain CH_4, H_2S and CO_2. Since methane is not considered corrosive, it is not included in the test program.

The composition of the test gases was chosen on the basis of the above-mentioned environmental conditions in underground gas storage facilities. They are summarized in Table 6.

Table 6: Composition of applied test gases

Constituent	Gas A [bar]	Gas B [bar]	Gas C [bar]	Gas D [bar]
H_2	120	120	120	120
CO_2	0	15	0	15
H_2S	0	0	1	1

The tests with gas A were carried out at a total pressure of 120 bar, for gas B at 135 bar, for gas C at 121 bar and the tests with gas D were carried out at a total pressure of 136 bar. In this way, the hydrogen partial pressure remains constant over the entire test matrix. Dry tests as well as tests with electrolyte of different salinities were carried out. When an electrolyte was added, an amount of 60 ml was used to achieve a filling quantity of 50 % of the autoclave volume. All tested materials were tested for 720 hours. The test matrix to investigate the influence of brine are shown in Table 7.

Table 7: Investigated test conditions

Amount of electrolyte in autoclave [ml]	Salinity of brine [g/l]	Rotation of the autoclave [rpm]
0	0	0
60	1*	0
60	200*	0
60	1	1
60	200	1

* 2 samples: 1 sample immersed in electrolyte, 1 sample in gas phase

The tests were carried out at 25 °C and at 120 °C. In total, 4 gases x 7 conditions x 2 temperatures = 56 tests were carried out for the complete investigation of a material. This complete program is carried out for the materials K55, L80 and welded steel J55.

In order to see the changes in pH value, these were carried out with the software OLI and the effects were simulated with the addition of 15 bar CO_2 and 1 bar H_2S. The results are given in Table 8.

If CO_2 is added to the H_2 gas, the molar content is about 11 %. At this percentage the pH of the solution dropped from roughly 7 to below 3 at room temperatures due to CO_2 dissolution. If 1 bar of H_2S was added to the hydrogen gas, the molar content of H_2S is 0.83 %. At such a percentage, it can be observed that the pH in a liquid phase can drop from 7 to under 4 due to H_2S dissolution. When CO_2 and H_2S are added together to the H_2, the molar contents are 11 and 0.74 %, respectively. The presence of H_2S and CO_2 in the system causes a reduction of the pH value below 3 at 25 °C. This acidic pH value directly lead to corrosion reactions. However, the greatest decrease at low temperatures is caused in the presence of CO_2, which is present in both, gas B and gas D.

Table 8: Calculated pH values in different conditions

salinity [g/l]	room temperature				120 °C			
	Gas A	Gas B	Gas C	Gas D	Gas A	Gas B	Gas C	Gas D
1	7.06	3.33	4.01	2.90	5.96	3.68	4.00	3.54
200	7.03	2.90	3.86	3.32	5.85	3.58	3.90	3.63

Gas A (120 bar H_2), Gas B (120 bar H_2 + 15 bar CO_2), Gas C (120 bar H_2 + 1 bar H_2S) and Gas D (120 bar H_2 + 15 bar CO_2 + 1 bar H_2S)

In addition, all other selected materials and surface conditions are also examined under critical conditions. The most severe conditions in our test matrix will be Gas D with 60 ml electrolyte at 200 g/l NaCl with alternating immersion at room temperature. The conditions for all other selected materials include experiments with dry hydrogen gas, which serves as a reference. Furthermore, tests were carried out in all four gases at room temperature with the addition of brine with 200 g/l NaCl in rotating autoclaves for 720 hours.

In combination with the change to underground storage, the pipes and equipment used for hydrogen operation may already be corroded due to the uniform corrosion during operation. A question was whether uniform pre-corrosion of the steel surface can influence the effect of hydrogen on the material. Therefore, pre-corroded samples were tested, as shown in Figure 33.

It is known that local defects such as notches can increase hydrogen embrittlement. Therefore, it was decided to investigate samples with V-notches to generate an additional notching effects. The circumferential notch will result in a localized tensile stress amplitude. Such a scenario can also happen in reality, e.g. due to localized corrosion or initiation of fatigue cracks.

Figure 33 a) and b) show pre-corroded specimens. Pre-corrosion was done for one week in a rotating autoclave with 200 g/l NaCl at 15 bar CO_2. The tensile specimen with a V-notch of 0.5 mm shown in Figure 33 c) and d) was indented to create higher stresses.
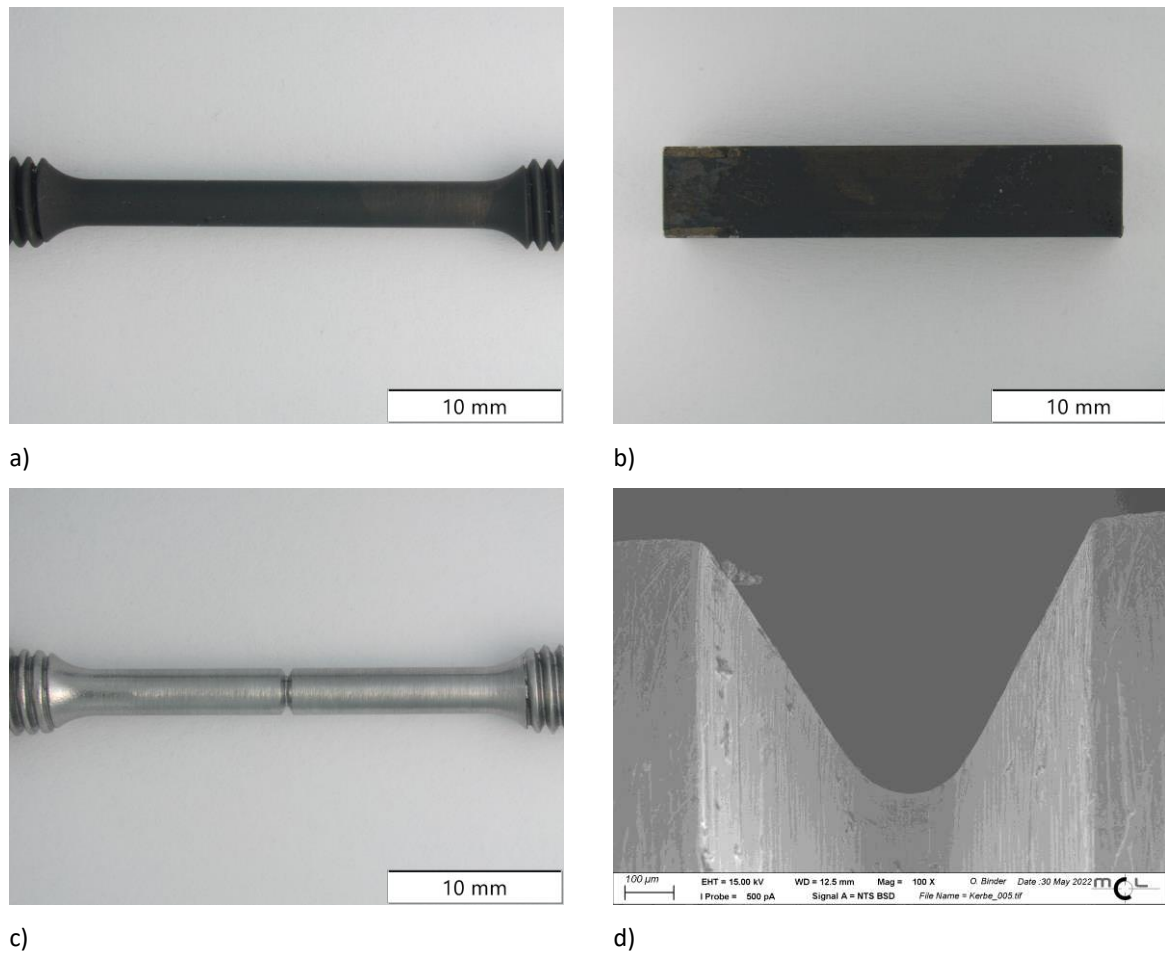
Figure 33: a) and b) Pre-corroded samples after immersion in 200 g/l NaCl with 15 bar CO_2 for 7 days, 1 rpm alternating and c) and d) V-notch specimens

3.3 Experimental set-up of autoclave tests

Autoclaves consisting of a tube with two threaded lids and made of nickel-based alloy Alloy 625 were used for hydrogen loading. In one of the lids there is an inner thread to where a valve and a quick coupling system is attached, see Figure 34.

Figure 34: Autoclave made of Alloy 625

Inside each autoclave, two samples are placed: a hydrogen sample with the specified dimensions of 6 x 6 x 30 mm, shown in Figure 35, all dimensions have a tolerance of ± 0.1 mm and all edges were milled with a geometry of 0.1 x 45° and a tensile sample for Constant Load Tests (CLT) with a total length of 80 mm and an M6 external thread, with a gauge length of 25 mm and a diameter of 3 mm. The geometry of the tensile specimen is shown in Figure 36.
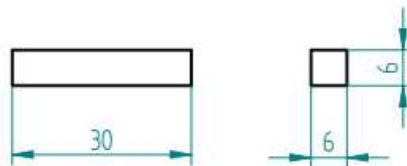
Figure 35: Geometry of the sample for hydrogen analysis
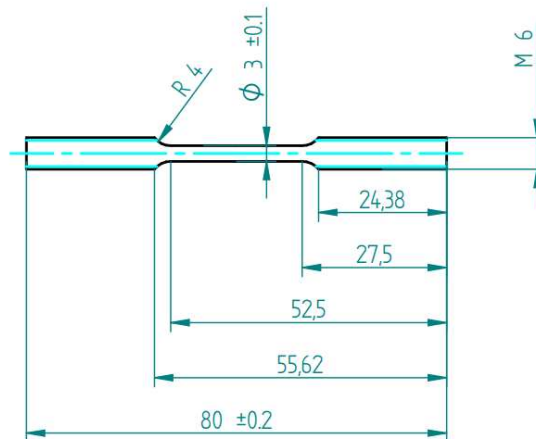
Figure 36: Sample geometry of the tensile specimen.

Figure 37 shows the tensile specimen, the ceramic nuts and the spring used for loading in detail.

Figure 37: Ceramic nuts, spring and tensile specimen

The tensile specimen is stressed with a spring at the required stress. Two ceramic nuts were used to eliminate galvanic effects. The minimum diameter in the gauge length must be measured to calculate the force which was needed to reach the tension of 90 % yield strength. The specimen assembly was carried out in a custom-built fixture within a universal testing machine from Messphysik, type BETA 50-10. The compressed spring was locked by fixing the lower nut. The crosshead of the machine was then moved upwards and the stressed specimen was removed from the clamping fixture as shown in Figure 38.

Figure 38: Loading of the tensed specimen with the aid of the clamping device

To avoid movement of the samples in the autoclaves during the test, the samples are fixed with Polytetrafluoroethylene (PTFE) distance holders, shown in Figure 39.
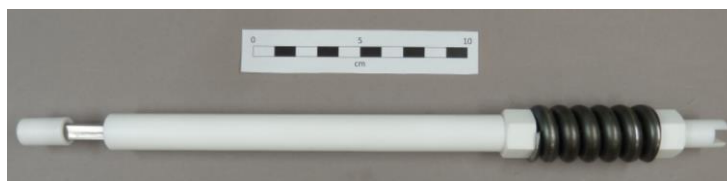
Figure 39: Positioning of the two samples inside an autoclave

The two samples with the distance holders were inserted into an autoclave lined with a PTFE foil. The sealing rings of the autoclave were covered with a vacuum paste, the threads of the autoclave were additionally sprayed with Teflon spray to achieve a high gas tightness.

Up to 8 autoclaves were placed in a polymer box that purged with Ar to avoid any air intake (Figure 40). Then the autoclaves were evacuated with a Pfeiffer Duo Line 5 vacuum pump. After reaching a pressure below 2×10^{-1} mbar, the autoclaves were Ar flooded (5 bar Ar). Finally the autoclave was evacuated again. To ensure that the autoclaves are free of oxygen, evacuation and Ar filling was done in three steps.
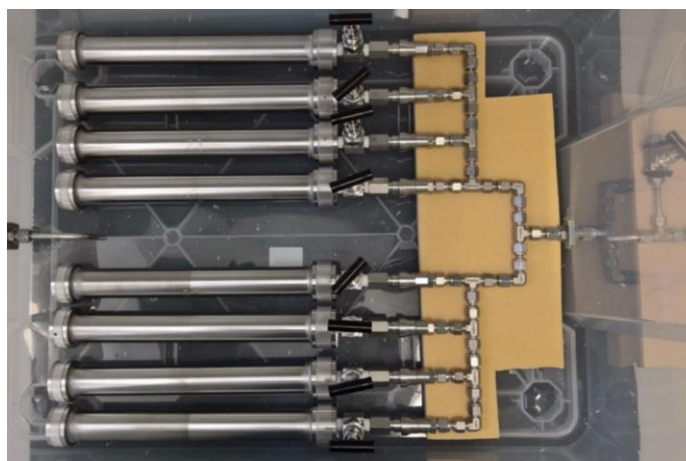
Figure 40: Evacuation and Argon floating station

When an electrolyte was added into the autoclaves the filling was done using an Ar purged filling station. 60 ml of electrolyte were dosed in the autoclave, which corresponded to 50 % of the volume remaining in the autoclave after installation of the samples and their holders. The filling station is shown in Figure 41.

Figure 41: Filling station for dosing the electrolyte

After the preparation of the autoclaves, they were filled with gas at the filling station, which is shown in Figure 42. For this purpose, a digital manometer was used to set the required pressure of the relevant gas, for safety reasons autoclaves were placed into a thick walled pipe during gas filling.
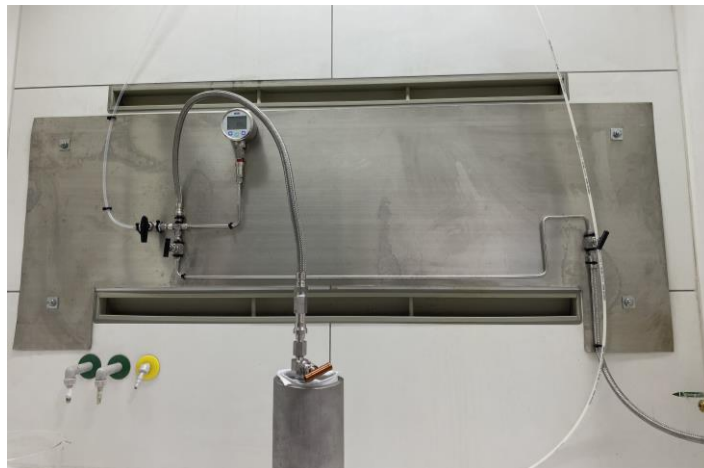
Figure 42: Gas filling station for autoclave

All tests were carried out for 720 hours in the oven. If the autoclaves need to be rotated (1 rpm) during the tests to generate wet-dry-cycles for realistic well conditions, they are fixed on a rotating shaft in the oven, see Figure 43.

Figure 43: Oven with a rotating shaft and a holder for the autoclave

After a 30-day test period, the autoclave pressure was checked via a manometer to identify pressure losses due to a leakage. After draining the gas, they were opened and the samples were quickly removed and cooled immediately in liquid nitrogen to avoid any hydrogen effusion. The outlet station is shown in Figure 44.

Figure 44: Gas outlet for autoclaves

Then the hydrogen samples were cleaned from corrosion products and analyzed for their hydrogen content by Thermal Desorption Spectroscopy (TDS) as shown in Figure 45. There were several alternating cooling steps to avoid hydrogen effusion before analysis.

Figure 45: TDS with mass spectrometer

The tensile specimens were unstressed and examined under a stereomicroscope for defects such as corrosion layers or cracks. On selected specimens a metallographic section was prepared.

3.4 Experimental set-up for permeation tests

The effective diffusion coefficient of hydrogen of carbon steels was determined by electrochemical permeation tests, which provide information about the trapping behavior of the material. The experiments were carried out in a double cell according to Devanathan and Stachurski. The parameters were chosen according to the ISO 17081:2014 standard for carbon steels. Since this is a very sensitive measurement, the entire experimental setup was located in a Faraday cage. The electrolyte in the charging cell was a 3.5 % NaCl solution with 1 g/l thiourea as promoter for hydrogen uptake and as well for a recombination poison, in the oxidation cell a 0.1 M NaOH solution was used as electrolyte. Both solutions were purged with Ar for 24 hours before the experiment in order to be free of oxygen. The hydrogen loading was carried out galvanostatically using a Gamry Reference 600 potentiostat, in the oxidation cell potentiostatic was also measured by a potentiostat of the same company over the duration of the experiment. The electrolyte was purged with Ar for the entire duration of the experiment in order to minimize the oxygen content in the solution and prevent the formation of an oxide layer on the sample surface. Square shaped samples with a cross-section of 40 x 40 mm and a thickness of 1.1 mm were produced for the permeation measurement. The permeation samples were brought to final thickness by grinding with SiC

abrasive paper #1000 and a final thickness of 1 ± 0.01 mm. The sample preparation of the thin membrane is time consuming, including the palladium coating with a 100 nm thick palladium layer. This was applied by physical vapour deposition, and it is mandatory to avoid corrosion and acts as a recombination blocker for H_2 on the oxidation side. With the help of a thermostat, both cells were set to 25 ± 2°C to influence the experiment as little as possible. The sample is considered as a membrane connected as working electrode on both charging and oxidation side. Each of the two half cells was operated with a platinum electrode as a counter electrode and a Ag/AgCl electrode as a reference electrode [73,74].

The test conditions are listed in Table 9 below and the experimental set-up in schematic form can be seen in Figure 46 as well as the real set-up is shown in Figure 47.

Table 9: Experimental parameters for permeation tests

Experimental parameters	
Electrolyte charging side	3.5 % NaCl + 1 Thiourea (CH_4N_2S) [g/l]
Charging current	1 mA/cm^2
Electrolyte oxidation side	0.1 M NaOH
Oxidation potential	546 mV
Counter electrode	Platin
Reference electrode	Ag/ AgCl
Sample thickness	1 ± 0.01 mm
Sample coating Pd	~ 100 nm
Temperatur	25 ± 2 °C
Area on charging side	1.389 cm^2
Area on oxidation side	1.108 cm^2
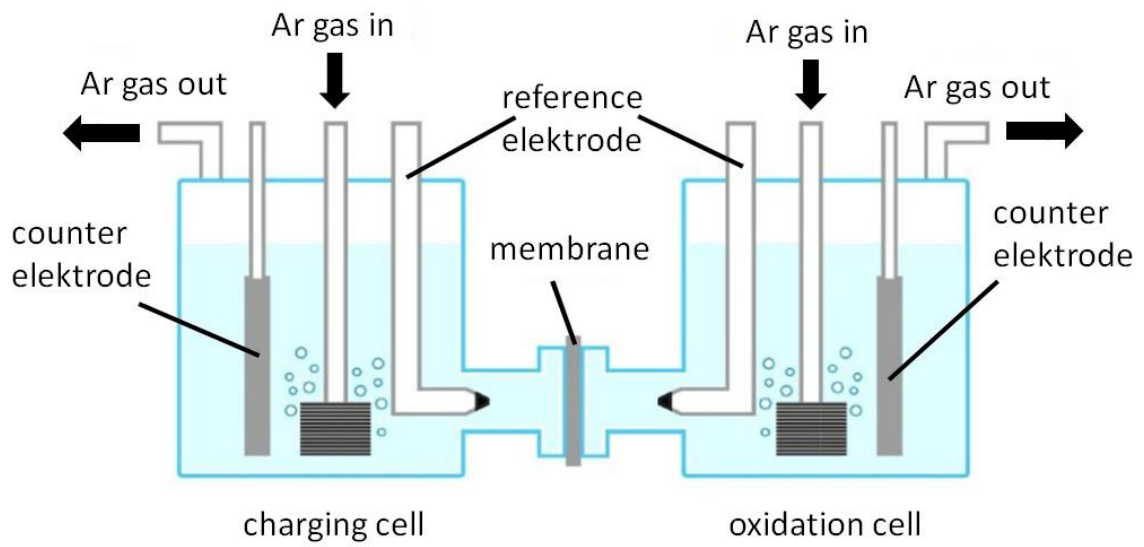
Figure 46: Schematic illustration of the used double cell according to Devanathan-Stachursky [75]
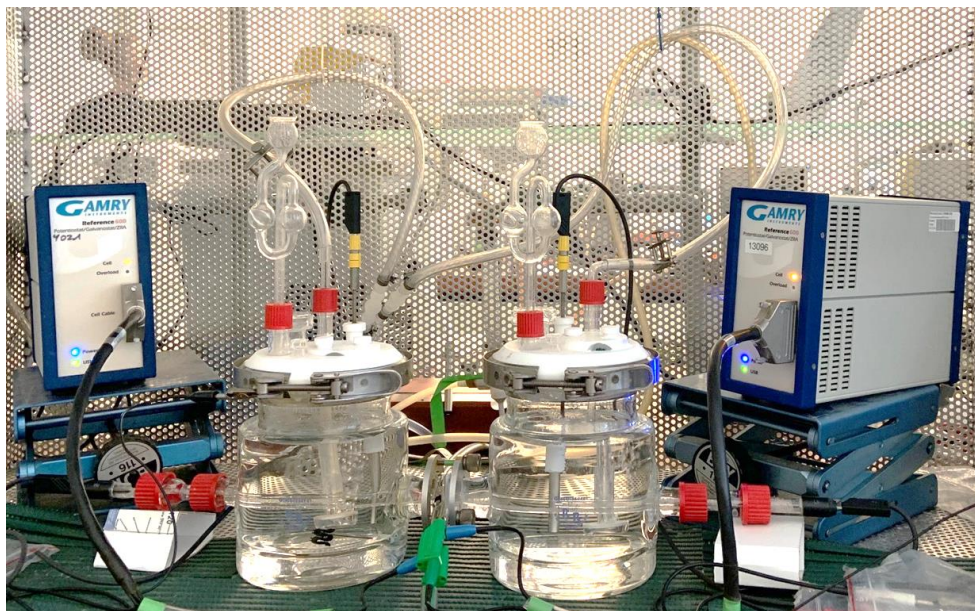
Figure 47: Experimental set-up for permeation tests

4 Results

4.1 Qualification material (quenched material)

A steel L80 was austenitized and then quenched in water. Due to quenching the material was made highly susceptible to hydrogen embrittlement. The existence of cracks in this material allows to crack reliability of the test set up to introduce HE.

CLT were carried out under three different conditions (Figure 48). Two of these tests ended in a failure of the material. Autoclaves have been opened only after testing after in total 720 h and therefore time to failure cannot be given. No failure occurred in dry gas A at 120 °C.
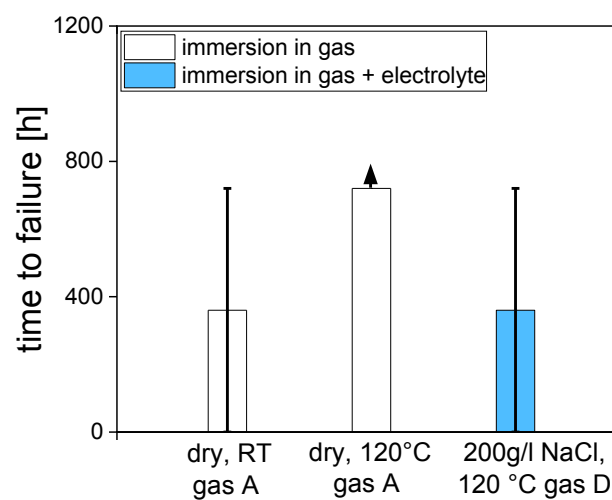
Figure 48: Time to failure of the quenched material after testing in gas A (120 bar H$_2$), without electrolyte, at room temperature and 120 °C; in gas D (120 bar H$_2$ + 15 bar CO$_2$ + 1 bar H$_2$S), 200 g/l NaCl, rotating at 120 °C

Figure 49 shows the hydrogen uptake under three different conditions for the quenched material.
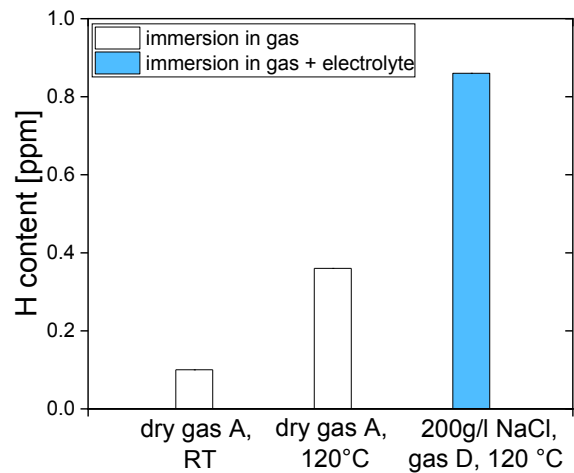
Figure 49: Hydrogen uptake of the quenched material after testing in gas A (120 bar H$_2$), without electrolyte, at room temperature and 120 °C; in gas D (120 bar H$_2$ + 15 bar CO$_2$ + 1 bar H$_2$S), 200 g/l NaCl, rotating at 120 °C

The hydrogen uptake in dry hydrogen gas A (120 bar H$_2$) at 25 °C is 0.1 ppm and 0.36 ppm at 120 °C. In H$_2$S containing gas D with the addition of 200 g/l NaCl solution the quenched carbon steel absorbed 0.86 ppm under the continuous application of wet-dry cycled at 120 °C. The blank hydrogen content was 0.2 ppm. This is in good agreement with the hydrogen content achieved by pressure charging in dry hydrogen gas at 25 °C. The value doubles when increasing the temperature from room temperature to 120 °C. If we add hydrogen sulfide and an electrolyte to the experimental conditions, the hydrogen uptake increases strongly compared to the blank value.

The fracture surface of the quenched material can be seen in Figure 50. At 120°C, test conditions were the most aggressive ones in gas D (H$_2$ + CO$_2$ + H$_2$S) with an electrolyte of 200 g/l sodium chloride NaCl. The fracture surface is covered by a thick layer of corrosion products. The hydrogen content in the sample after the test was 0.86 ppm.

Figure 50: Fracture surface of a quenched material at 120 °C with 200 g/l NaCl in gas D (120 bar H$_2$ + 15 bar CO$_2$ + 1 bar H$_2$S) and rotating

In Figure 51, the fracture surface of quenched steel tested in dry gas A (H$_2$) at 25 °C is shown. The fracture origin can be seen at the 12 o'clock position. A hydrogen content of only 0.10 ppm was measured with TDS.
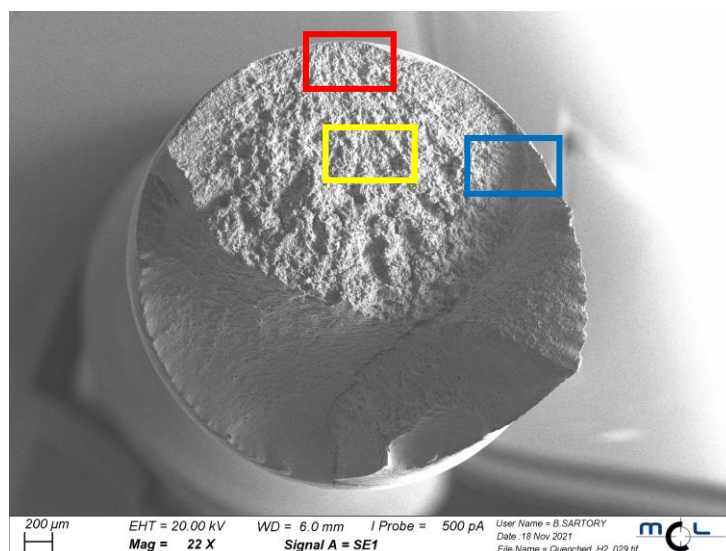
Figure 51: Fracture surface of a quenched material at RT in dry gas A (120 bar H$_2$)

a)

b)

c)

d)

e)

f)
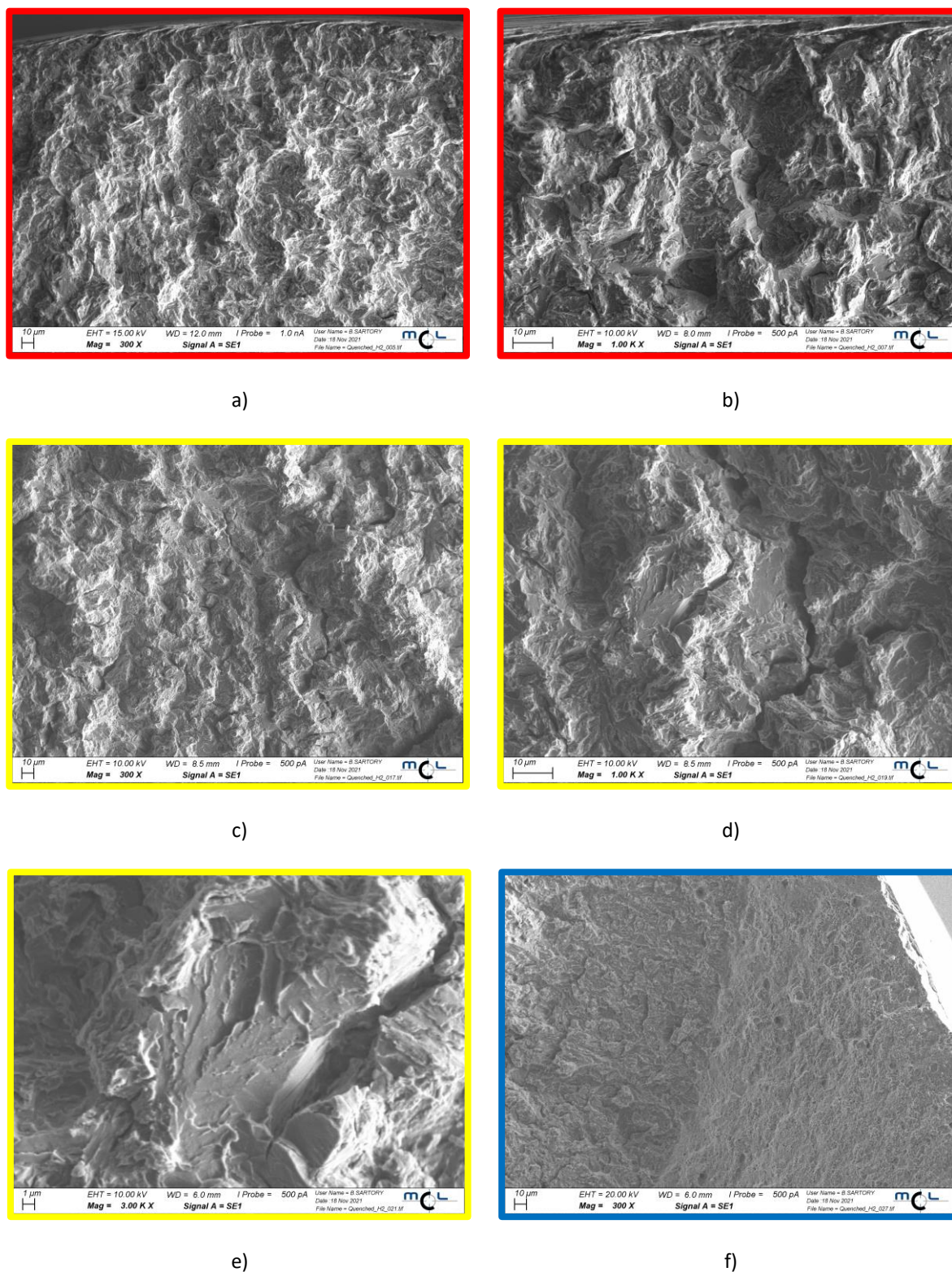
Figure 52. Fracture surface from quenched steel, in a) the origin of the fracture at a magnification of 300x, in b) a detail of the fracture origin at a magnification of 1000x, in c) the hydrogen fracture at 300x, d) & e) shows a detail of the hydrogen fracture with so river patterns at 1000x and 3000x, f) shows the transition zone between hydrogen fracture (left) and ductile forced fracture (right), 300x

Figure 52 shows the different fracture zones in detail in an SEM. A secondary electron image was used to observe the fracture surfaces more accurately. In Figure 52 a), in the red frame from Figure 51, the origin of the fracture in the 12 o'clock position with a magnification of 300x can be seen. In Figure 52 b) the same origin is visible at a larger magnification of 1000x. There is a mixed intergranular–transgranular fracture with open grain boundaries and some faceted quasi-cleavage fracture. In Figure 52 c) in the yellow frame a more transgranular fracture can be seen at a magnification of 300x. Figure 52 d) & e) shows the brittle fracture with the river patterns at larger magnifications 1000x and 3000x. In the blue area from Figure 52 f) the transition zone between the brittle hydrogen crack and a ductile forced fracture is visible.

4.2 Low strength carbon steels

For low strength steels, a common limit of 550 MPa is set for ultimate tensile strength. It is important to note that the classification of steels into low strength and high strength steels depends on various factors, such as chemical composition or heat treatment. However, this limit is not fixed and can vary depending on the application and industry. For example, in sheet metal production, a steel with a tensile strength of up to 620 MPa can be considered low strength, while in other industries this strength is already classified as high strength [155].

4.2.1 Steel 20MnV5

Figure 53 illustrates the time to failure in a CLT of ferritic pearlitic steel 20MnV5. There was no fracture under any of the tested conditions.
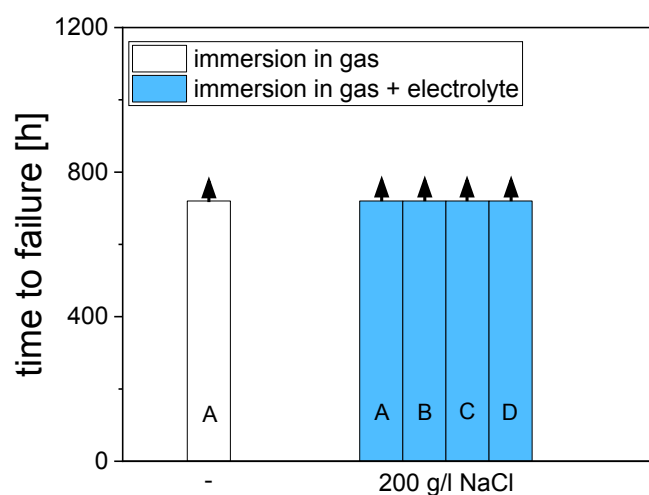
Figure 53: Time to failure in a CLT of a ferritic pearlitic steel 20MnV5 at room temperature in gas A (120 bar H_2), gas B (120 bar H_2 + 15 bar CO_2), gas C (120 bar H_2 + 1 bar H_2S) and gas D (120 bar H_2 + 15 bar CO_2 + 1 bar H_2S) with an electrolyte 200 g/l NaCl rotating and one dry condition with gas A (120 bar H_2)

Figure 54 shows a comparison between the hydrogen uptake in dry gas A and the gases A to D with the addition of 200 g/l NaCl solution in wet-dry cyclic testing. In the autoclave tests with the steel 20MnV5 at room temperature, the lowest value is 0.09 ppm for the dry gas A and the highest value is 2.71 ppm for the gas C with 200 g/l NaCl in the rotating autoclave. The blank value determined from an uncharged specimen is 0.11 ppm. Compared to the dry conditions it can be said that without the addition of an electrolyte there is almost no or very little hydrogen uptake. In both gases C and D there is a considerable hydrogen uptake, when an electrolyte is present. The reason for this is the dissociation of H_2S in the artificial brine and the formation of H^+ ions.
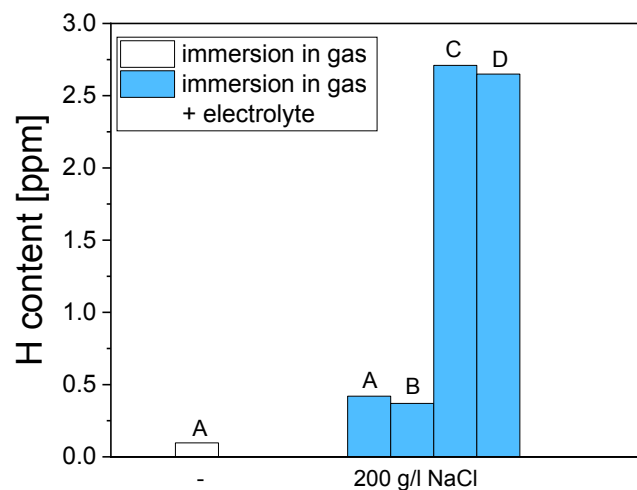
Figure 54: Hydrogen uptake of a ferritic pearlitic steel 20MnV5 at room temperature in gas A (120 bar H_2), gas B (120 bar H_2 + 15 bar CO_2), gas C (120 bar H_2 + 1 bar H_2S) and gas D (120 bar H_2 + 15 bar CO_2 + 1 bar H_2S) with an electrolyte 200 g/l NaCl rotating and one dry condition with gas A (120 bar H_2)

Figure 55 shows the cross-section of the ferritic pearlitic steel 20MnV5 from a tensile specimen at a magnification of 300x, tested at room temperature, rotating autoclave, salinity of 200 g/l NaCl in gas D. There is a certain localized attack in the form of shallow pitting. Depth of attack is not larger than 10 µm.
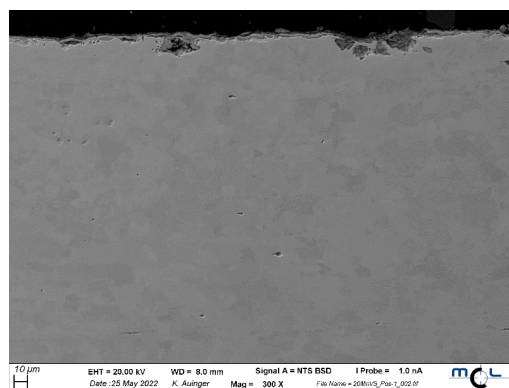
Figure 55: Cross section of steel 20MnV5 after the test in CLT with salinity of 200 g/l NaCl in gas D with a magnification of 300x

4.2.2 Welded J55

Hydrogen embrittlement can be accelerated in the presence of stress concentrations, such as those found in welding areas. For this reason, it was decided in the test program to investigate welded steels as well. The preheating temperature was set to 120 °C, and the interpass temperature ranged between 120 and 170 °C. There was no additional heat treatment (PWHT) after welding. As a consequence, it can be assumed that local stresses were not reduced. The hardness of the weld represents hardness values ranging from 162 to 458 HV1, with the highest value located in the top layer. For all welded specimens the weld was located in the center of the gauge length of the tensile specimen and in the center of the cuboid specimen for hydrogen analysis [32].

Figure 56 shows the time to failure in gas D (120 bar H_2 + 1 bar H_2S + 15 bar CO_2) at room temperature. No fracture occurred under any condition. There were no cracks in the welded steel J55. Apart from results shown about gas D in Figure 56 welded J55 was also tested in gases A, B and C. Results were the same for all gases like shown in Figure 56. No fractures at all occurred. Additionally to the tests at 25 °C the material was also investigated at 120 °C under equivalent conditions regarding the applied gases and electrolytes. Also none of the specimens tested at elevated temperature failed.
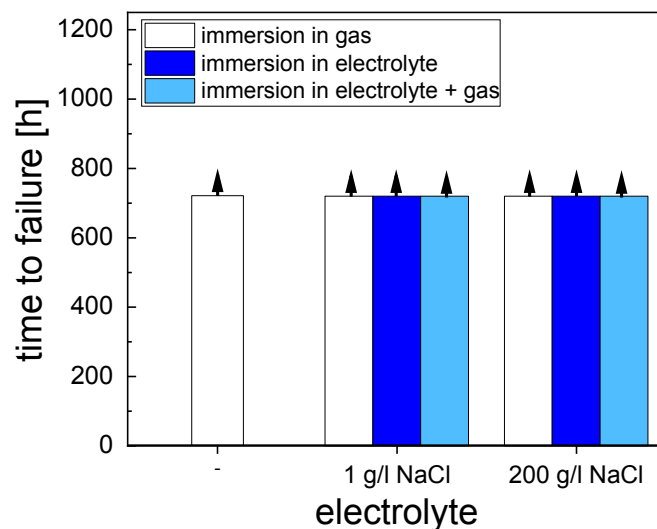
Figure 56: Time to failure of a welded ferritic pearlitic steel J55 in gas D (120 bar H_2 + 15 bar CO_2 + 1 bar H_2S) at room temperature

Figure 57 shows the time to failure in a CLT in the dry hydrogen gas at 120 bar and also rotating autoclaves with a salt content of 200 g/l NaCl in gas A (120 bar H_2), gas B (120 bar H_2 + 15 bar CO_2), gas C (120 bar H_2 + 1 bar H_2S) and gas D (120 bar H_2 + 15 bar CO_2 + 1 bar H_2S), at room temperature. Like in Figure 57 the time to failure of the

welded ferritic pearlitic steel J55 for pre-corroded samples as well for notched specimens looked the same. No fracture occurred under any of the tested conditions.
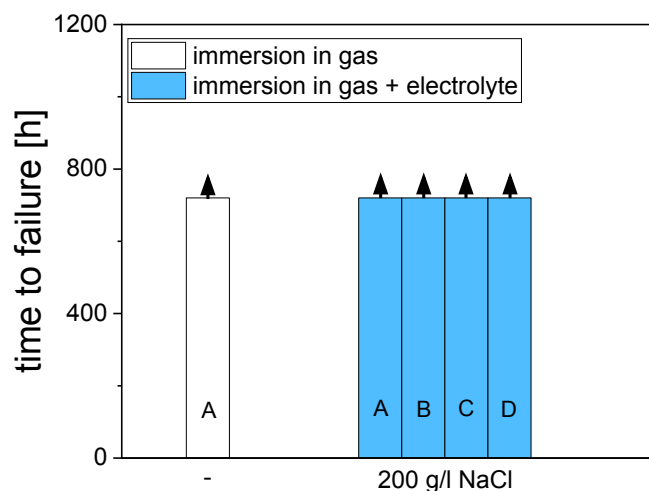
Figure 57: Time to failure of a ferritic pearlitic steel welded J55 at room temperature in gas A (120 bar H$_2$), gas B (120 bar H$_2$ + 15 bar CO$_2$), gas C (120 bar H$_2$ + 1 bar H$_2$S) and gas D (120 bar H$_2$ + 15 bar CO$_2$ + 1 bar H$_2$S) with an electrolyte 200 g/l NaCl rotating and one dry condition with gas A (120 bar H$_2$)

Figure 58 depicts the hydrogen uptake in a) gas A and b) gas B at room temperature. Figure 58 c) depicts the uptake in gas C, while Figure 58 d) depicts the hydrogen content following exposure to gas D. The lowest hydrogen content determined in the autoclave tests on welded steel J55 at room temperature was 0.12 ppm for gas A. The highest content was 2.95 ppm and determined after immersion in gas D. In autoclave tests with welded steel J55 at 120 °C, the lowest value is 0.35 ppm in gas A and the highest value is 2.08 ppm in gas C. The lowest value for the pre-corroded material was 1.07 ppm in the dry gas A and the highest value was 3.32 ppm for immersion in gas D, shown in Figure 58 e). The measured blank value of the material was 0.65 ppm. In the autoclaves with gases A and B, almost no hydrogen absorption was observed at low temperatures. However, higher temperatures indicate a higher hydrogen uptake in these gases. Measurements of specimens charged in gas C show significant hydrogen uptake at both temperatures. Due to the dissolution of H$_2$S in the brine, the pH dropped and caused a higher hydrogen uptake. Figure 58 depicts the results of hydrogen uptake of the steel J55 under all conditions after autoclave testing.

Overall, it can be seen that the ferritic-pearlitic welded steel J55 has a higher hydrogen uptake than the ferritic-pearlitic steel without weld. This could be due to the heat treatment by welding. It is found that the hydrogen uptake of pre-corroded welded steel J55 is similar to the one of pre-corroded steel K55. The welding appears to have no additional effect on the pre-corroded samples, while it affects the not welded one.

Images a) and c) of Figure 59 and Figure 60 show backscattered electron detector (BSD) SEM images of the cross-section of the ferritic-pearlitic welded steel J55 after the test in gases without H_2S. Figure 59 and Figure 60 b) and d) show the element mappings of welded steel J55 after tests in gases A and B. Figure 61 and Figure 62 a) and d) show the BSD cross section image of the welded J55 with gases with additional H_2S. Figure 61 and Figure 62 b-c) and e-f) show element mappings of the welded steel in gas C and D.

Figure 63 shows the welded steel J55 with a notch after 30 days of exposure in gas D, a) is a BSD image of the notch and b-c) are element mappings. Figure 63 d) shows a cross section BSD image at the pre-corroded sample at 120 °C, e-f) show the element mapping for the pre-corroded sample at higher temperature in gas D. In addition to the SEM examinations, images of the surface of the tensile specimens were taken, and are given in the appendix.

All BSD images and element mappings shown were carried out with the addition of 200 g/l NaCl solution under alternating immersion conditions for 30 days. In the case of the tests without hydrogen sulfide, only an oxide or hydroxide layer is formed during the experiments, as shown in Figure 59 and Figure 60. The layer of corrosion products is thicker at room temperature when compared to the one formed at 120 °C. No local corrosive attack from the surface is visible at any temperature. In the tests with H_2S, mixed layer containing oxides and sulfides are formed on the surface of the sample. There is a certain localized attack with lower than 10 µm in gas D (Figure 62 d).

The welded notched steel J55 shows a 40-50 µm thick layer consisting of two sublayers of an oxide and a sulfide layer on the surface. There is again very little localized attack (below 10 µm), as can be seen in Figure 63 a). Consequently, the welding does not increase localized attack at the notch tip. Figure 63 d) shows a cross-section of the pre-corroded steel J55 after the test. There is a homogeneous oxide-sulfide layer with a thickness of 40 to 50 µm. The layer consists of two sub-layers, the inner oxide one is homogeneous while the outer sulfide is more heterogeneous.

The SEM analysis of the steel surface shows that there is a very low localized damage attack at conditions in gas D. The cross-section of welded steel J55 in all other conditions shows no localized attack.
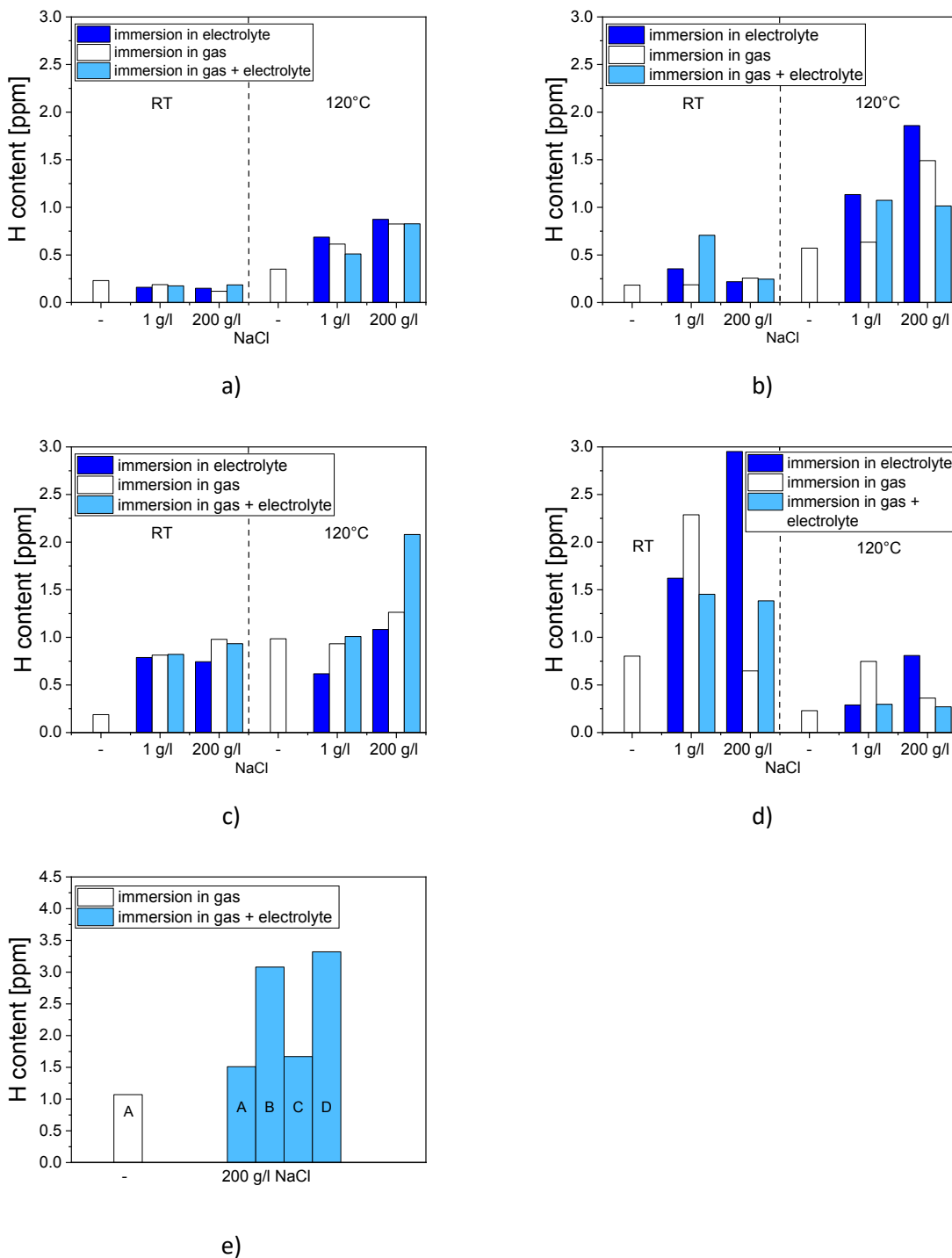
Figure 58: Hydrogen uptake after 30-day immersion of a welded steel J55 in different gases and electrolytes at 25 and 120 °C; a) gas A (120 bar H_2), b) gas B (120 bar H_2 + 15 bar CO_2), c) gas C (120 bar H_2 + 1 bar H_2S) and d) gas D (120 bar H_2 + 15 bar CO_2 + 1 bar H_2S); e) shows the welded pre-corroded steel J55 at room temperature in dry gas A and with an electrolyte (200 g/l NaCl) rotating in gas A, gas B, gas C and gas D
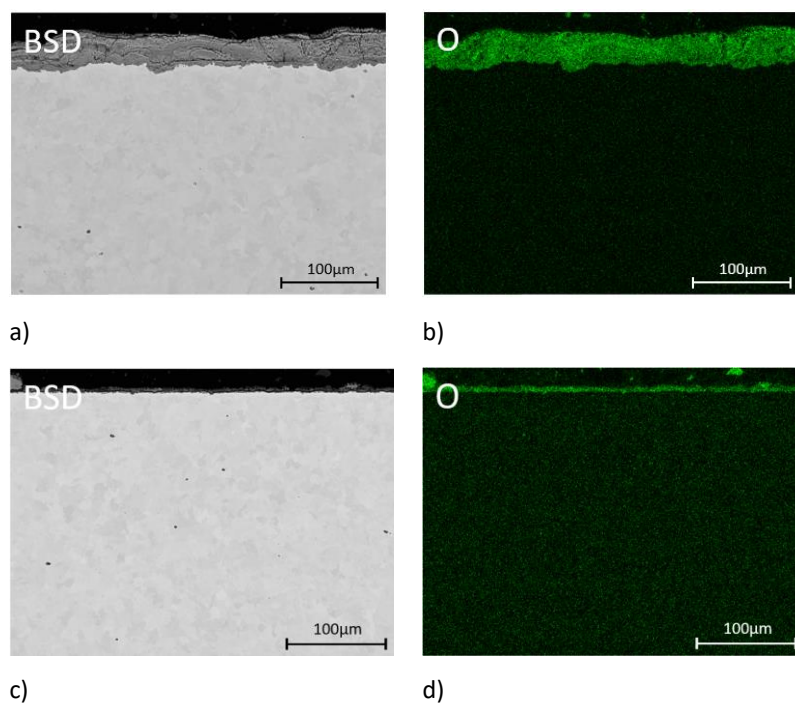
Figure 59: Welded steel J55 after 30 days exposure in gas A (120 bar H₂) a) BSD image after testing at RT b) element mapping after testing at RT; c) BSD image after testing at 120 °C and d) element mapping after testing at 120 °C
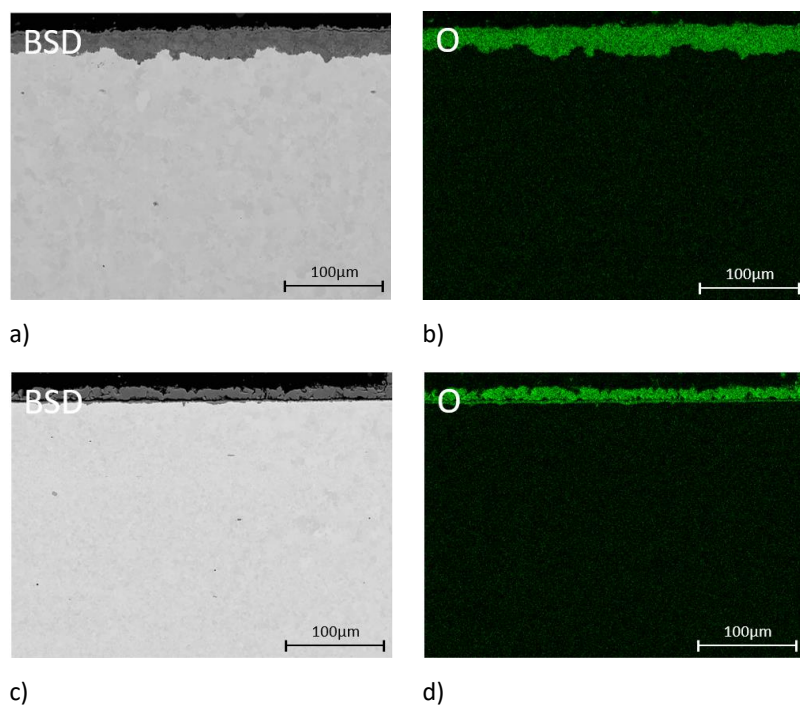
Figure 60: Welded steel J55 after 30 days exposure in gas B (120 bar H₂ + 15 bar CO₂) after testing a) BSD image at RT b) element mapping at RT; c) BSD image at 120 °C d) element mapping at 120 °C
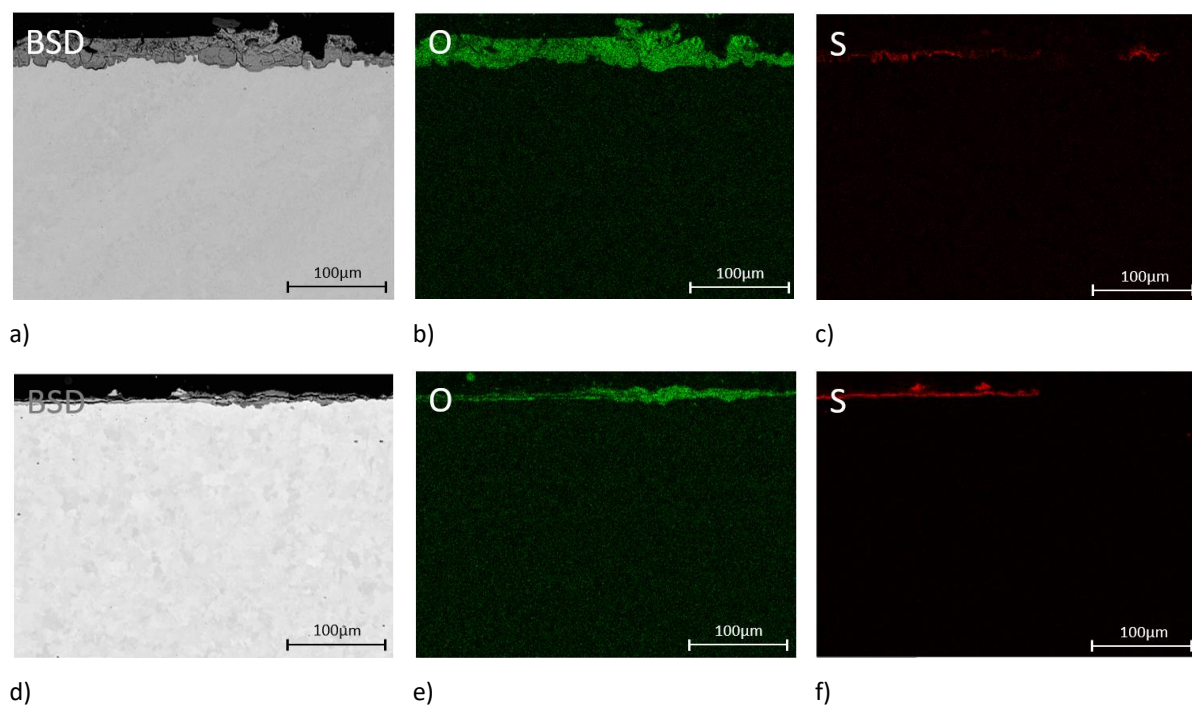
Figure 61: Welded steel J55 after 30 days exposure in gas C (120 bar H$_2$ + 1 bar H$_2$S) after testing a) BSD image at RT b-c) element mapping at RT; d) BSD image at 120 °C and e-f) element mapping at 120 °C
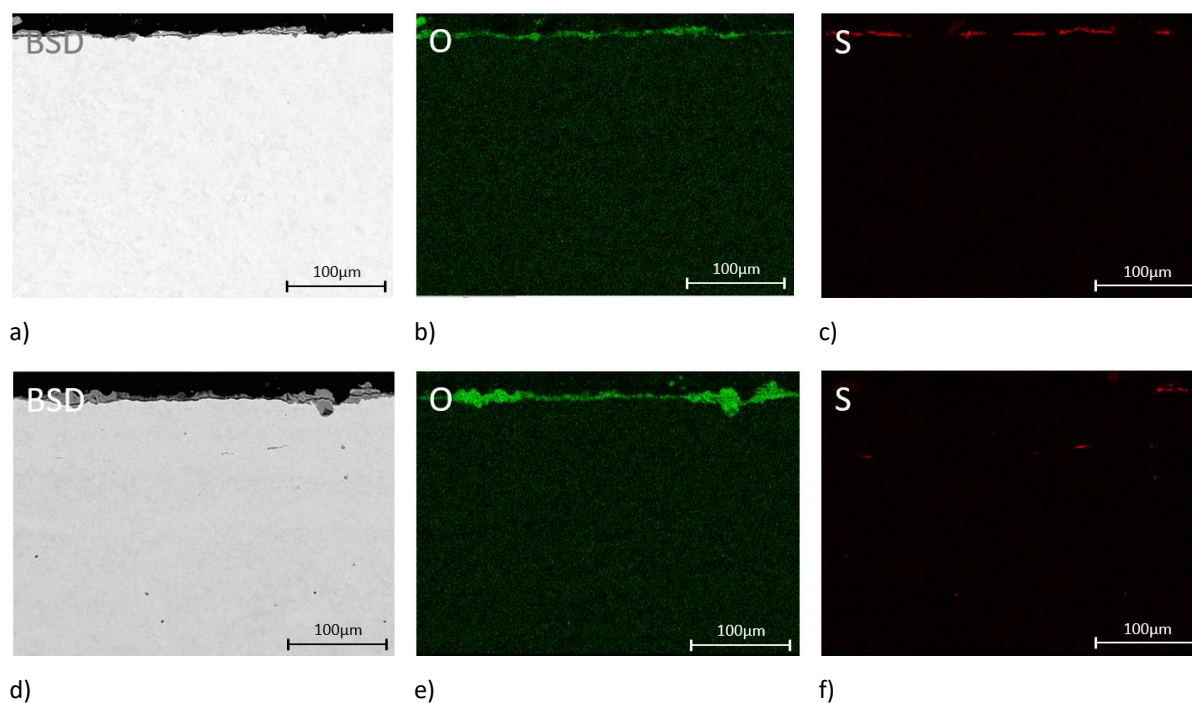
Figure 62: Welded steel J55 after 30 days exposure in gas D (120 bar H$_2$ + 15 bar CO$_2$ + 1 bar H$_2$S) after testing a) BSD image at RT b-c) element mapping at RT; d) BSD image at 120 °C and e-f) element mapping at 120 °C
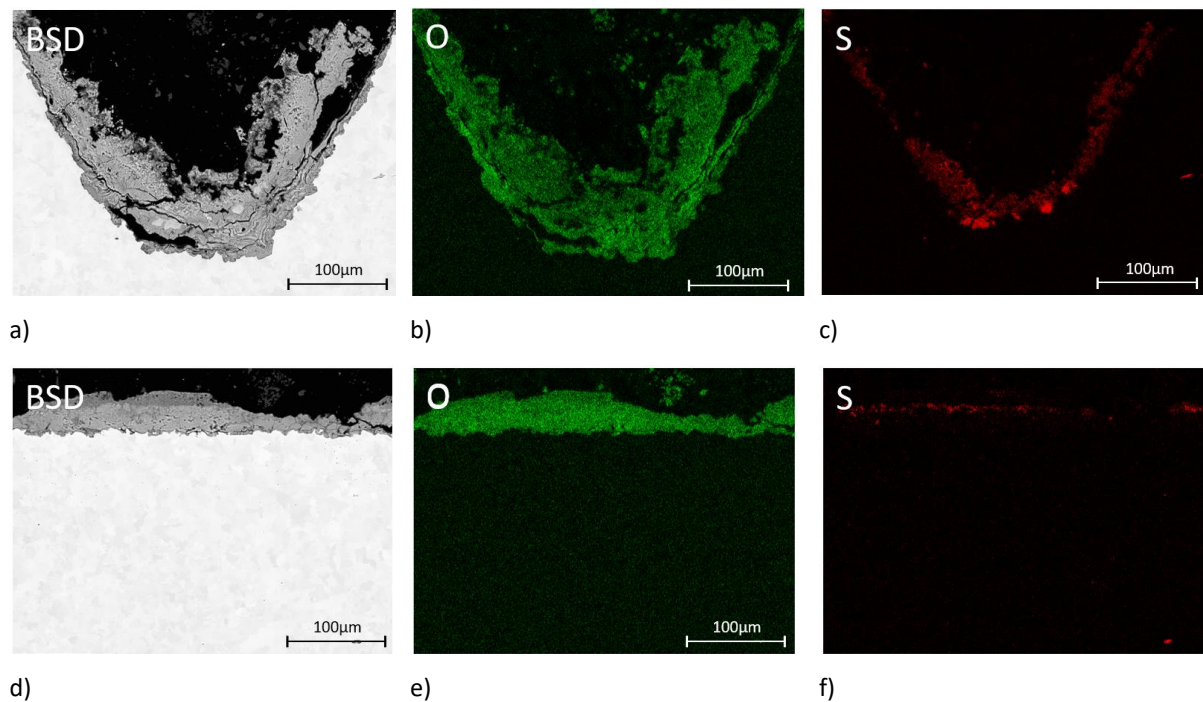
Figure 63: Welded steel J55 after 30 days exposure in gas D (120 bar H₂ + 15 bar CO₂ + 1 bar H₂S) after testing at RT a) BSD image at the notch and b-c) element mapping; d) BSD image of the pre-corroded sample, e-f) element mapping

To complete the material examination, the effective hydrogen diffusion coefficient was determined by performing a permeation test, which provided information about the trapping behaviour of the material. The permeation test was carried out in a Devanathan-Stachursky cell according to ISO 17081 [74]. Figure 64 depicts the results of the hydrogen permeation tests on welded steel J55. Figure 64 a) shows the permeation current as a function of time for two consecutive loads. Figure 64 b) shows the first loading with hydrogen in a magnification. The evaluation of the data with determination of the lag time is also included. Figure 64 c) shows a magnification of the permeation current as a function of time, including as well the evaluation of the second loading.

The first loading gave an effective diffusion coefficient D_{eff} of $1.69 \cdot 10^{-6} \frac{cm^2}{s}$, while the second coefficient resulted in a value of $2.36 \cdot 10^{-6} \frac{cm^2}{s}$.
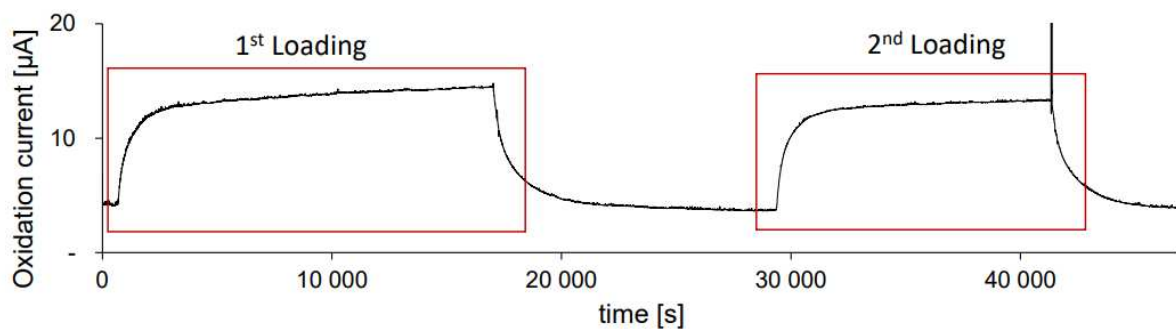
a)
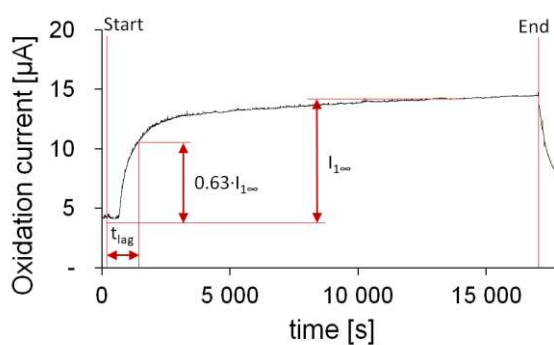
b)
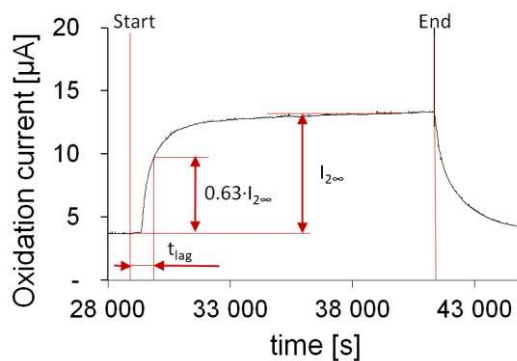
c)

Figure 64: Hydrogen permeation current as function of time for the welded steel J55 a) Overview of two charging cycles; b) Detail of the first charging cycle; and c) Detail of the second charging cycle

4.2.3 Steel K55

The time to failure in a CLT for ferritic pearlitic steel K55 is shown in Figure 65. As an example, for all tested conditions, Figure 65 shows the time to failure in gas D at room temperature. The same results were achieved when testing steel K55 in gas A (120 bar H_2), B (120 bar H_2 + 15 bar CO_2) and C (120 bar H_2 + 1 bar H_2S) for all tested temperatures. No fracture occurred under any condition. There were no cracks as well in steel K55 after autoclave testing.
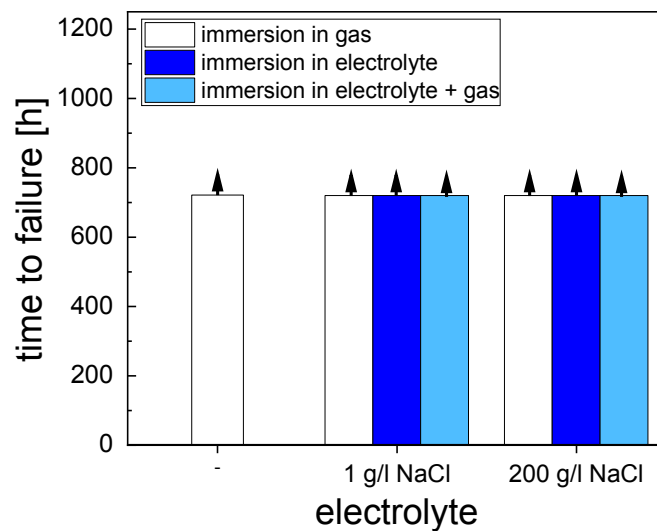
Figure 65: Time to failure in a CLT of ferritic pearlitic steel K55 in gas D (120 bar H_2 + 15 bar CO_2 + 1 bar H_2S) at RT

Figure 66 compares the hydrogen absorption of steel K55 at room temperature to a higher temperature (25 °C) and at 120 °C in all test gases. In the autoclave test series with steel K55 at room temperature, the lowest hydrogen value was 0.07 ppm for gas A and the highest value was 2.33 ppm when immersed in gas C. If H_2S is present, the hydrogen content increase when an electrolyte is present. H_2S has almost no effect on hydrogen uptake when no electrolyte is present. Gases C and D resulted in higher hydrogen contents than gases A and B in the presence of an electrolyte at room temperature. In autoclave tests with the steel K55 at higher temperatures, the lowest value is 0.19 ppm in gas B and the highest value is 0.49 ppm in gas D, while the blank value is 0.22 ppm. The hydrogen content was determined using TDS.

In contrast, the addition of H_2S to the gas resulted in a faster sulfide layer formation at 120°C and, as a result, a reduction of hydrogen uptake when compared to room temperature tests. The lowest hydrogen value for the pre-corroded sample in the autoclave tests is 0.67 ppm and the highest value is 3.64 ppm after immersion in gas B. Pre-corrosion resulted in an increased hydrogen uptake also in dry conditions with 120 bar H_2 saying for a pronounced hydrogen uptake during these pretreatment (Figure 66 e)). Nevertheless no cracking at all occurred for pre-corroded specimens.

Figure 67 to Figure 70 show results of SEM investigation on steel K55 in 4 investigated gases. In Figure 71, the steel K55 with a notch is shown after 30 days exposure to gas D.

There are always first the BSD images and then element mappings, first for room temperature and then for 120 °C. After testing in pure H_2 (Gas A) or $H_2 + CO_2$ (Gas B) there is always a rather thin layer of oxide/ hydroxide. In H2S containing gases there is additionally a layer of sulfide on the surface and in total the layers are thicker than the pure oxide layers in Gas A and B.

Layer thickness is larger at room temperature than at 120 °C. This is valid for Gas A, B and C. Gas D there might have been some spalling of the layers at room temperature. Figure 70 a) shows some locally thicker areas of layers indicating such a spalling.

To investigate the cause of varying hydrogen contents after immersion under different conditions, the surface layers formed during the test was characterized by SEM.

Figure 71 a) shows a non-uniform layer formation with a maximum thickness of up to 150 µm in the notch. The localized corrosive attack in the notch was up to 30 µm. In Figure 71 d) a cross-section of the pre-corroded steel K55 after the test is shown. There is a homogeneous oxide-sulfide layer with a thickness of up to 100 µm. The layer consists of two sub-layers, a homogeneous oxide layer, close to the material surface and a heterogeneous sulfide layer. The cross-sections of all the steel surfaces tested show that there is very little localized attack, below 5 µm, with the exception of the notched specimen (up to 30 µm) and the pre-corroded sample (up to 15 µm), which were tested in gas D at 25 °C.

a)

b)

c)

d)

e)
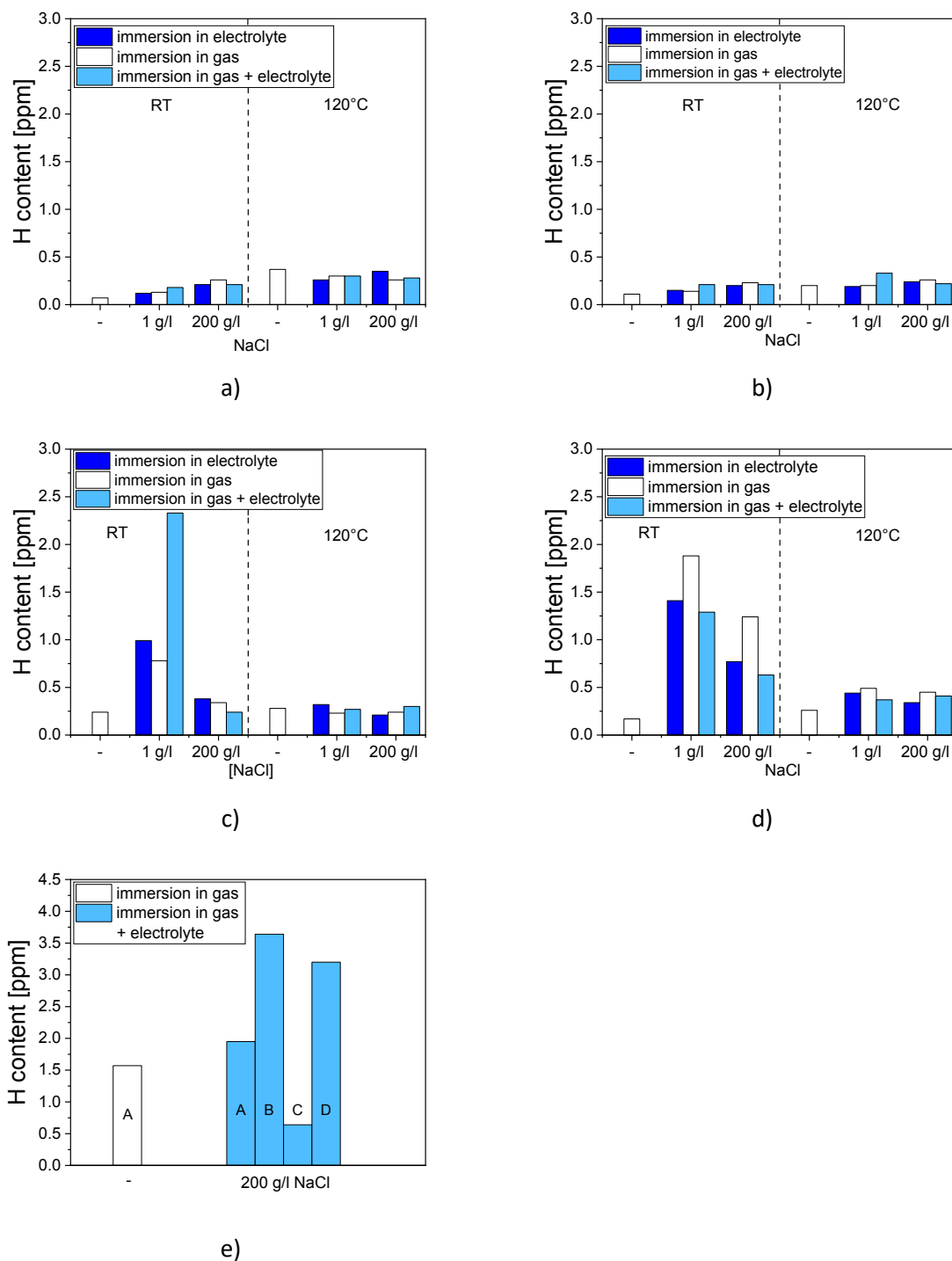
Figure 66: Hydrogen uptake after 30-day immersion of a steel K55 in different gases, electrolytes and salinity at different temperatures; a) gas A (120 bar H₂), b) gas B (120 bar H₂ + 15 bar CO₂), c) gas C (120 bar H₂ + 1 bar H₂S) and d) gas D (120 bar H₂ + 15 bar CO₂ + 1 bar H₂S); e) shows the pre-corroded steel K55 at room temperature in the dry condition with gas A, with an electrolyte of 200 g/l NaCl rotating in gas A, gas B, gas C and gas D

a)

b)

c)

d)
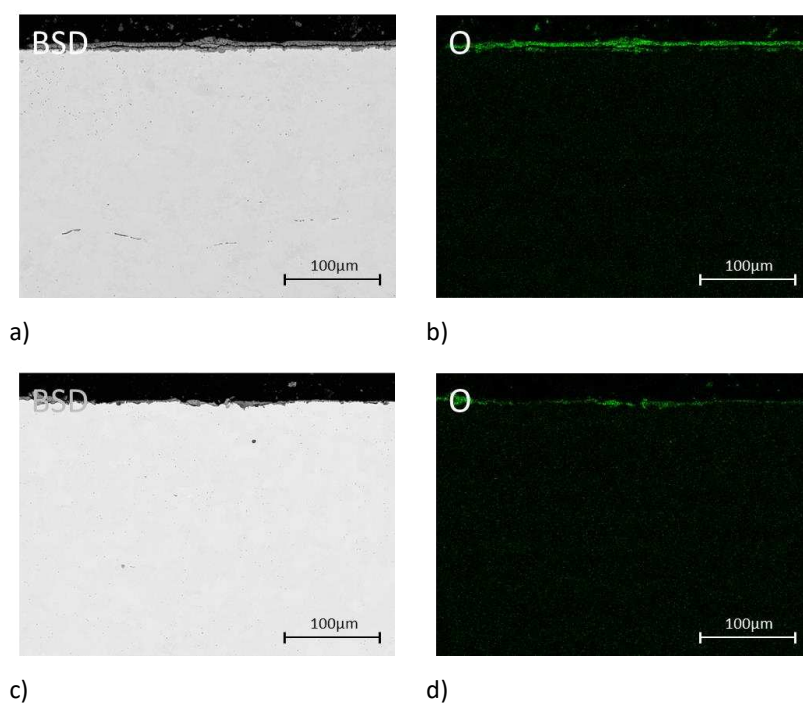
Figure 67: Steel K55 after 30 days exposure in gas A (120 bar H$_2$) a) BSD image after testing at RT b) element mapping after testing at RT; c) BSD image after testing at 120 °C and d) element mapping after testing at 120 °C

a)

b)

c)

d)
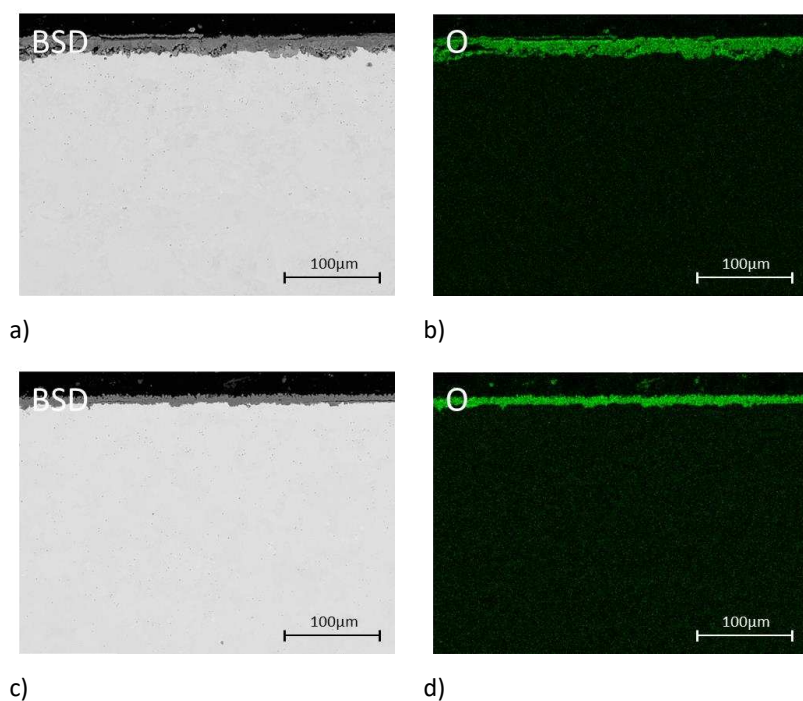
Figure 68: Steel K55 after 30 days exposure in gas B (120 bar H$_2$ + 15 bar CO$_2$) after testing a) BSD image at RT b) element mapping at RT; c) BSD image at 120 °C d) element mapping at 120 °C
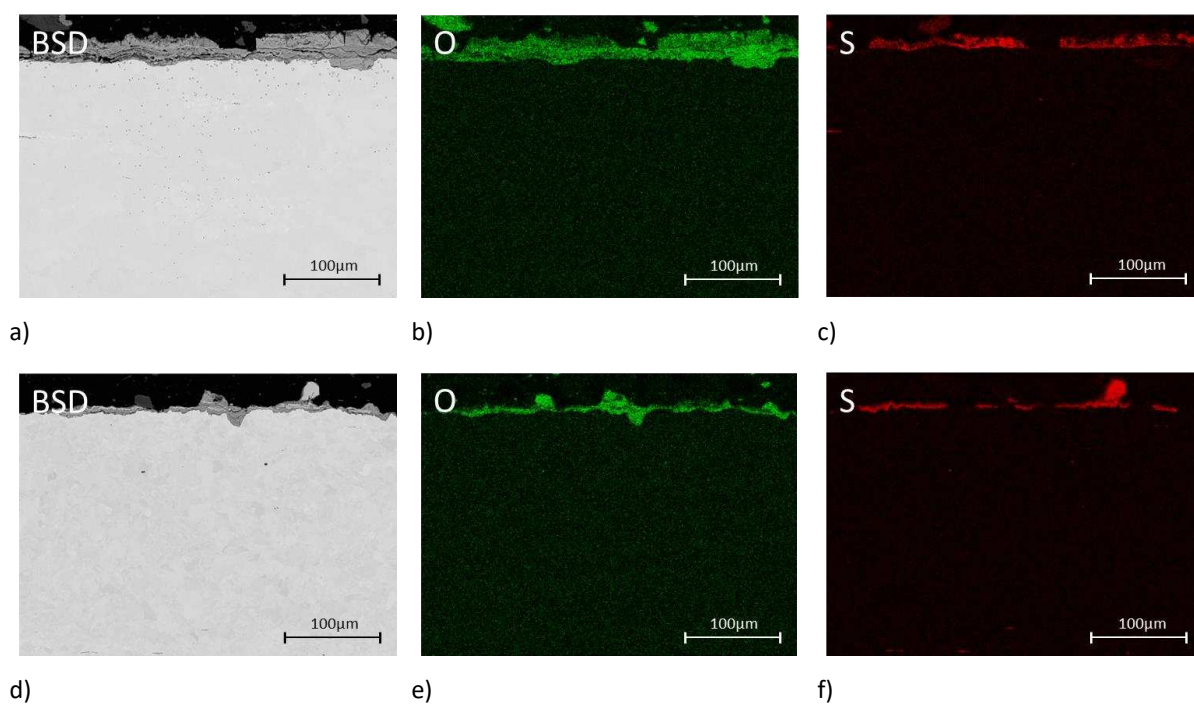
Figure 69: Steel K55 after 30 days exposure in gas C (120 bar H$_2$ + 1 bar H$_2$S) after testing a) BSD image at RT b-c) element mapping at RT; d) BSD image at 120 °C and e-f) element mapping at 120 °C
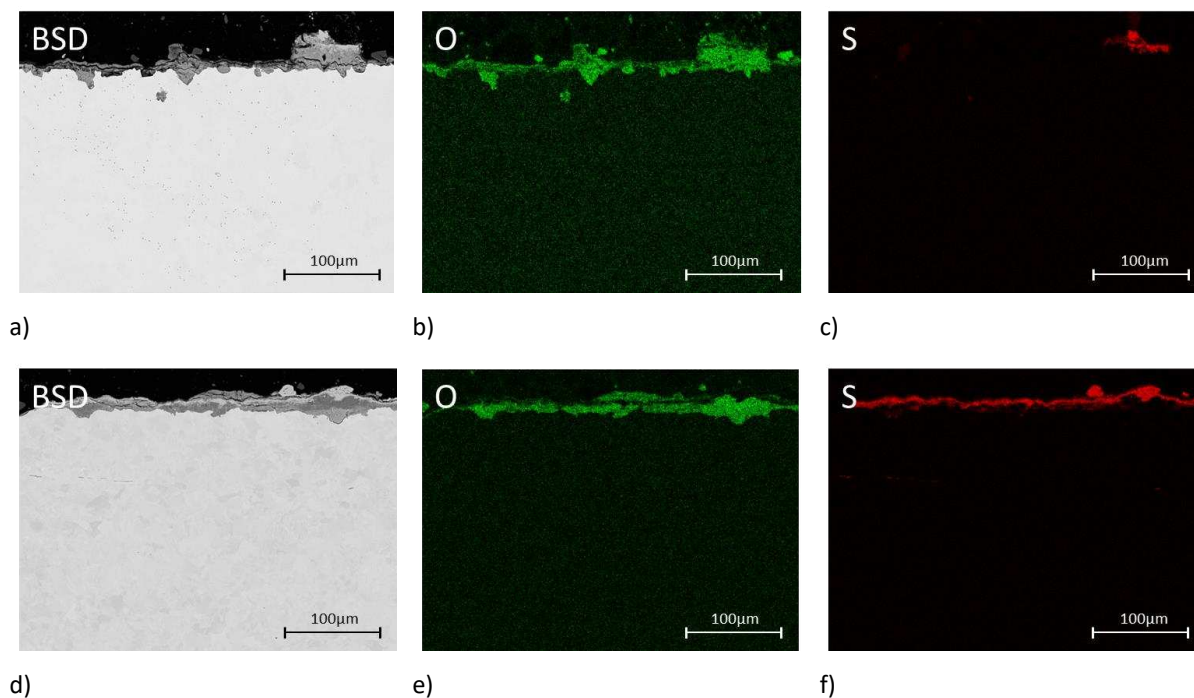
Figure 70: Steel K55 after 30 days exposure in gas D (120 bar H$_2$ + 15 bar CO$_2$ + 1 bar H$_2$S) after testing a) BSD image at RT b-c) element mapping at RT; d) BSD image at 120 °C and e-f) element mapping at 120 °C
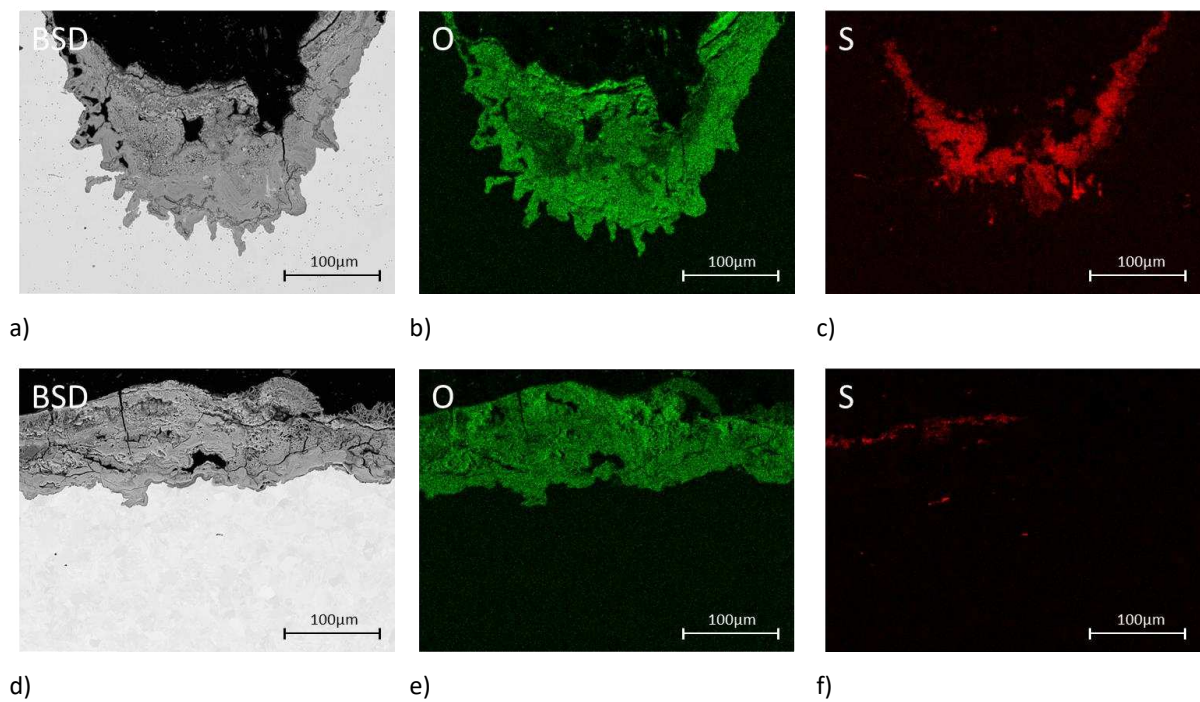
Figure 71: Steel K55 after 30 days exposure in gas D (120 bar H$_2$ + 15 bar CO$_2$ + 1 bar H$_2$S) after testing at RT a) BSD image at the notch and b-c) element mapping of the notch; d) BSD image at of the pre-corroded sample, e-f) element mapping of the pre-corroded sample

In order to complete the material investigation, the effective diffusion coefficient was determined by measuring the oxidation current over time. Figure 72 depicts the results of hydrogen permeation tests on steel K55. Figure 72 a) shows results from permeation tests as function of time for two consecutive loadings, Figure 72 b) depicts a detail of the permeation current for the first loading, and Figure 72 c) shows the same for the second loading. The evaluation is also included in Figure 72 b) and c).

The first loading gave an effective diffusion coefficient D_{eff} of $6.22 \cdot 10^{-6} \frac{cm^2}{s}$, and the second a D_{eff} of $7.96 \cdot 10^{-6} \frac{cm^2}{s}$.
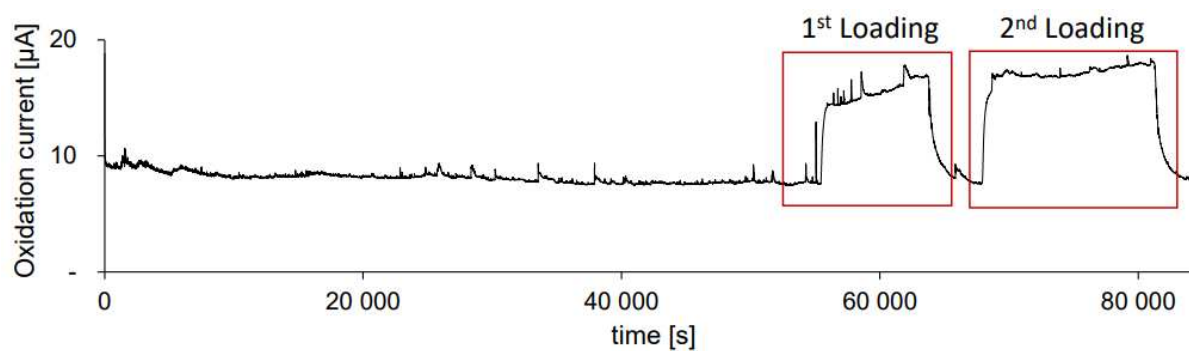
a)
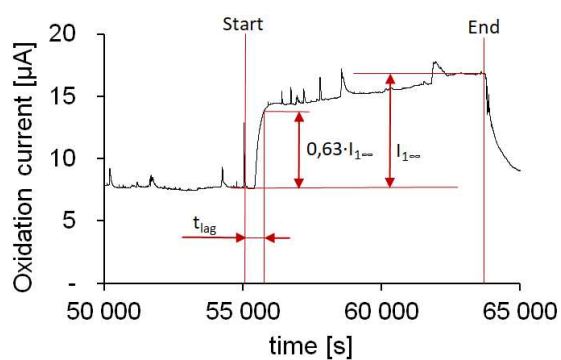
b)
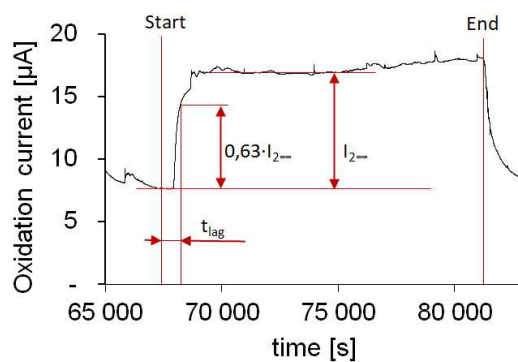
c)

Figure 72: Hydrogen permeation current as function of time for steel K55 a) Overview over both charging cycles; b) Detail of the first charging cycle; and c) Detail of the second charging cycle

4.2.4   Welded K55

As in the case of steel grade J55, a weld with a V-joint was also carried out on steel grade K55. The preheating temperature has been set to 110 °C and the interpass temperature was maximal 235 °C. No post-weld heat treatment (PWHT) was done.

Figure 73 illustrates the time to failure of the welded ferritic pearlitic steel K55. There was no fracture under any test condition.
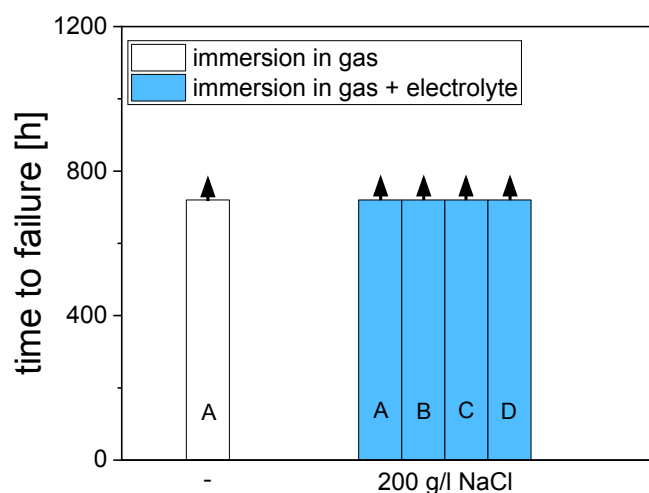
Figure 73: Time to failure in a CLT of a welded ferritic pearlitic steel K55 at room temperature in gas A (120 bar H$_2$), gas B (120 bar H$_2$ + 15 bar CO$_2$), gas C (120 bar H$_2$ + 1 bar H$_2$S) and gas D (120 bar H$_2$ + 15 bar CO$_2$ + 1 bar H$_2$S) with an electrolyte 200 g/l NaCl rotating and one dry condition with gas A (120 bar H$_2$)

Figure 74 shows the corresponding hydrogen uptake. The lowest measured hydrogen value is 1.03 ppm for dry gas A and the highest value is 2.69 ppm for immersion in gas C, the blank value for hydrogen is 0.49 ppm. Although there is a hydrogen uptake between 0.5 and 2.2 ppm no cracking at all did occur for the welded K55 material.
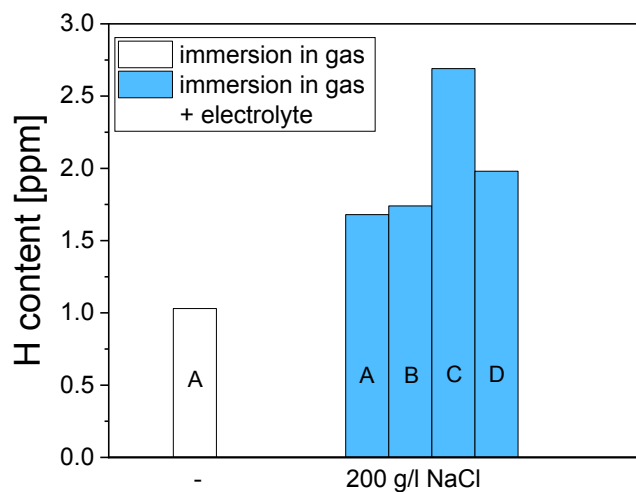
Figure 74: Hydrogen uptake of a welded ferritic pearlitic steel K55 at room temperature in gas A (120 bar H$_2$), gas B (120 bar H$_2$ + 15 bar CO$_2$), gas C (120 bar H$_2$ + 1 bar H$_2$S) and gas D (120 bar H$_2$ + 15 bar CO$_2$ + 1 bar H$_2$S) with an electrolyte 200 g/l NaCl rotating and one dry condition with gas A (120 bar H$_2$)

Figure 75 shows a cross section of the welded steel K55 at room temperature in Gas D (120 bar H$_2$ + 15 bar CO$_2$ + 1 bar H$_2$S) with a salinity of 200 g/l NaCl at a magnification of 300x with the standard detector, BSD.
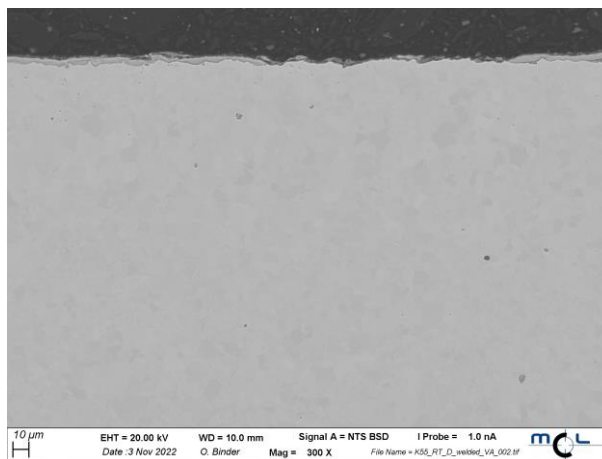
Figure 75: SEM analysis of a welded steel K55 at RT in Gas D (120 bar H$_2$ + 15 bar CO$_2$ + 1 bar H$_2$S) with a salinity of 200 g/l NaCl with a magnification of 300x

The cross-section in Figure 75 shows that there is no localized attack starting from the surface.

In addition to autoclave tests, permeation tests were performed to determine how welding affects processes diffusion. Effective diffusion coefficient has been determined in the described way via the lag time method. Figure 76 depicts the results of hydrogen permeation tests on a welded ferritic pearlitic steel K55.
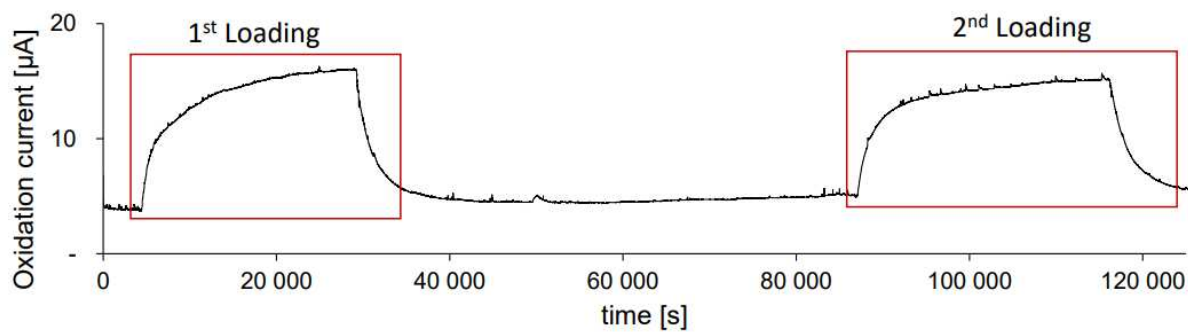
a)
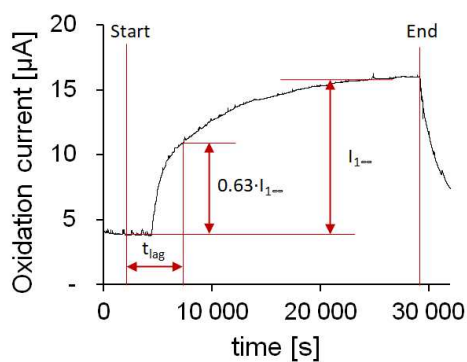
b)
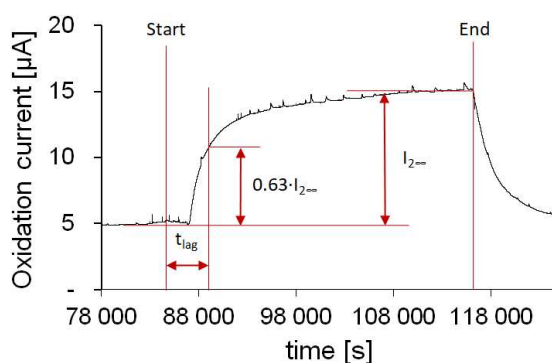
c)

Figure 76: Hydrogen permeation current as function of time for the welded steel K55 a) Overview of two charging cycles; b) Detail of the first charging cycle; and c) Detail of the second charging cycle

The first loading resulted in an effective diffusion coefficient of $D_{eff} = 4.57 \cdot 10^{-7} \frac{cm^2}{s}$, while the second loading resulted in a $D_{eff} = 6.50 \cdot 10^{-7} \frac{cm^2}{s}$.

4.3 High strength carbon steels

Steels with an ultimate tensile strength higher than 550 MPa are frequently designated as high strength steels in oil and gas industry. It has to be noted that, this classification is not fixed and can vary depending on application and industry.

4.3.1 Steel L80

The time to failure in CLT of the tempered steel L80 is shown in Figure 77. As an example, Figure 77 describes the time to failure in gas D at room temperature. No fracture at all occurred in 56 tests representing 7 conditions times 4 gases times 2 temperatures.
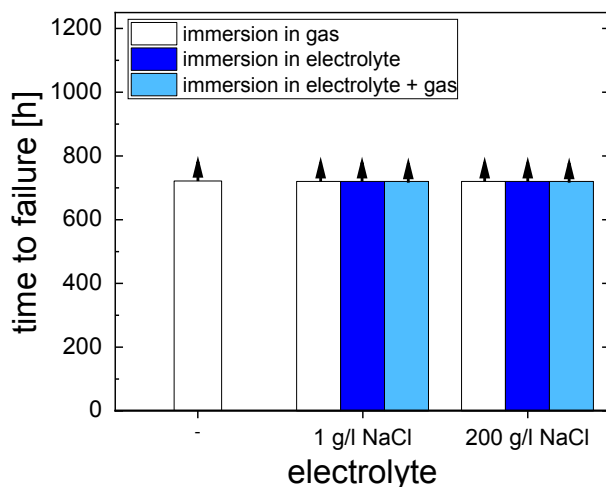
Figure 77: Time to failure in a CLT of a tempered steel L80 in gas D (120 bar H_2 + 15 bar CO_2 + 1 bar H_2S) at RT

Figure 78 shows hydrogen uptake for steel L80. The lowest value was 0.09 ppm in dry gas A and the highest measured value was 1.03 ppm. Some hydrogen uptake occurred in gases C and D at 25 °C when an electrolyte was present. This is due to the lowering of the pH of the solution by the effect of H_2S. At 120 °C, the lowest hydrogen value was 0.15 ppm and the highest value was 0.32 ppm. Even under conditions containing H_2S, the hydrogen concentrations in the steel are low compared to tests at room temperature. In comparison, the blank value was 0.22 ppm, which is only slightly higher than in the dry tests. The lowest value for the pre-corroded material was 1.51 ppm after immersion in gas A and the highest value was 3.55 ppm when immersed in gas B.
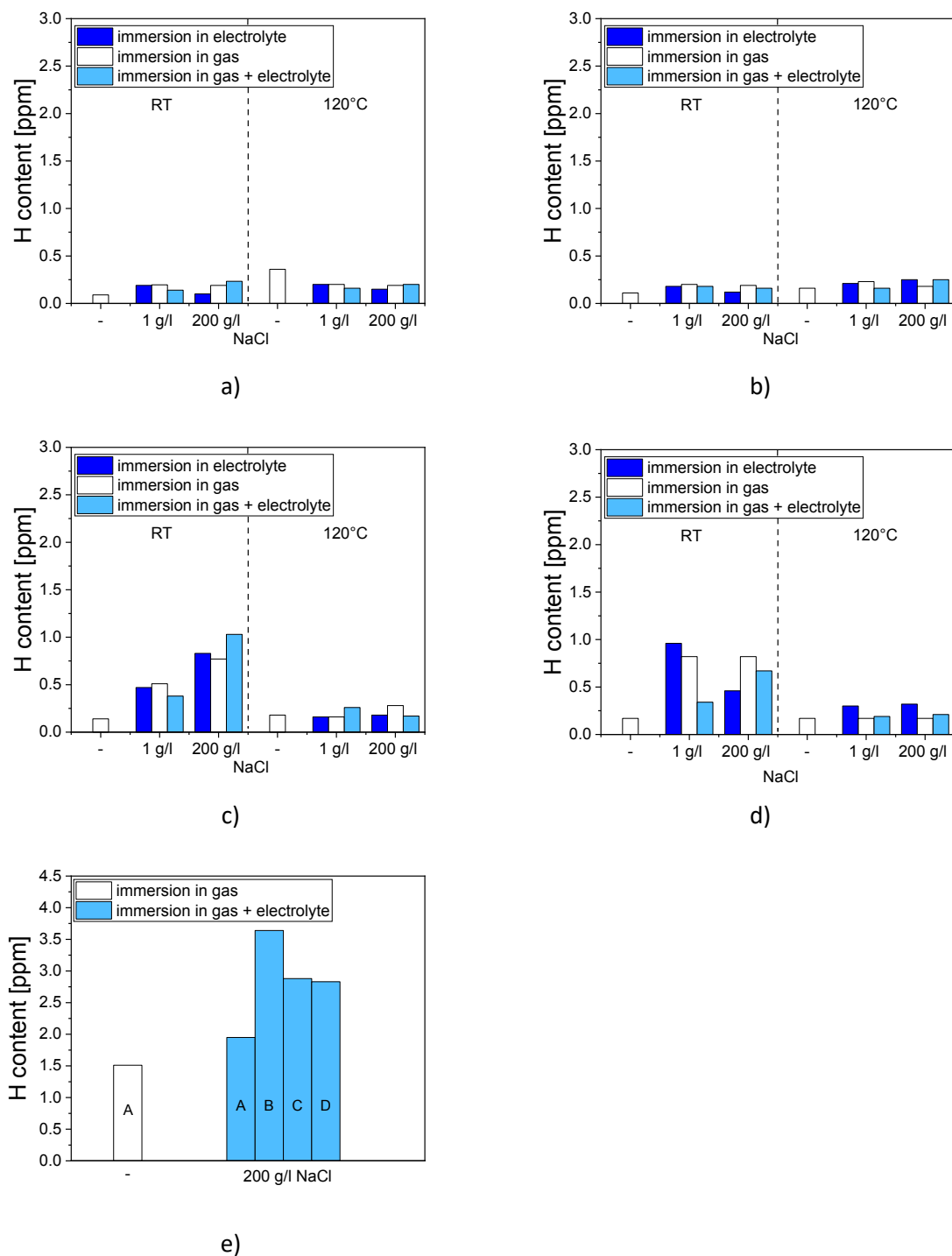
Figure 78: Hydrogen uptake after 30-day immersion of a steel L80 in different gases, electrolytes and salinity at different temperatures; a) gas A (120 bar H₂), b) gas B (120 bar H₂ + 15 bar CO₂), c) gas C (120 bar H₂ + 1 bar H₂S) and d) gas D (120 bar H₂ + 15 bar CO₂ + 1 bar H₂S); e) shows the pre-corroded steel L80 at room temperature in the dry condition with gas A, with an electrolyte of 200 g/l NaCl rotating in gas A, gas B, gas C and gas D

The results show some scatter. Even under H_2S-containing conditions, no significantly higher hydrogen uptake was achieved with the pre-corroded material.

The same effect like for steel K55 can be seen for steel L80 when H_2S is present. At 120 °C a faster formation of sulfide layer is observed and a decrease of hydrogen uptake compared to room temperature is obtained. For the experiments without H_2S, only an oxide respectively a hydroxide layer is formed in the experiments as can be seen in Figure 79 and Figure 80. Figure 81 and Figure 82 show results of SEM investigation on steel L80 in investigated gases with H_2S. In Figure 83 shows the steel L80 with a notch and pre-corroded specimens after 30 days exposure in gas D.

a)

b)

c)

d)
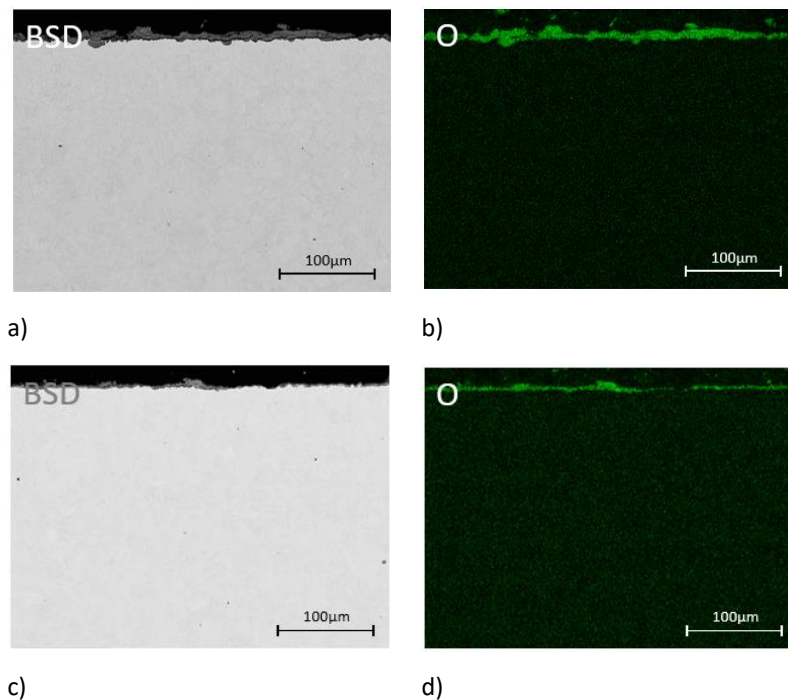
Figure 79: Steel L80 after 30 days alternating in exposure 200 g/l NaCl solution and gas A (120 bar H_2) a) BSD image at RT b) element mapping at RT; c) BSD image at 120 °C and d) element mapping at 120 °C
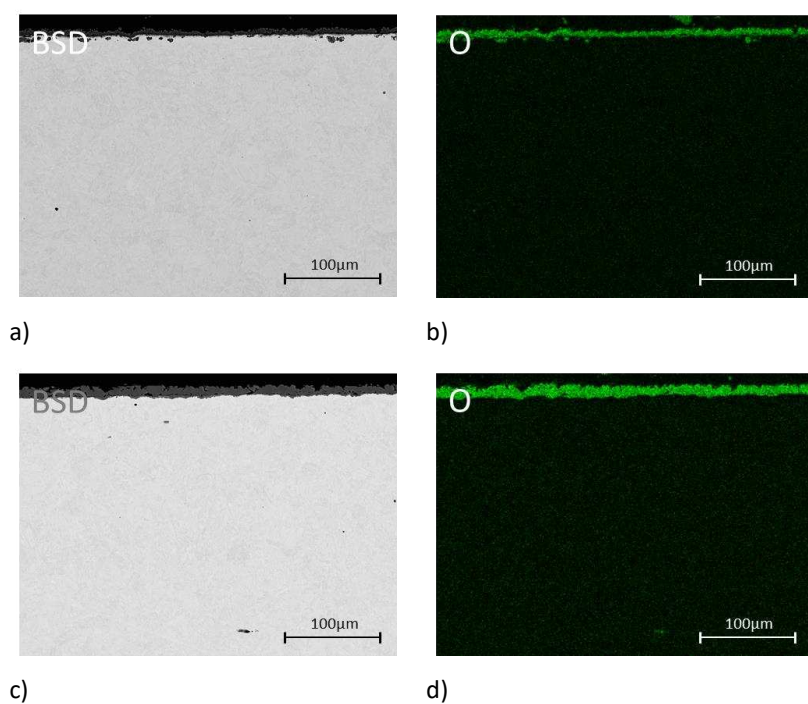
Figure 80: Steel L80 after 30 days alternating in exposure 200 g/l NaCl solution and gas B (120 bar H_2 + 15 bar CO_2) a) BSD image at RT b) element mapping at RT; c) BSD image at 120 °C and d) element mapping at 120 °C
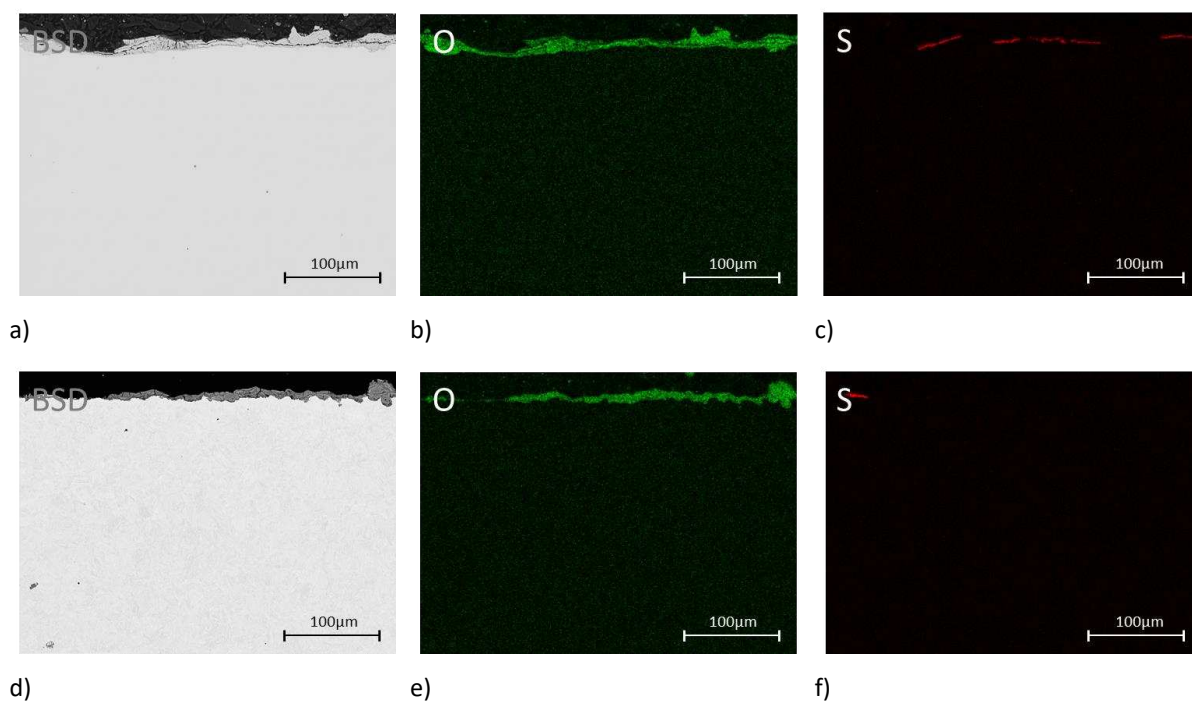
Figure 81: Steel L80 after 30 days alternating in exposure 200 g/l NaCl solution and gas C (120 bar H_2 + 1 bar H_2S) a) BSD image at RT b-c) element mapping at RT; d) BSD image at 120 °C and e-f) element mapping at 120 °C
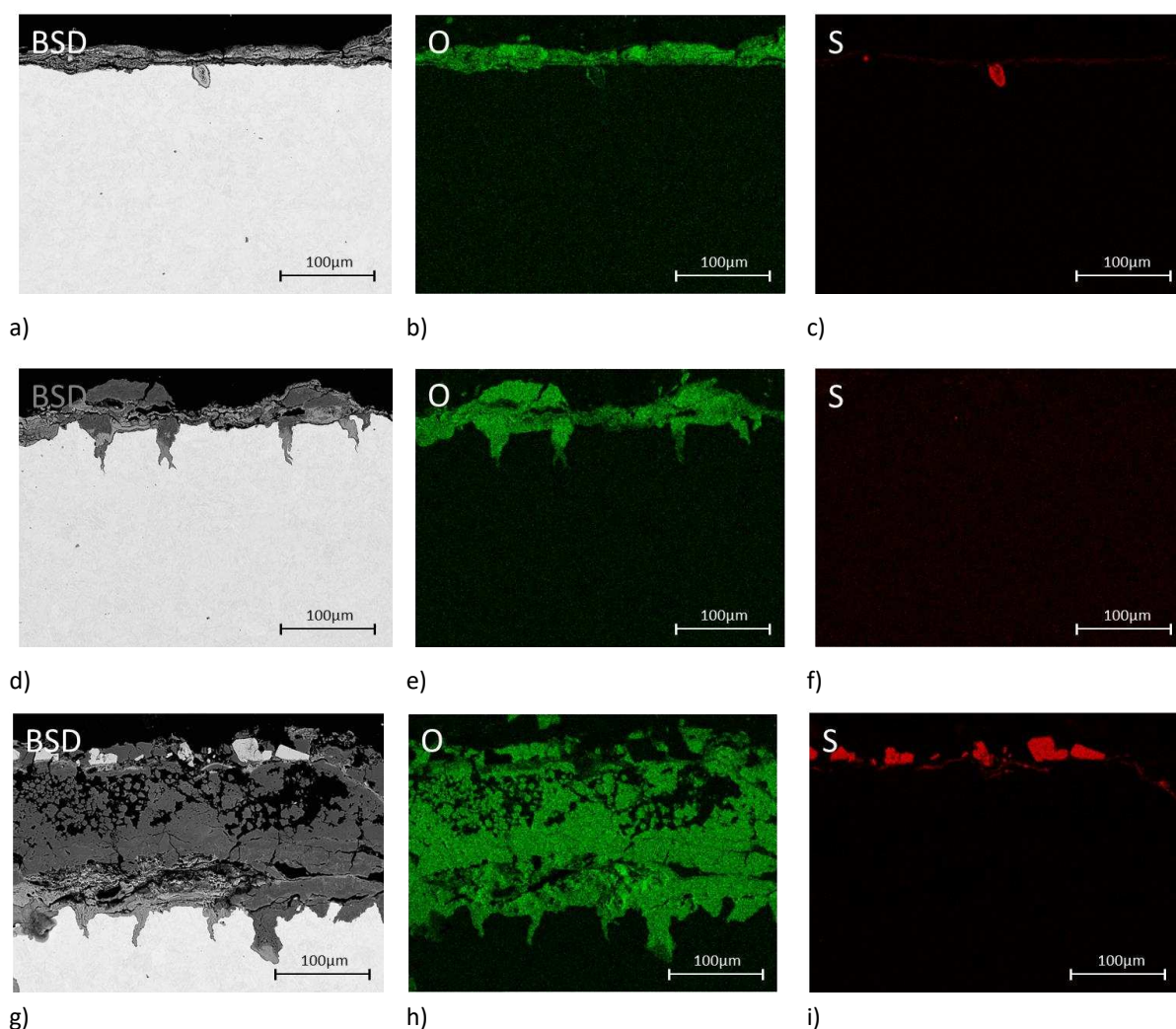
Figure 82: Steel L80 after 30 days alternating in exposure gas D (120 bar H₂ + 15 bar CO₂ + 1 bar H₂S) and 200 g/l NaCl solution a) BSD image at RT b-c) element mapping at RT; d) BSD image at 120 °C and e-f) element mapping at 120 °C, g-i) shows the same condition as d-f) at higher magnification at 1000x another position

In the tests with H₂S, an oxide and a sulfide layer were formed on the surface of the sample. Figure 81 a) still shows a reasonably homogeneous sulfide layer, other conditions with H₂S, lead to partial or not visible layers, as given in Figure 81 and Figure 82. Figure 82 d) shows a localized corrosive attack after immersion in gas D at 120 °C of up to 70 μm. A conclusion on the thickness of the layer at different temperatures cannot be made because of the high variation of the thickness, compare Figure 82 d) and g). Figure 82 d) shows a thinner layer with a maximum thickness of 50 μm, while Figure 82 g) shows a layer with 220 μm thickness. The thicker layer is more porous and the sulfide layer has not spalled off.
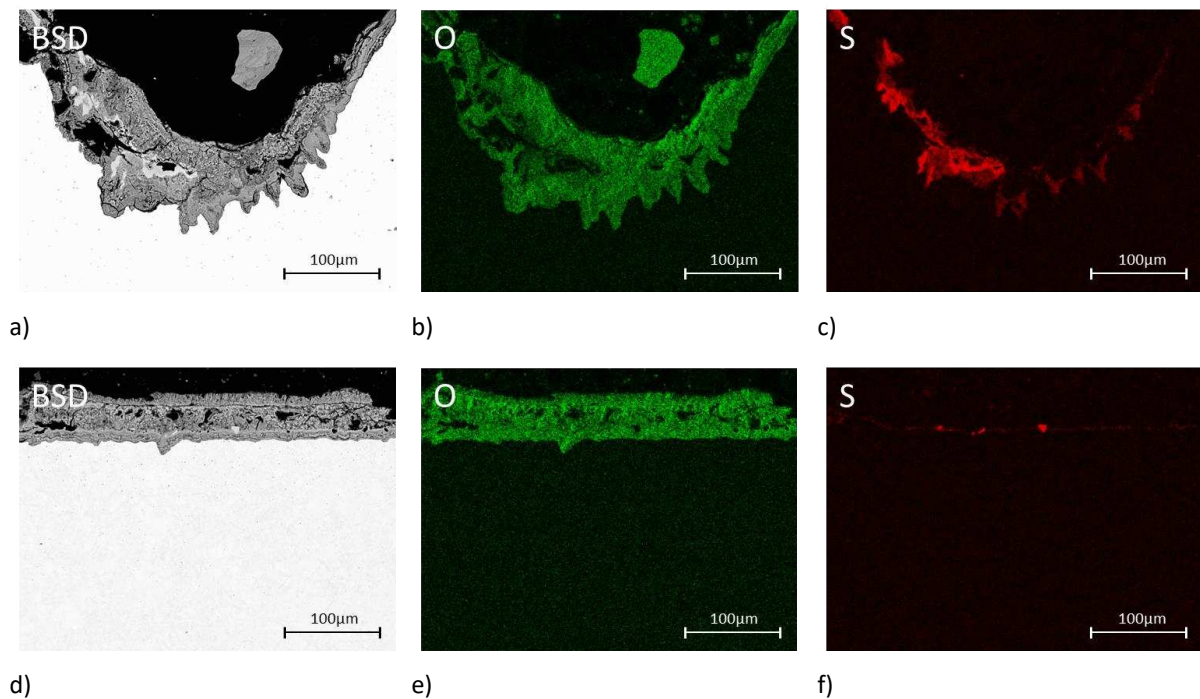
Figure 83: Steel L80 after 30 days alternating in exposure gas D (120 bar H₂ + 15 bar CO₂ + 1 bar H₂S) at RT a) BSD image at the notch and b-c) element mapping at the notch; d) BSD image at the pre-corroded sample, e-f) element mapping at the pre-corroded sample

When looking at the notched sample in Figure 83 a), one can see that the thickness of both layers is up to 100 µm and a localized corrosive attack of up to 30 µm is present. In comparison the sample with a pre-corroded layer has a maximum thickness of 75 µm and a localized corrosive attack of up to 15 µm. It is possible that deeper attacks can be found in other parts of the specimen.

In addition to the previous tests, hydrogen permeation tests were conducted. Figure 84 shows the results of the hydrogen permeation tests of steel L80. Figure 84 shows the two oxidation current as a function of time cycles that have been performed like for the other materials where permeation tests have been done.

The effective diffusion coefficient D_{eff} was $2.68 \cdot 10^{-6} \frac{cm^2}{s}$ for the first loading and $3.98 \cdot 10^{-6} \frac{cm^2}{s}$ for the second loading.
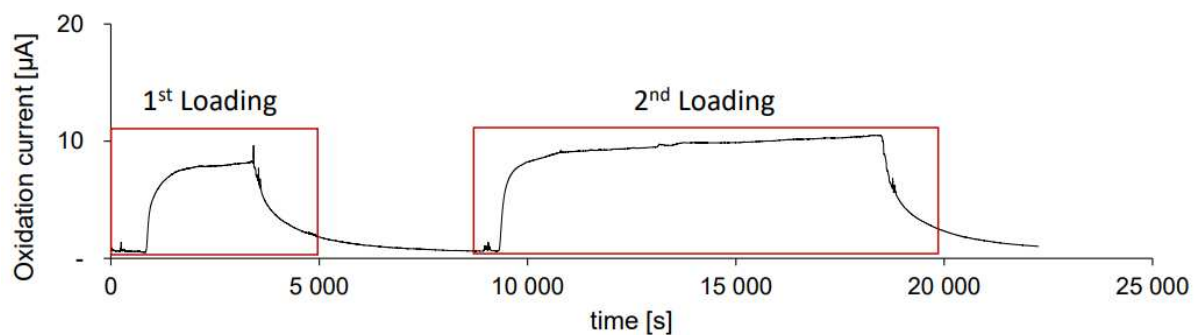
a)
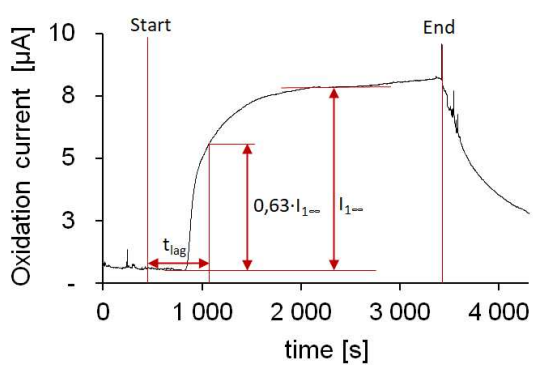
b)
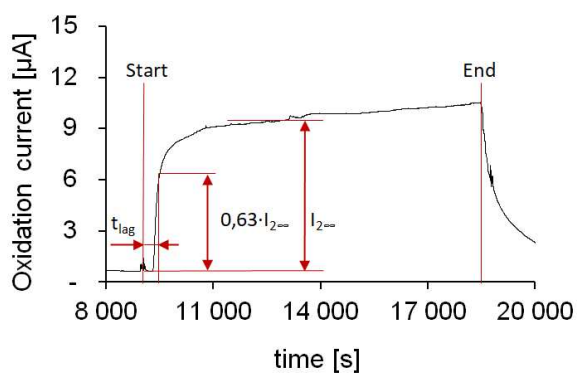
c)

Figure 84: Hydrogen permeation current as function of time for steel L80 a) Overview of two charging cycles; b) Detail of the first charging cycle; and c) Detail of the second charging cycle

4.3.2 Steel P110

Figure 85 presents the time to failure in a CLT of the tempered martensitic steel P110 for tested gas conditions. These conditions were dry hydrogen gas A (120 bar H_2), in gas A (120 bar H_2), in gas B (120 bar H_2 + 15 bar CO_2), in gas C (120 bar H_2 + 1 bar H_2S), in gas D (120 bar H_2 + 15 bar CO_2 + 1 bar H_2S) and with an electrolyte of 200 g/l NaCl in rotating autoclaves. There was no fracture under any of the tested conditions.
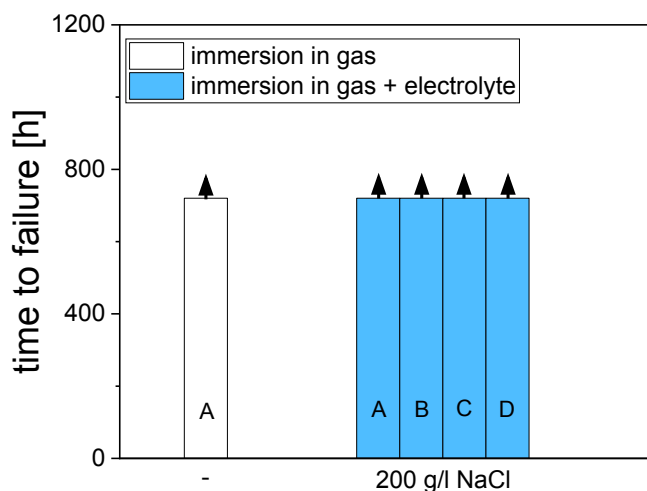
Figure 85: Time to failure in a CLT of tempered martensitic steel P110 at room temperature in gas A (120 bar H_2), gas B (120 bar H_2 + 15 bar CO_2), gas C (120 bar H_2 + 1 bar H_2S) and gas D (120 bar H_2 + 15 bar CO_2 + 1 bar H_2S) with an electrolyte 200 g/l NaCl rotating and one dry condition with gas A (120 bar H_2)

Figure 86 illustrates the hydrogen uptake at 25 °C in dry condition for gas A (120 bar H_2) and with an electrolyte of 200 g/l NaCl in gases A (120 bar H_2) to gas D (120 bar H_2 + 15 bar CO_2 + 1 bar H_2S). The lowest measured value was 0.09 ppm in dry gas A and the highest measured value was 1.65 ppm for gas D. The hydrogen content of the blank material was 0.23 ppm, which is slightly above the measured value with dry hydrogen, which indicates scatter of results. Under H_2S free conditions, there is almost no hydrogen uptake. The addition of H_2S increased the hydrogen uptake significantly.
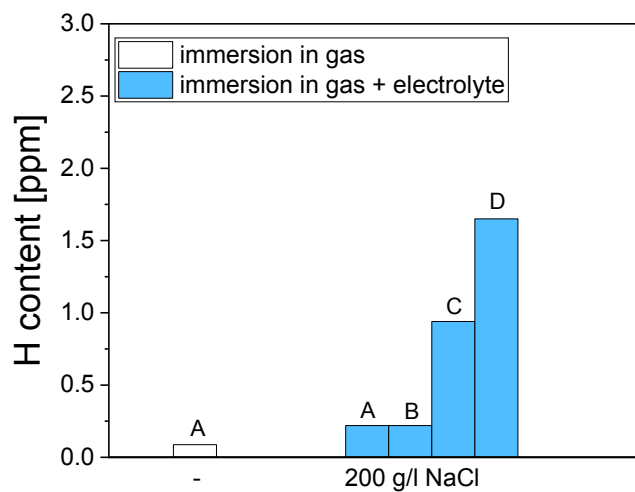
Figure 86: Hydrogen uptake of steel P110 in autoclave tests at room temperature in gas A (120 bar H₂), gas B (120 bar H₂ + 15 bar CO₂), gas C (120 bar H₂ + 1 bar H₂S) and gas D (120 bar H₂ + 15 bar CO₂ + 1 bar H₂S) with an electrolyte 200 g/l NaCl rotating and one dry condition with gas A (120 bar H₂)

Figure 87 shows the cross-section of tempered martensitic steel P110 after testing at room temperature with 200 g/l sodium chloride in gases A to gas D (120 bar H₂ + 15 bar CO₂ + 1 H₂S).

Testing in gas D yield to a significant localized corrosive attack with a maximum depth of up to 40 µm on the investigated surface area. Deeper attack can not be excluded. All other conditions (gas A, gas B and gas C) show no localized damage. They show uniform corrosion at the surface with layer formation.
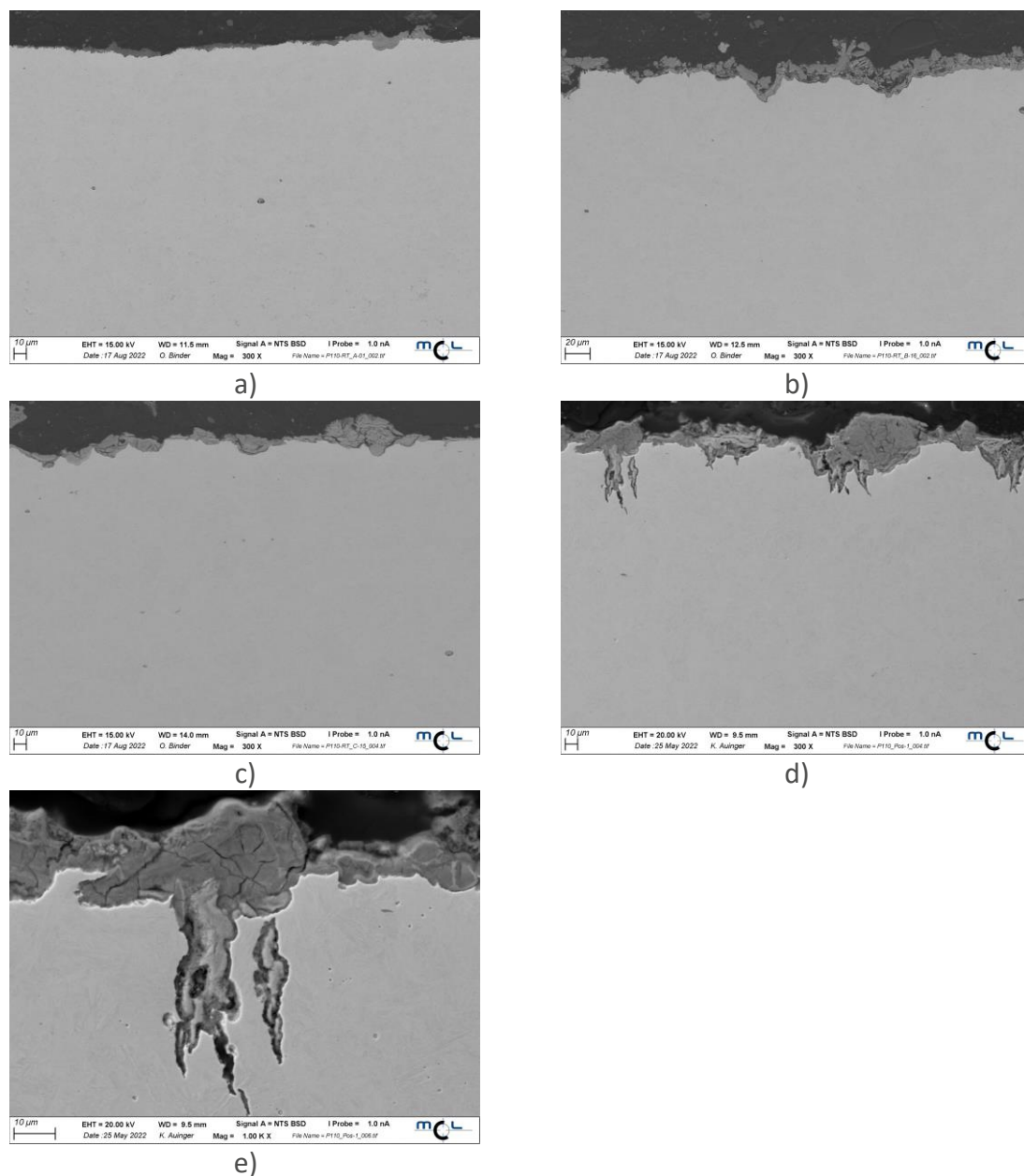
Figure 87: SEM analysis of the surface of the tempered martensitic steel P110 at 25 °C after autoclave testing with 200 g/l sodium chloride in gas A (120 bar H_2), b) gas B (120 bar H_2 + 15 bar CO_2), c) gas C (120 bar H_2 + 1 bar H_2S) and d) gas D (120 bar H_2 + 15 bar CO_2 + 1 H_2S) at magnification 300x; e) shows a detail of d) at higher magnification of 1000x

4.4 Corrosion Resistant Alloys

4.4.1 13 % Cr stainless steel

Figure 88 shows the time to failure in CLT of tempered martensitic 13% Cr-steel. Figure 88 illustrates the steel under the five tested conditions. No fracture under any of the tested conditions occurred.
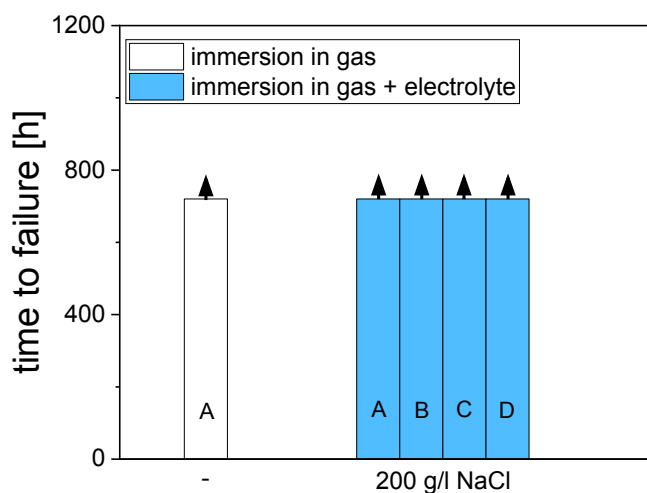
Figure 88: Time to failure of a tempered martensitic 13% Cr-steel at RT in gas A (120 bar H$_2$), gas B (120 bar H$_2$ + 15 bar CO$_2$), gas C (120 bar H$_2$ + 1 bar H$_2$S) and gas D (120 bar H$_2$ + 15 bar CO$_2$ + 1 bar H$_2$S) with an electrolyte 200 g/l NaCl rotating and one dry condition with gas A (120 bar H$_2$)

Figure 89 illustrates the hydrogen absorption under the applied test conditions. The lowest hydrogen value is 0.42 ppm after exposure H$_2$ atmosphere at 120 bar in dry condition and the highest value is 7.02 ppm when immersed in gas D and addition of an electrolyte. H$_2$S in the presence of an electrolyte resulted in highest hydrogen uptake.

When considering a fairly high hydrogen uptake for the passive 13 % chromium steel with a tempered martensitic microstructure, it is surprising that even under most aggressive conditions in Gas D no cracking did occur. Nevertheless one must not forget that the hardness level is rather low for the material representing a SMYS of 70 ksi (or 525 MPa of actual Yield Strength). The low mechanical properties (and the high ductility of the tempered martensite) are a result of the low carbon content of 0.19 % for this steel.
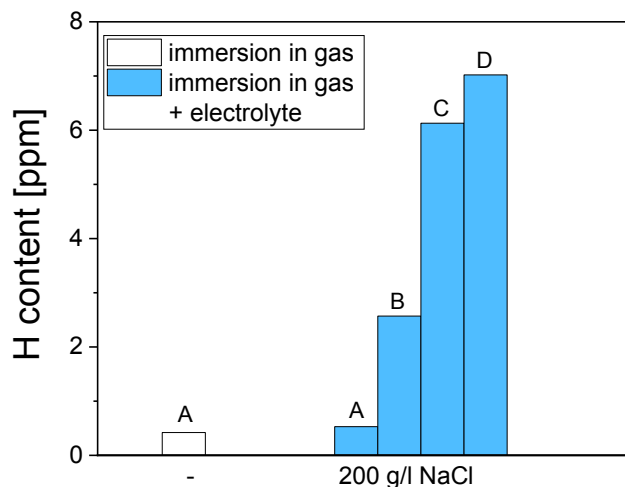
Figure 89: Hydrogen uptake of a tempered martensite 13% Cr-steel at RT in gas A (120 bar H$_2$), gas B (120 bar H$_2$ + 15 bar CO$_2$), gas C (120 bar H$_2$ + 1 bar H$_2$S) and gas D (120 bar H$_2$ + 15 bar CO$_2$ + 1 bar H$_2$S) with an electrolyte 200 g/l NaCl rotating and one dry condition with gas A (120 bar H$_2$)

Figure 90 shows a polished metallographic section at the surface of the 13 % Cr stainless steel after being tested at room temperature in Gas D (120 bar H$_2$ + 15 bar CO$_2$ + 1 bar H$_2$S) with a highly saline electrolyte.
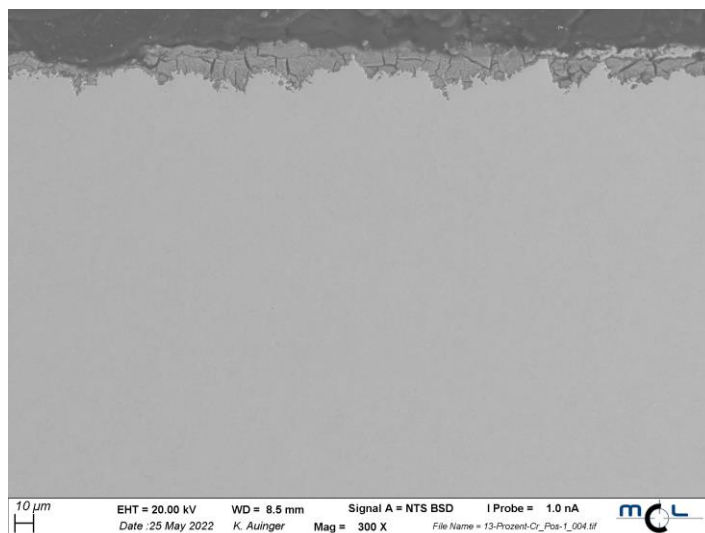
Figure 90: Cross section of a ferritic stainless steel 13% Cr at magnification of 300x, after testing in Gas D with 200 g/l NaCl at RT

The material shows pronounced uniform attack and a sulfide hydroxide layer at the surface. No localized attack occurred during testing.

4.4.2   Austenitic stainless steels 316L

Figure 91 depicts the time to failure of stainless steel 316L in CLT for both suppliers at room temperature in pure dry hydrogen gas condition at (120 bar H_2) and in four gases A to D with 200 g/l NaCl containing electrolyte. There was no fracture under any condition.
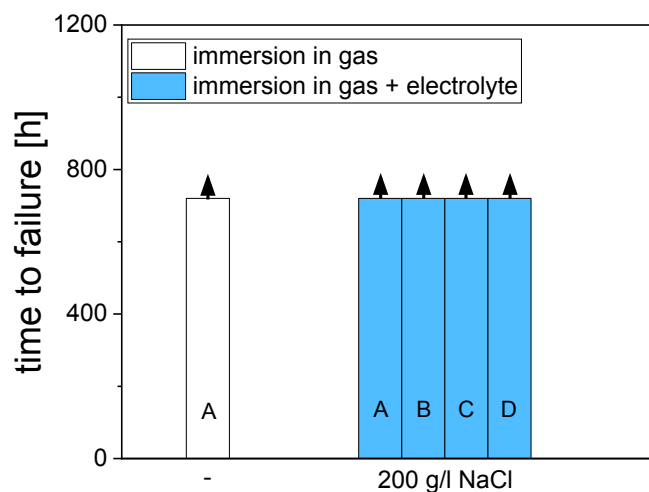
Figure 91: Time to failure of a stainless steel 316 L for both suppliers at RT in gas A (120 bar H_2), gas B (120 bar H_2 + 15 bar CO_2), gas C (120 bar H_2 + 1 bar H_2S) and gas D (120 bar H_2 + 15 bar CO_2 + 1 bar H_2S) with an electrolyte 200 g/l NaCl rotating and one dry condition with gas A (120 bar H_2); (no failure for both suppliers)

In Figure 92 hydrogen uptake of stainless steel from supplier no.1 is shown. The lowest value in autoclave tests of the stainless steel 316L from supplier 1 at room temperature was 1.70 ppm (in dry hydrogen) and the maximum value was 2.04 ppm after exposure to wet gas D. The blank hydrogen value of the stainless steel was 1.94 ppm. This is comparable with the value of the specimen that has been exposed to the dry 120 bar H_2 gas.
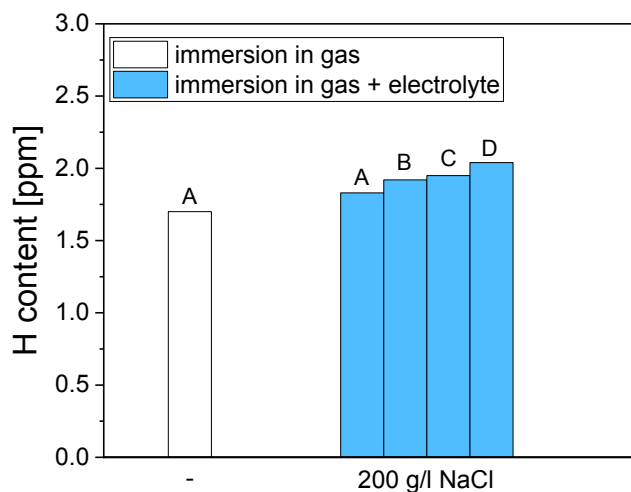
Figure 92: Hydrogen uptake of a stainless steel 316L from the supplier 1 at RT in gas A (120 bar H$_2$), gas B (120 bar H$_2$ + 15 bar CO$_2$), gas C (120 bar H$_2$ + 1 bar H$_2$S) and gas D (120 bar H$_2$ + 15 bar CO$_2$ + 1 bar H$_2$S) with an electrolyte 200 g/l NaCl rotating and one dry condition with gas A (120 bar H$_2$)

Figure 93 shows hydrogen uptake of 316L from supplier 2. Hydrogen content after exposure to dry hydrogen gas was 4.53 ppm, after immersion in gas C with a highly saline electrolyte. The blank value in the material is 3.20 ppm, which is 1.24 ppm higher than in 316L of supplier 1. Comparing the two Figures the initial hydrogen content determines all. The presence of an electrolyte leads to a slight increase of hydrogen uptake.
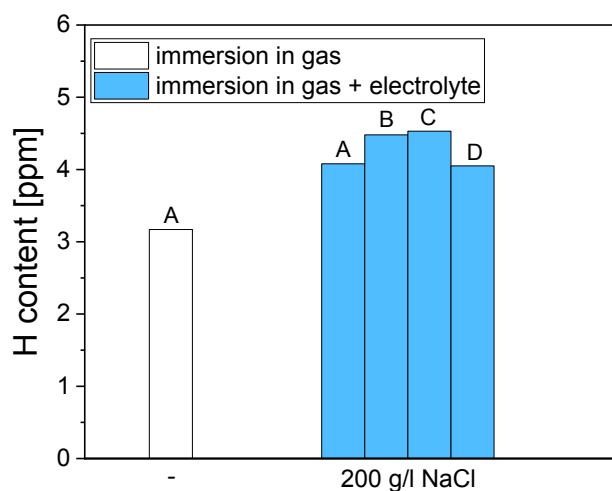
Figure 93: Hydrogen uptake of a stainless steel 316L from supplier 2 at RT in gas A (120 bar H$_2$), gas B (120 bar H$_2$ + 15 bar CO$_2$), gas C (120 bar H$_2$ + 1 bar H$_2$S) and gas D (120 bar H$_2$ + 15 bar CO$_2$ + 1 bar H$_2$S) with an electrolyte 200 g/l NaCl rotating and one dry condition with gas A (120 bar H$_2$)

In Figure 94 and Figure 95 the cross-sections of 316L stainless steels from both suppliers are given.
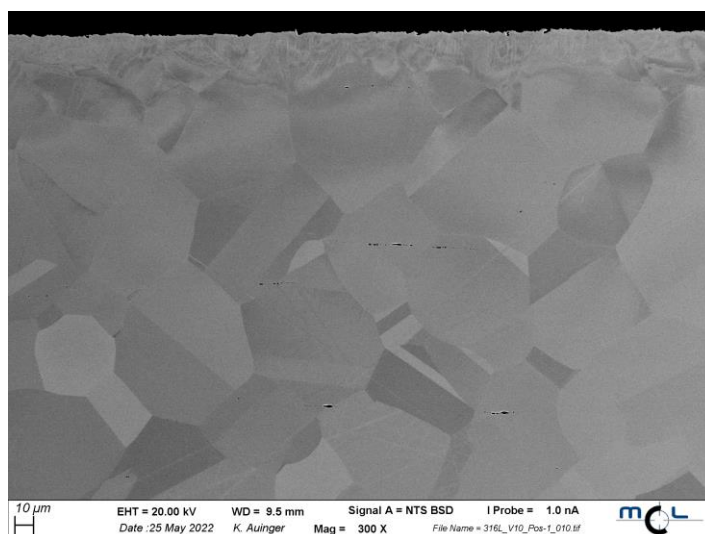
Figure 94: Cross section of stainless steel 316L from supplier 1 at magnification of 300x, in Gas D containing 200 g/l NaCl at RT
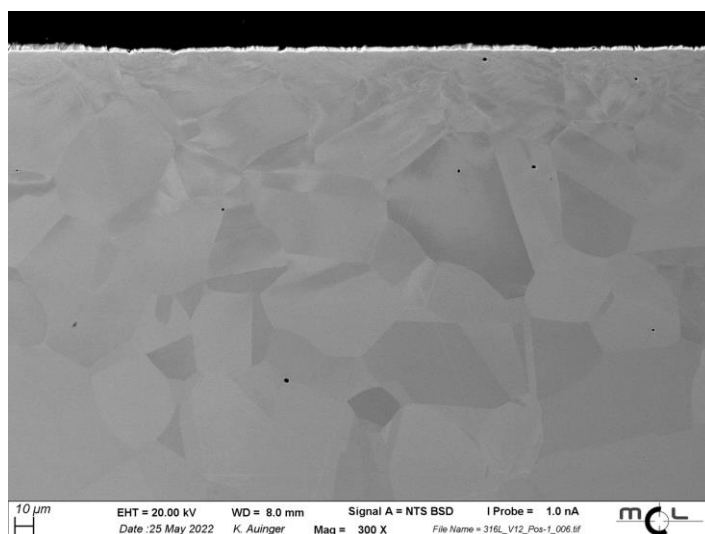
Figure 95: Cross section of stainless steel 316L from supplier 2 at magnification of 300x, in Gas D containing 200 g/l NaCl at RT

Under the tested conditions, the stainless steel 316L from both suppliers showed no corrosive attack on the surface.

4.4.3 Nickel-based Alloy 625

The time to failure of a weld-cladding Alloy 625 with a dendritic microstructure is depicted in Figure 96. Figure 96 depicts the time to failure at room temperature. There was no fracture under any tested condition.
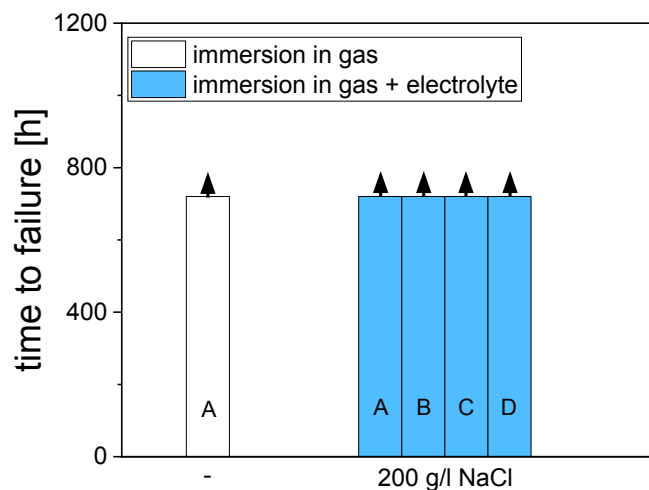
Figure 96: Time to failure of a dendritic welded Alloy 625 at RT in gas A (120 bar H₂), gas B (120 bar H₂ + 15 bar CO₂), gas C (120 bar H₂ + 1 bar H₂S) and gas D (120 bar H₂ + 15 bar CO₂ + 1 bar H₂S) with an electrolyte 200 g/l NaCl rotating and one dry condition with gas A (120 bar H₂)

Figure 97 represents hydrogen uptake after CLT. The lowest value for weld-cladded Alloy 625 at room temperature is 1.13 ppm when dry hydrogen is present, and the highest value is 6.86 ppm, when the specimen was immersed in gas D with electrolyte of a high salinity. Blank value was 0.78 ppm, which is lower than the dry condition. When H_2S and an electrolyte were present, the hydrogen uptake increased substantially.
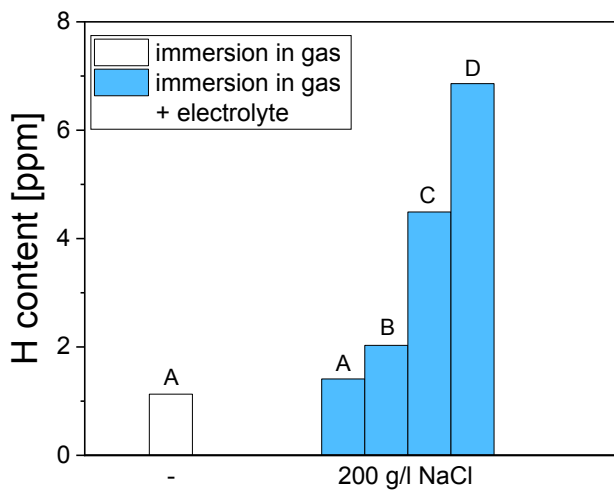
Figure 97: Hydrogen uptake of a dendritic welded Alloy 625 at RT in gas A (120 bar H_2), gas B (120 bar H_2 + 15 bar CO_2), gas C (120 bar H_2 + 1 bar H_2S) and gas D (120 bar H_2 + 15 bar CO_2 + 1 bar H_2S) with an electrolyte 200 g/l NaCl rotating and one dry condition with gas A (120 bar H_2)

Figure 98 shows no surface attack of Alloy 625.
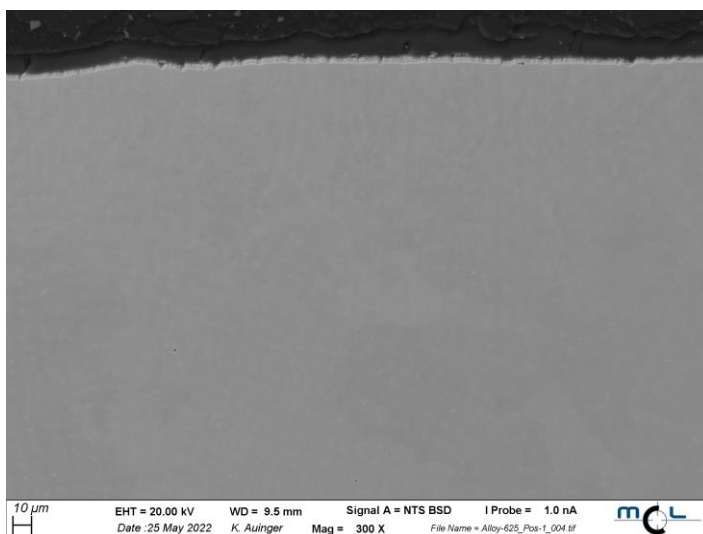
Figure 98: Cross section of a dendritic welded Alloy 625 at magnification of 300x, in Gas D containing 200 g/l NaCl at RT

The cross-section of Alloy 625 also shows that there is no localized corrosive attack on the surface.

4.4.4   Duplex stainless steel 2205

Figure 99 shows the time to failure of Duplex stainless steel 2205 in CLT. A fracture occurred during exposure to gas D with electrolyte.
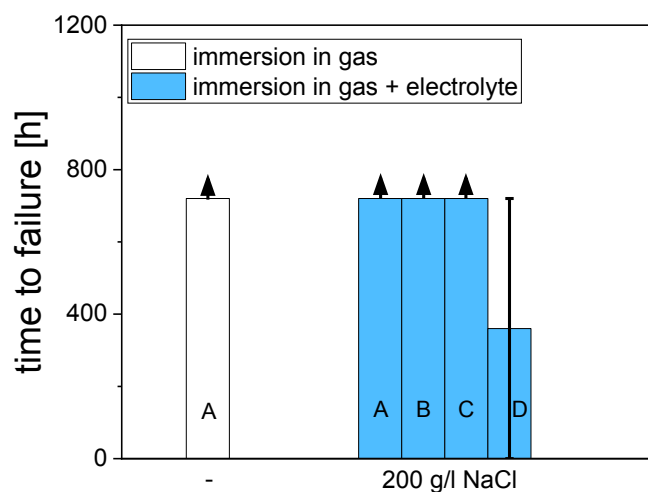
Figure 99: Time to failure of Duplex stainless steel 2205 at room temperature in gas A (120 bar H$_2$), gas B (120 bar H$_2$ + 15 bar CO$_2$), gas C (120 bar H$_2$ + 1 bar H$_2$S) and gas D (120 bar H$_2$ + 15 bar CO$_2$ + 1 bar H$_2$S) with an electrolyte 200 g/l NaCl rotating and one dry condition with gas A (120 bar H$_2$)

Figure 100 shows the hydrogen uptake of Duplex stainless steel. The lowest hydrogen uptake was 4.08 ppm exposure to dry hydrogen gas and the highest value was 7.02 ppm after exposure to mixed H$_2$/CO$_2$/H$_2$S gas in the presence of an electrolyte. The blank hydrogen value was 4.72 ppm, which is slightly higher than the hydrogen content measured after exposure to dry pressurized hydrogen, which may be due to a scatter of results There is a certain hydrogen uptake in the presence of an electrolyte. Finally cracking occurred near 7 ppm hydrogen.

In the Figure 101, the fracture surface of Duplex stainless steel 2205 tested under most severe conditions including the H$_2$/ CO$_2$/ H$_2$S gas is shown. The fracture surface has been investigated with a scanning electron microscope and recorded with a secondary electron detector, for topographical imaging. At the 12 o'clock position, the initiation point of fracture can be seen. The upper area is a brittle hydrogen fracture, details are shown in the green frames. The ductile area is visible at the bottom of the fracture surface, details can be seen in the blue frames. The transition area between the zones is shown in the brown frame.

Figure 102 illustrates in details the different fracture zones of the duplex steel in SEM images. The fracture surface of a hydrogen crack can be divided into three parts. In Figure 102 a) to d), a hydrogen fracture with river

patterns can be seen in the green frame. Figure 102 e) shows the transition zone from brittle to ductile (brown frame). Between 4 and 8 o'clock position there is a ductile fracture with coarse dimples. Figure 102 f) shows the ductile fracture surface with the blue frame.
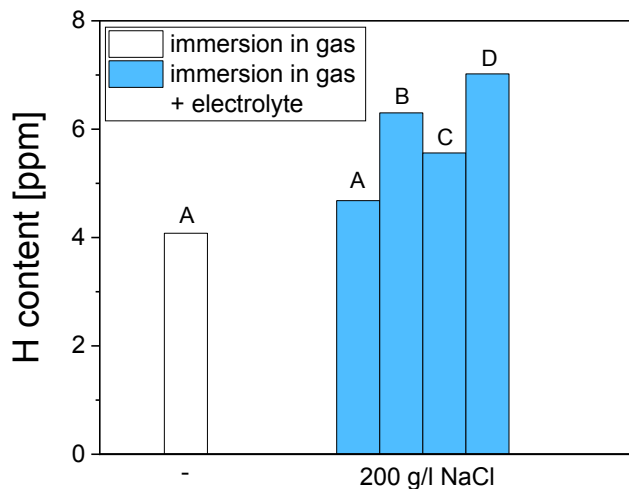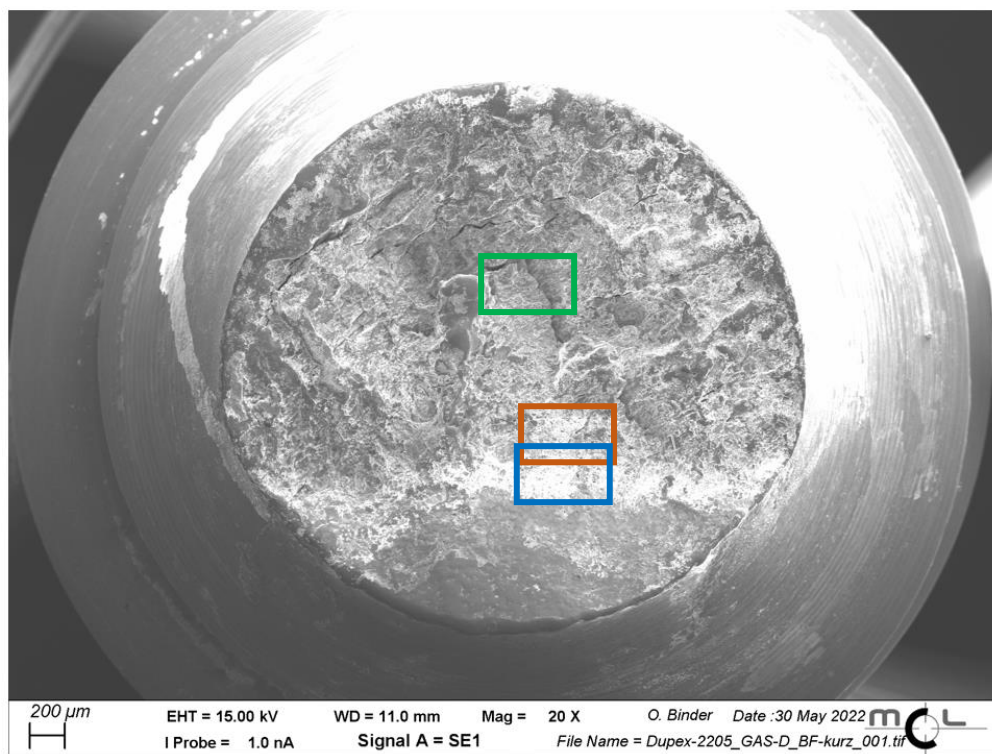

Figure 100: Hydrogen uptake of a Duplex stainless steel 2205 at room temperature in gas A (120 bar H$_2$), gas B (120 bar H$_2$ + 15 bar CO$_2$), gas C (120 bar H$_2$ + 1 bar H$_2$S) and gas D (120 bar H$_2$ + 15 bar CO$_2$ + 1 bar H$_2$S) with an electrolyte 200 g/l NaCl rotating and one dry condition with gas A (120 bar H$_2$)

Figure 101: Electron optical images of the fracture surface of a Duplex 2205 at room temperature, in a rotating autoclave with 200 g/l NaCl in gas D
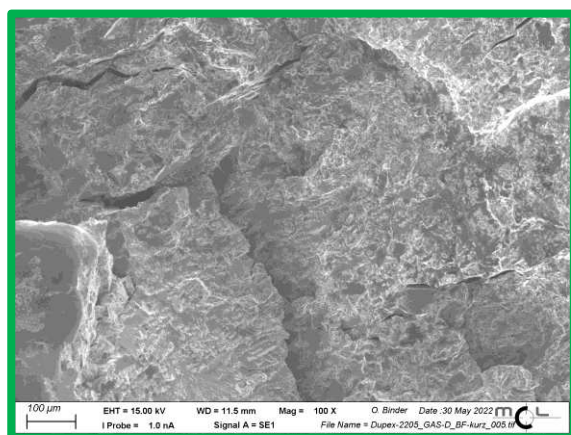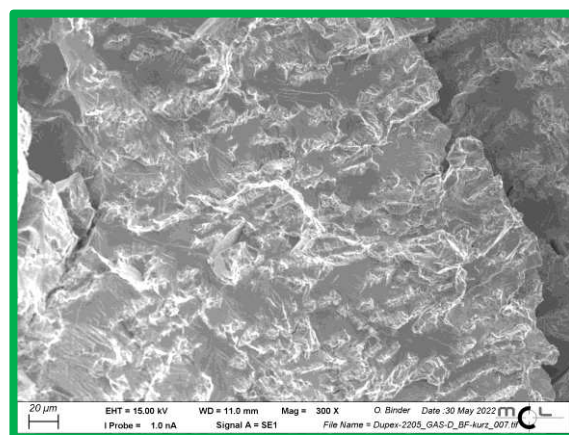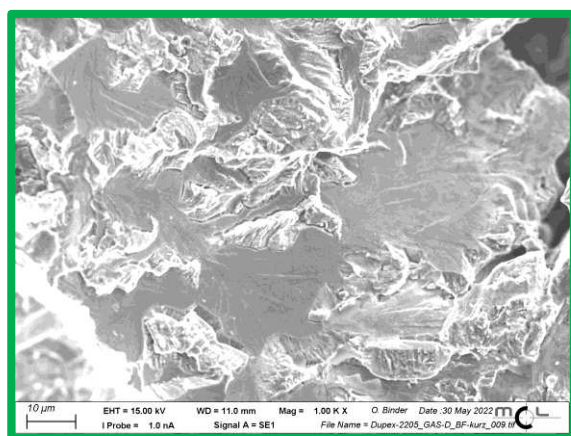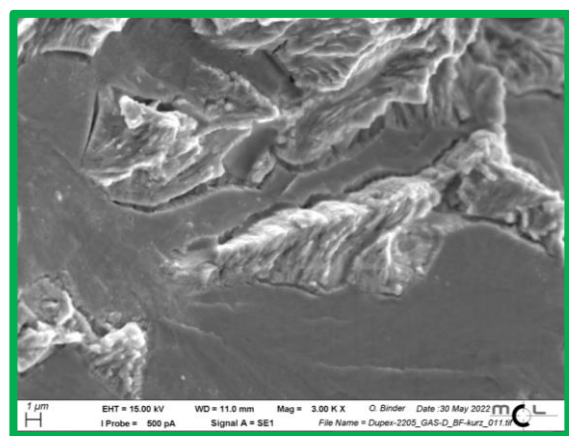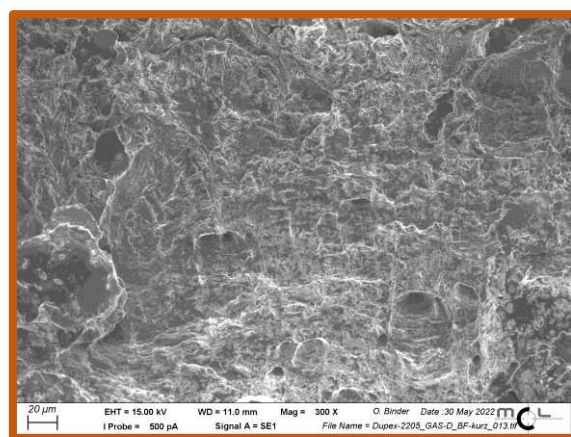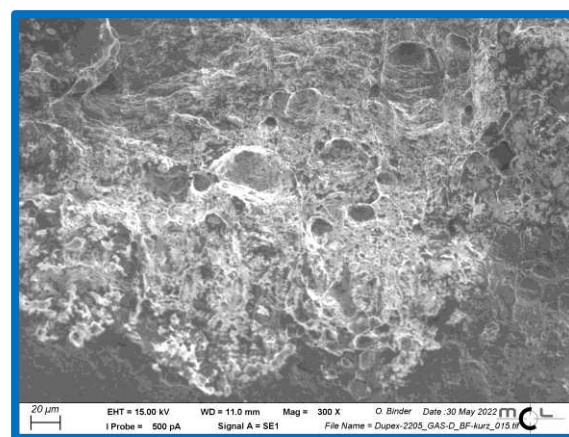
Figure 102: Details of the fracture surface of Duplex steel 2205 in a) to d) brittle fracture area, e) showing the transition area from brittle to ductile zones and f) showing the ductile fractured area

5 Discussion

In order to investigate the hydrogen resistance of the materials, permeation tests were carried out. For this purpose, the effective diffusion coefficient was determined by measuring the oxidation current over time, what provides information about the trapping behaviour of the material.

Retained austenite, represents a fcc crystallographic structure, that can affect the hydrogen cracking resistance of a steel substantially, due to its low diffusion, which allows it to act as a deep hydrogen trap. Commonly, the steel which has this phase have lower D_{eff} and higher solubility due to its close-packed lattice. On the contrary, the ferritic phase, which has a bcc crystal structure, shows a high diffusion rate and a low solubility as a result of its open lattice structure. The martensite, with a bct crystal structure, is more tightly packed than bcc, and the hydrogen D_{eff} value is between that of ferrite and austenite [62,156].

The normalized permeation transients resulting from the first and second loading of the electrochemical permeation experiments are shown in Figure 103. Three ferritic pearlitic materials, whereby two of them were in welded (J55 and K55) and one in its base (K55) condition, as well as one tempered martensite (L80) were investigated. The effective diffusion coefficients D_{eff} determined lie in the range of $6.5 \cdot 10^{-7} \frac{cm^2}{s}$ to $8.0 \cdot 10^{-6} \frac{cm^2}{s}$ for the materials investigated, see Table 10. As shown in Figure 100, the hydrogen traps increase from ferritic pearlitic steel K55, to tempered martensite L80, welded J55 and further to welded K55. What is additionally visible from the normalized permeation current versus time is that the second loading for all investigated materials are slightly faster than the first loadings, with the exception of welded steel K55, where the two loadings are very similar.
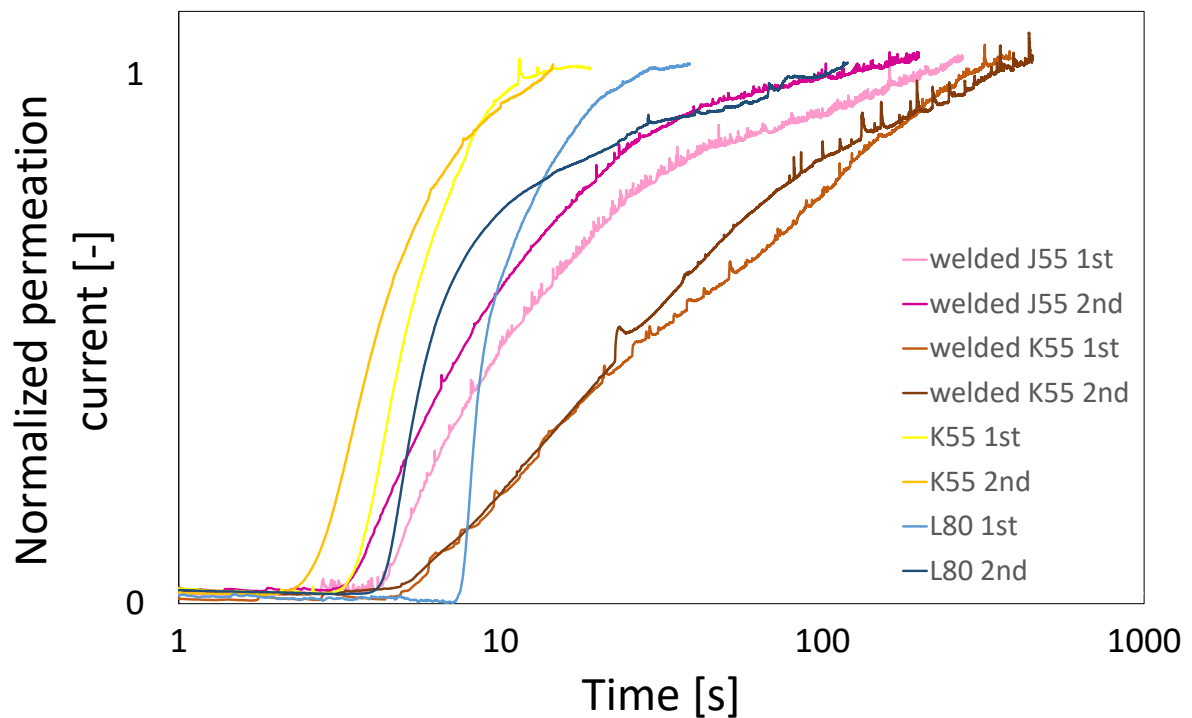
Figure 103: Normalized permeation transients of the first and second loading of four carbon steel grades

Figure 104 shows an overview of comparison of several data points of the measured D_{eff} of the first and second loading. Additionally, pure iron is plotted in the Figure 104 to show the effect of hydrogen trapping. In Table 10 results of the measured D_{eff} are presented.

Since the second loading is slightly faster compared to first for steel K55, there are some deep traps, present. As expected from the literature review, the results show diffusion coefficients for non-sour gas resistant steels. The steel L80 has more traps because it has a different chemical composition and is differently heat treated than the ferritic-pearlitic steel K55. The steel L80 has more traps due to the fact that this steel is also more deformed, in the manufacturing process. Heat treatment, resulted in martensitic transformation, which distorts the lattice and causes an increase in stress. From the lower diffusion coefficients of steel L80, it can be concluded, that in L80 more traps are present compared to steel K55.

Diffusion coefficient of welded steel J55, are in correspondence with those found in literature. The welded ferritic-pearlitic steel J55 has more traps than the ferritic-pearlitic steel K55 which is also more deformed by the welding process, which also has a heat treatment effect on the material. As a result, the diffusion coefficients of the welded material are lower. The welded steel K55 has more traps than the unwelded ferritic-pearlitic steel

due to being more deformed. The welded steel K55 has the highest trap density of all the investigated materials. As a result, the diffusion coefficients are lower [72,75,157].
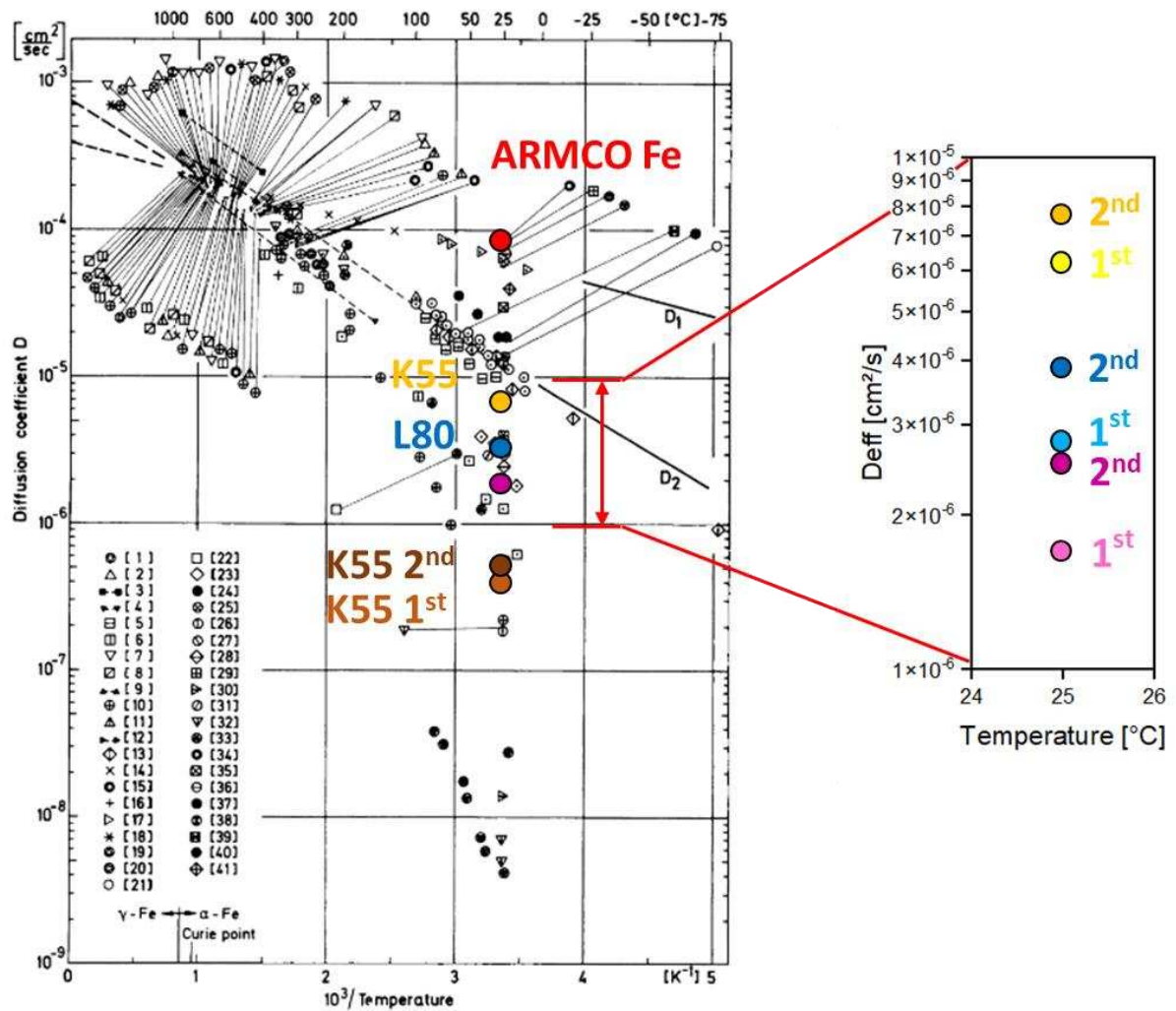

Figure 104: Plotting the measured values in the effective diffusion coefficient versus temperature [70]

Table 10: Results of electrochemical permeation experiments

Material	D_{eff} [cm²/s]
K55 1st loading	$6.22 \cdot 10^{-6}$
K55 2nd loading	$7.96 \cdot 10^{-6}$
L80 1st loading	$2.68 \cdot 10^{-6}$
L80 2nd loading	$3.98 \cdot 10^{-6}$
J55 welded 1st	$1.69 \cdot 10^{-6}$
J55 welded 2nd	$2.36 \cdot 10^{-6}$
K55 welded 1st	$4.57 \cdot 10^{-7}$
K55 welded 2nd	$6.50 \cdot 10^{-7}$

Additionally to permeation tests, autoclave tests were carried out. Hydrogen content was measured after 30 days of exposure by the use of a TDS. Cross-sections were investigated in a SEM to characterize the depth of localized corrosive attack. With this informations, it was possible to identify application limits for the investigated materials. A summary of these results is shown in Table 11. Table 11 also includes a color code for the depth of localized corrosion attack and for cracking. Green represents a localized attack that causes little or no harm (low or no danger of HE), whereas red and orange represent a localized attack that causes cracking or failure (either by ongoing localized corrosion or by HE). The most severe localized corrosive attack was observed in gas D, which contained H_2 as well as H_2S and CO_2.

The German Technical and Scientific Association for Gas and Water (Deutscher Verein des Gas- und Wasserfaches: DVGW), together with the University of Stuttgart, investigated how susceptible the German gas pipelines are to HE. In their investigations, samples were exposed to different loads in a hydrogen atmosphere of 100 bar. There was not found any issue with hydrogen embrittlement. The authors state that only individual plant components or some specific parts of the existing equipment might have to be replaced. It is now the federal government's turn to support this great potential and pave the way for the hydrogen economy, to an accelerated climate protection. These results correspond to the present research work for applications with dry and pure hydrogen. However, additional changes such as micro-organisms can lead to changes in the applicability limit, see the following paragraph [158].

Table 11: Summary of the autoclave results of the localized corrosive attacks for all investigated materials

Material	max H-uptake / blank value	Depth of localized corrosion attack*	cracking (no/yes)
20MnV5	2.71 / 0.11	≤ 10 μm	no
welded J55	2.95 / 0.65	≤ 10 μm	no
welded J55 pre-corroded	3.32 / 0.65	≤ 5 μm	no
welded J55 with notch	-	≤ 10 μm	no
K55	2.33 / 0.22	15 μm	no
K55 pre-corroded	3.64 / 0.22	≤ 5 μm	no
K55 notched	-	30 μm	no
welded K55	2.69 / 0.49	≤ 5 μm	no
L80	1.03 / 0.21	70 μm	no
L80 pre-corroded	3.55 / 0.21	15 μm	no
L80 notched	-	30 μm	no
P110	1.65 / 0.23	40 μm	no
quenched material	0.86 / 0.20	fracture	yes, presence of H_2
13%Cr	7.02 / 0.52	≤ 5 μm	no
316L IGS	2.04 / 1.94	no attack	no
316L Vallourec	4.53 / 3.20	no attack	no
Duplex 2205	7.02 / 4.72	fracture	yes, presence of H_2S
Alloy 625	6.86 / 0.78	no attack	no

increasing yield strength

increasing alloy content

* low...≤ 10 μm/mt   * medium...10 – 30 μm/mt   * high...≥ 30 μm/mt

Low strength carbon steels:

H_2S dissolved in an artificial brine results in an increased hydrogen uptake as mentioned already before. The cross-section of steel 20MnV5 shows in the SEM analysis that there are no cracks on the surface. The material is resistant under the tested conditions and is suitable for hydrogen applications without restrictions (except the maximal applied partial pressures).

H_2S free gases caused almost no hydrogen uptake in the welded steel J55 compared to the blank value (valid for room temperature). Higher hydrogen uptake is indicated at 120 °C under same gaseous conditions. Measurements with gases with attentional H_2S show a significant increase in hydrogen uptake for both, ambient temperature and elevated temperature. Due to the decreasing pH value by dissolving H_2S into an electrolyte, gases containing H_2S are more severe than gases without H_2S which yields in higher absorbed hydrogen contents. The hydrogen uptake is even lower when the addition of H_2S to the gas resulted in a faster sulfide layer formation at 120°C. As a result, a reduction in the hydrogen uptake due to the layer that acts as a barrier was obtained when compared to room temperature tests, where the sulfide layer formed at much lower rates. Although the maximum value of 22 HRC from the standard was exceeded by more than twice the limit value in the heat-affected zone, no irregularities occurred. The welded steel J55 is resistant under the test conditions and appears to be suitable for hydrogen applications for underground hydrogen storage [32,159].

For the steel K55 the addition of H_2S to the gas, resulted in a faster sulfide layer formation at 120 °C compared to the tests carried out at 25 °C. As a result, the uptake of hydrogen content decreased. Altogether it can be determined that the welded ferritic pearlitic steel J55 has a higher hydrogen uptake than the unwelded ferritic pearlitic steel K55. The heat treatment by welding can be achieved by changing the stress concentrations, can be responsible for this. It was found that the hydrogen uptake of the pre-corroded steel K55 are similar to the welded and pre-corroded steel J55. The steel K55 is resistant under the test conditions, when localized corrosive attack is not an issue and appears to be suitable for hydrogen applications for underground hydrogen storage, this is also mentioned in the norm ISO 15156-1:2020 [159].

The welded material K55 has a higher hydrogen uptake than the not welded K55. The cross-sections shows that there is no local attack starting from the surface. Although the hardness value in the heat-affected zone exceeded the H2S applicability limit of 22 HRC, no cracking occurred. Therefore the welded steel is not susceptible to HE in gas storage. As a consequence, it can be used for hydrogen applications [32].

Higher strength carbon steels:

In the case of hydrogen, it is well-documented that the fracture elongation decreases with increasing tensile strength of the material. Carbon steels which perform well in hydrogen service over long periods of time are generally low strength alloys with a Specified Minimum Yield Strength (SMYS) < 52 ksi, which is equivalent to 359 MPa. The actual YS is usually higher than the SMYS, but particular attention must be given to higher strength materials that exceed this limit [32,160]. When a steel has higher mechanical properties, especially Yield Strength, which is the design measure in construction and also in oil and gas industry, higher stresses are applied in service and consequently a higher hydrogen concentration at the crack tip can occur. On the contrary the increase in yield strength does not affect the amount of absorbed hydrogen in deep traps, since saturation is independent of yield strength [84]. According to Sieverts and Krumbhaar [44], a higher hydrogen pressure leads to a greater amount of absorbed hydrogen in the material, see the following paragraph. The design guidelines for hydrogen pipes and pipelines indicate that martensitic materials, when used, should be heat treated to engineer the strengths at the lower end of the specification scale [32,161].

In the autoclave tests steel L80 at room temperature had a very low hydrogen uptake when no H_2S was present. When H_2S is present, there is a certain hydrogen uptake at room temperature, which increases significantly in the presence of an electrolyte. This is due to the lowering of the pH of the solution by H_2S dissolution. The same was found for the K55 steel. On the contrary, the addition of H_2S leads at 120°C to a kinetically favoured formation of a sulfide layer and the result is a reduced quantity of absorbed hydrogen compared to tests carried out at room temperature. L80 is stable under the test conditions as long as localized corrosive attack is not an issue, which only occurs when H_2S is present and appears to be suitable for hydrogen applications for underground hydrogen storage, with some limitation when H_2S is present. Since also ISO 15156-1:2020 and ISO 15156-3:2020 indicates that steel L80 is a sour gas resistant steel grade, it can be used at all temperatures, even when H_2S is present as long as localized corrosion is not an issue [159,162].

The tempered martensitic steel P110 has the same order of magnitude of hydrogen uptake like the tempered martensitic steel L80 with a lower strength. In H_2S significant localized corrosive attack with a maximum depth of 40 μm was obtained. Therefore, the material P110 can only be used to a limited extent in the presence of H_2S. According to ISO 15156-1:2020 [159] and ISO 15156-3:2020 [162], the steel P110 should only be used for H_2S applications at temperatures higher than 80°C. Consequently, at room temperature, it should not be considered for sour service application. The steel P110 is much more susceptible to hydrogen embrittlement than the quenched and tempered martensitic steel L80 with lower tensile strength.

CRAs:

Austenitic stainless steels do not lose a high amount of their high ductility (or reduction of area) when being exposed to dry hydrogen gas. In terms of resistance to hydrogen embrittlement, these materials appear to be the best choice for hydrogen piping systems [32]. Austenitic stainless steel with high nickel equivalent is more resistant to HE. The nickel-based alloys have excellent mechanical properties and corrosion resistance and are therefore often used in hydrogen energy systems [163]. Nevertheless, austenitic stainless steel is not suitable for long-distance hydrogen transport due to its low strength and high cost. Most pipelines are installed in underground locations, so for large-scale hydrogen transport over long distances, pipeline steels are considered to be the most environmentally friendly and economic material [164].

No localized corrosion damage has occurred. It is therefore apparent that the 13% chromium steel can be used without restrictions for hydrogen storage. Although the standards ISO 15156-1:2020 and ISO 15156-3:2020 [159,162] specifies a limitation for H_2S concentration, 13 % Cr steel did not show any indications for HE in the presence of H_2S.

Stainless steels 316L (two suppliers) showed no cracking at all in all investigated conditions. The amount of hydrogen uptake of the second supplier is double of the one of 316L of supplier 1. This is due to the significantly lower grain size of the second supplier of 316L material. During the test, both stainless steels 316L showed no corrosive attack on the surface. According to the standards ISO 15156-1:2020 and ISO 15156-3:2020 [159,162], steels 316L can be used for H_2S applications if the partial pressure is less than 10.2 kPa. In the present tests the material was investigated at 1 bar of H_2S, which corresponds to 100 kPa H_2S, which is outside of the application limits of this steel. There is no corrosive attack on the surface of both specimens. Under the tested conditions, the stainless steel from both suppliers is not susceptible to hydrogen embrittlement. The tested stainless steels are well applicable for use in hydrogen atmospheres. From the design guidelines for hydrogen pipes and pipelines [32] it was suggested that 316L austenitic steel is highly suitable choice for the use of high pressure dry hydrogen gas.

When an electrolyte and gases with H_2S are present, the hydrogen uptake of Alloy 625 in gases C and D are increased. This is due to the fact that H_2S lowers the pH of the solution. In autoclave tests performed without H_2S, hydrogen uptake is low to moderate. High hydrogen contents in the steel are induced by conditions containing H_2S. The cross-section of Alloy 625 shows no localized corrosive attack on the surface. Under the tested conditions, the material appears to be highly resistant and suitable for hydrogen applications. It can be used in a H_2S environment at any temperature and partial pressure according to the standards ISO 15156 [159,162].

Duplex stainless steel 2205, which has a mixed austenitic and ferritic structure, is very susceptible to hydrogen embrittlement. The microstructure of duplex steels influences their behavior in terms of HE due to the fraction on the one hand of ferrite with a fast diffusion and a low hydrogen solubility and on the other hand of austenite which has a low diffusivity for hydrogen and a high solubility. The solubility of hydrogen in the austenite phase is two or three orders of magnitudes higher than in the ferrite phase, while the diffusion in the ferrite phase is up to five orders of magnitudes faster compared to the austenite phase. Duplex stainless steel 2205 is considered to be very susceptible to HE because of the fast diffusion in ferrite and the high hydrogen solubility in austenite, the combination which leads to a fast reaching of the critical hydrogen concentration [165–167]. According to the standards ISO 15156-1:2020 and ISO 15156-3:2020 [159,162], Duplex stainless steel can be used up to a H_2S content of 0.02 bar. Although the present tests we done at much higher contents, the use of Duplex stainless steel in H_2 atmospheres is not recommended. Since one fracture has occurred at 0.9 × YS, it is absolutely not recommended to use this material in hydrogen environments. Duplex stainless steels can be significantly affected by hydrogen embrittlement and should be avoided in the construction of underground storage facilities or according to [32] shall only be used at low stress levels in dry hydrogen gas.

6 Summary

In the course of decarbonization, numerous processes in industry, energy generation and transport must be converted to operate with hydrogen. One of the challenges is that hydrogen negatively affects the mechanical properties of metallic materials and can subsequently lead to material damage. Therefore, the aim of this work was to find various casing and tubing materials for completion of wellbores in depleted fields or other underground storage facilities, to find suitable materials for hydrogen storage. In order to find out the application limits of interesting carbon steels as well as of corrosion resistant steels applied in underground storage facilities, conclusion with respect to the results and also with consideration of ISO 15156 were established. From the results, it can be seen that the hydrogen uptake for carbon steels is low under dry conditions. This situation changes when an electrolyte and in addition H_2S are present. For stainless steels compared to carbon steels, the results show a significant higher hydrogen uptake.

Table 12 provides an overview of the applicability of all investigated steels for their use in hydrogen storage. In Table 12, the applicability is indicated by a color code. Materials showing no cracking in Constant Load Testing and neither or very minor localized corrosive attack are considered as „Applicable". Materials showing localized corrosive attack although no cracking occurred in Constant Load Testing are considered as „Applicable with limitations". Finally, materials that failed during Constant Load Testing are considered as „Not applicable". The tests in this work were carried out with various gas compositions and temperatures. The tests with sour gas composition (gas C and D) were performed with 1 bar H_2S, which is considered as severe in comparison to the standards of the ISO 15156 series [159,162,168].

Table 12: Applicability in H₂ environment of all investigated steels, 3ʳᵈ column from ISO 15156 [159,162,168]

Material	Damage	Application with H_2S based on ISO 15156	Applicability in H_2 environment
20MnV5	no damage	Not specified	well applicable
welded J55	no damage	Acceptable for H_2S application if hardness ≤ 22 HRC	well applicable
welded J55 pre-corroded	no damage		
welded J55 with notch	no damage		
K55	no damage	Acceptable for H_2S application for all temperatures	well applicable when localized corrosion is not an issue
K55 pre-corroded	no damage		
K55 with notch	some localized damage		
welded K55	no damage	Acceptable for H_2S application if hardness ≤ 22 HRC	well applicable
L80	deep localized damage	Acceptable for H_2S application for all temperatures provided that it is type 1	applicable when localized corrosion is not an issue
L80 pre-corroded	some localized damage		
L80 with notch	some localized damage		
P110	deep localized damage	Acceptable for H_2S application only if T° > 80°C	applicable at RT when no H_2S is present
quenched material	failure in H_2	Not applicable	not applicable
13%Cr	no damage	Acceptable if pH_2S < 10.2 kPA	well applicable
316L IGS	no damage	Acceptable if pH_2S < 10.2 kPA	well applicable
316L Vallourec	no damage		well applicable
Duplex 2205	failure in (H_2 + CO_2 + H_2S)	Acceptable if pH_2S < 2 kPA	not applicable
Alloy 625	no damage	Acceptable for H_2S application for all temperatures	well applicable

increasing yield strength

increasing alloy content

no damage	localized damage	failure

well applicable in hydrogen environment	applicable in hydrogen environment when localized corrosion is not an issue	not applicable in hydrogen environment

For carbon steels, there is no concern at all in dry conditions, as in these conditions the hydrogen uptake was low and no localized corrosive damage occurred at the surface. Adding H_2S and an electrolyte did not cause any problems like cracking or failure at lower strength materials, although more hydrogen was uptaken. The two welded steel grades show no localized corrosive attack. For higher strength carbon steel L80 in the presence of electrolyte and H_2S, there is a localized corrosive attack. Therefore it can be used with some limitations regarding H_2S, although this is assumed to be uncritical in the standard ISO 15156-1:2020 [159]. The even higher strength carbon steel P110 should be considered with a certain risk for sour gas applications. The local damage of P110 was more pronounced than for L80. Fracture has only occurred in the case of the quenched material, which was only used as a qualifying material for verifying a sufficient aggressivity of the chosen experimental set-up. All stainless steels tested are recommended as suitable materials for tubings and casings, with the exception of duplex stainless steel 2205.

There are no qualification standards for H_2 use in wells yet. Based on the results of the present thesis, Vallourec Mannesmann has qualified a number of its materials for hydrogen use (Figure 105) [169,170].

Figure 105: Material qualification for hydrogen applications based on the results of Hystories [169]

7 References

[1] E. Wendler-Kalsch, H. Gräfen, Korrosionsschadenkunde, Springer Berlin Heidelberg, Berlin, Heidelberg, 1998 612

[2] A. Trautmann, G. Mori, M. Oberndorfer, S. Bauer, C. Holzer, C. Dittmann, Hydrogen Uptake and Embrittlement of Carbon Steels in Various Environments, Materials 13 (2020) 3604

[3] https://hystories.eu/project-hystories/ accessed on May 8, 2023

[4] M. Newborough, G. Cooley, Developments in the global hydrogen market: The spectrum of hydrogen colours, Fuel Cells Bulletin 2020 (2020) 16–22

[5] H. Kojima, K. Nagasawa, N. Todoroki, Y. Ito, T. Matsui, R. Nakajima, Influence of renewable energy power fluctuations on water electrolysis for green hydrogen production, International Journal of Hydrogen Energy 48 (2023) 4572–4593

[6] K. Caldeira, A.K. Jain, M.I. Hoffert, Climate sensitivity uncertainty and the need for energy without CO_2 emission, Science 299 (2003) 2052–2054

[7] C.-H. Yu, C.-H. Huang, C.-S. Tan, A Review of CO_2 Capture by Absorption and Adsorption, Aerosol and Air Quality Research 12 (2012) 745–769

[8] P.A. Owusu, S. Asumadu-Sarkodie, A review of renewable energy sources, sustainability issues and climate change mitigation, Cogent Engineering 3 (2016) 1167990

[9] https://www.iea.org/reports/co2-emissions-in-2022 accessed on April 18, 2023

[10] M. Noussan, P.P. Raimondi, R. Scita, M. Hafner, The Role of Green and Blue Hydrogen in the Energy Transition—A Technological and Geopolitical Perspective, Sustainability 13 (2021) 298

[11] L. Mosca, E. Palo, M. Colozzi, G. Iaquaniello, A. Salladini, S. Taraschi (Eds.), Hydrogen in chemical and petrochemical industry, 2020 387-410

[12] https://hydrogeneurope.eu/wp-content/uploads/2021/11/Clean-Hydrogen-Monitor-2020.pdf   accessed on April 19, 2023

[13] R. Tarkowski, B. Uliasz-Misiak, Towards underground hydrogen storage: A review of barriers, Renewable and Sustainable Energy Reviews 162 (2022) 112451

[14] https://www.afr.com/companies/energy/what-exactly-is-green-hydrogen-and-could-it-save-the-world-20220711-p5b0p9, available at https://www.afr.com/companies/energy/what-exactly-is-green-hydrogen-and-could-it-save-the-world-20220711-p5b0p9 accessed on May 15, 2023

[15] N.S. Muhammed, M.B. Haq, D.A. Al Shehri, A. Al-Ahmed, M.M. Rahman, E. Zaman, S. Iglauer, Hydrogen storage in depleted gas reservoirs: A comprehensive review, Fuel 337 (2023) 127032

[16] https://www.forbes.com/sites/forbestechcouncil/2020/08/31/a-look-at-the-colors-of-hydrogen-that-could-power-our-future/?sh=2b588e4f5e91 accessed on April 19, 2023

[17] https://power-to-x.de/wp-content/uploads/2021/09/H2-in-Farbe-Grafik-FINAL-870x675.png accessed on June 27, 2023

[18] R. Hefner, Toward sustainable economic growth: The age of energy gases, International Journal of Hydrogen Energy 20 (1995) 945–948

[19] D. Zivar, S. Kumar, J. Foroozesh, Underground hydrogen storage: A comprehensive review, International Journal of Hydrogen Energy 46 (2021) 23436–23462

[20] S. Niaz, T. Manzoor, A.H. Pandith, Hydrogen storage: Materials, methods and perspectives, Renewable and Sustainable Energy Reviews 50 (2015) 457–469

[21] R. Moradi, K.M. Groth, Hydrogen storage and delivery: Review of the state of the art technologies and risk and reliability analysis, International Journal of Hydrogen Energy 44 (2019) 12254–12269

[22] L. Schlapbach, A. Züttel, Hydrogen-storage materials for mobile applications, in: Materials for Sustainable Energy 414, 265–270

[23] C. Sambo, A. Dudun, S.A. Samuel, P. Esenenjor, N.S. Muhammed, B. Haq, A review on worldwide underground hydrogen storage operating and potential fields, International Journal of Hydrogen Energy 47 (2022) 22840–22880

[24] W. M. Mueller, J. P. Blackledge, G. Libowitz, Metal Hydrides: No. TID-25030 (1968) 804

[25] B. Sakinatuna, Lamaridarkrim F., M. HIRSCHER, Metal hydride materials for solid hydrogen storage: A review, International Journal of Hydrogen Energy 32 (2007) 1121–1140

[26] G.S. A. Martinez-Mesa, Adsorption of Molecular Hydroegn on Nanostructured Surfaces, Revista Cubana de Fisica 31 (2014) 32–34

[27] D.P. Broom, C.J. Webb, K.E. Hurst, P.A. Parilla, T. Gennett, C.M. Brown, R. Zacharia, E. Tylianakis, E. Klontzas, G.E. Froudakis, T.A. Steriotis, P.N. Trikalitis, D.L. Anton, B. Hardy, D. Tamburello, C. Corgnale, B.A. van Hassel, D. Cossement, R. Chahine, M. Hirscher, Outlook and challenges for hydrogen storage in nanoporous materials, Applied Physics A 122 (2016) 1-21

[28] W. Oelerich, T. Klassen, R. Bormann, Metal oxides as catalysts for improved hydrogen sorption in nanocrystalline Mg-based materials, Journal of Alloys and Compounds 315 (2001) 237–242

[29] S.-I. Orimo, Y. Nakamori, J.R. Eliseo, A. Züttel, C.M. Jensen, Complex hydrides for hydrogen storage, Chemical reviews 107 (2007) 4111–4132

[30] J. Ren, N.M. Musyoka, H.W. Langmi, M. Mathe, S. Liao, Current research trends and perspectives on materials-based hydrogen storage solutions: A critical review, International Journal of Hydrogen Energy 42 (2017) 289–311

[31] N. Stetson, An overview of U.S. DOE's activities for hydrogen fuel cell technologies: Fuel Cell Technologies, U.S. Department of Energy 12 (2012) 1-41

[32] L.E. Hayden, M.E. Ulucakli, Design guidelines for hydrogen piping and pipelines, New York, NY, 2007 1-32

[33] W. Johnson, On some remarkable changes produced in iron and steel by the action of hydrogen and acids, Proceedings of the Royal Society of London 23 (1875) 168–179

[34] J. Venezuela, Q. Liu, M. Zhang, Q. Zhou, A. Atrens, A review of hydrogen embrittlement of martensitic advanced high-strength steels, Corrosion Reviews 34 (2016) 153–186

[35] T.J. Carter, L.A. Cornish, Hydrogen in metals, Engineering Failure Analysis 8 (2001) 113–121

[36] J. Villalobos, A. Del-Pozo, B. Campillo, J. Mayen, S. Serna, Microalloyed Steels through History until 2018: Review of Chemical Composition, Processing and Hydrogen Service, Metals 8 (2018) 351

[37] M.R. Louthan, Hydrogen Embrittlement of Metals: A Primer for the Failure Analyst, Journal of Failure Analysis and Prevention 8 (2008) 289–307

[38] S.M. Myers, M.I. Baskes, H.K. Birnbaum, J.W. Corbett, G.G. DeLeo, S.K. Estreicher, E.E. Haller, P. Jena, N.M. Johnson, R. Kirchheim, S.J. Pearton, M.J. Stavola, Hydrogen interactions with defects in crystalline solids, Reviews of Modern Physics 64 (1992) 559–617

[39] E. Protopopoff, Surface Effects on Hydrogen Entry into Metals, in: P. Marcus (Ed.), Corrosion Mechanisms in Theory and Practice, 3rd ed., CRC Press, Boca Raton, 2012, 105–148

[40] A. Turnbull, Hydrogen diffusion and trapping in metals, in: Gaseous Hydrogen Embrittlement of Materials in Energy Technologies, Elsevier, 2012 89-128

[41] J. Tafel, Über die Polarisation bei kathodischer Wasserstoffentwicklung, Zeitschrift für Physikalische Chemie 50 (1905) 641–712

[42] M. Bhardwaj, R. Balasubramaniam, Uncoupled non-linear equations method for determining kinetic parameters in case of hydrogen evolution reaction following Volmer–Heyrovsky–Tafel mechanism and Volmer–Heyrovsky mechanism, International Journal of Hydrogen Energy 33 (2008) 2178–2188

[43] G.B. Rawls, T. Adams, N.L. Newhouse, Hydrogen production and containment, in: Gaseous hydrogen embrittlement of materials in energy technologies: The problem, its characterisation and effects on particular, Woodhead Publishing Ltd, Cambridge, 2012 3-50

[44] A. Sieverts, W. Krumbhaar, Über die Löslichkeit von Gasen in Metallen und Legierungen, Berichte der deutschen chemischen Gesellschaft 43 (1910) 893–900

[45] S. Pillot, L. Coudreuse, Hydrogen-induced disbonding and embrittlement of steels used in petrochemical refining, in: Gaseous Hydrogen Embrittlement of Materials in Energy Technologies, Elsevier, 2012 51-93

[46] A. San-Martin, F.D. Manchester, The Fe-H (Iron-Hydrogen) system, Bulletin of Alloy Phase Diagrams 11 (1990) 173–184

[47] K. J. Lakshminarayans Iyer, E.G. Ramachandran, J. Ruge, Austenite stabilization in stainless steel by hydrogen, Archiv für das Eisenhüttenwesen 49 (1978) 461–462

[48] A.R. Kucernak, C. Zalitis, General Models for the Electrochemical Hydrogen Oxidation and Hydrogen Evolution Reactions: Theoretical Derivation and Experimental Results under Near Mass-Transport Free Conditions, The Journal of Physical Chemistry C 120 (2016) 10721–10745

[49] M.W. Breiter, Reaction mechanisms of the H2 oxidation/evolution reaction, in: W. Vielstich, A. Lamm, H.A. Gasteiger, H. Yokokawa (Eds.), Handbook of Fuel Cells, John Wiley & Sons, Ltd, Chichester, UK, 2010 1136

[50] A. Lasia (Ed.), Hydrogen evolution reaction: Fundamentals, technology and applications, Wiley Interscience, Hoboken, NJ, 2010 878-886

[51] J. Rehrl, Wasserstoffversprödung in hochfesten, mikrolegierten Stählen: Dissertation TU München, München, 2014

[52] C.E. Mortimer, U. Müller, Chemie: Das Basiswissen der Chemie, Georg Thieme Verlag, Stuttgart, 2020 717

[53] M.A. Mohtadi-Bonab, J.A. Szpunar, S.S. Razavi-Tousi, A comparative study of hydrogen induced cracking behavior in API 5L X60 and X70 pipeline steels, Engineering Failure Analysis 33 (2013) 163–175

[54] C. Dong, K. Xiao, Z. Liu, W. Yang, X. Li, Hydrogen induced cracking of X80 pipeline steel, International Journal of Minerals, Metallurgy, and Materials 17 (2010) 579–586

[55] P. Bai, J. Zhou, B. Luo, S. Zheng, P. Wang, Y. Tian, Hydrogen embrittlement of X80 pipeline steel in H2S environment: Effect of hydrogen charging time, hydrogen-trapped state and hydrogen charging–releasing–recharging cycles, International Journal of Minerals, Metallurgy and Materials 27 (2020) 63–73

[56] R.N. Iyer, I. Takeuchi, M. Zamanzadeh, H.W. Pickering, Hydrogen Sulfide Effect on Hydrogen Entry into Iron—A Mechanistic Study, Corrosion 46 (1990) 460–468

[57] A.E. Lewis, Review of metal sulphide precipitation, Hydrometallurgy 104 (2010) 222–234

[58] A. Kawahima, K. Hashimoto, S. Shimodaira, Hydrogen Electrode Reaction and Hydrogen Embrittlement of Mild Steel in Hydrogen Sulfide Solutions, Corrosion 32 (1976) 321–331

[59] M.C. Folena, J.A.d.C. Ponciano, Assessment of hydrogen embrittlement severity of an API 5LX80 steel in H2S environments by integrated methodologies, Engineering Failure Analysis 111 (2020) 104380

[60] F. Huang, P. Cheng, X.Y. Zhao, J. Liu, Q. Hu, Y.F. Cheng, Effect of sulfide films formed on X65 steel surface on hydrogen permeation in H2S environments, International Journal of Hydrogen Energy 42 (2017) 4561–4570

[61] E. Snape, H2S Corrosion in Oil & Gas Production: Sulfide Stress Corrosion of Some Medium and Low Alloy Stee, NACE, Houston (TX) 1981 101-128

[62] D. Garcia, R.N. Carvalho, V. Lins, D.M. Rezende, D.S. Dos Santos, Influence of microstructure in the hydrogen permeation in martensitic-ferritic stainless steel, International Journal of Hydrogen Energy 40 (2015) 17102–17109

[63] A. Fick, Ueber Diffusion, Annalen der Physik und Chemie 170 (1855) 59–86

[64] M. Nagumo, Fundamentals of Hydrogen Embrittlement, Springer Singapore, Singapore, 2016 241

[65] G. Gottstein, Materialwissenschaft und Werkstofftechnik, Springer Berlin Heidelberg, Berlin, Heidelberg, 2014 642

[66] P.F. A. McNabb, A new analysis of the diffusion of hydrogen in iron and ferritic steels, Transactions of the Metallurgical Society of AIME 227 (1963) 618–627

[67] H.-J. Christ, M. Decker, S. Zeitler, Hydrogen diffusion coefficients in the titanium alloys IMI 834, Ti 10-2-3, Ti 21 S, and alloy C, Metallurgical and Materials Transactions A 31 (2000) 1507–1517

[68] H. Mehrer, Diffusion in solids: Fundamentals, methods, materials, diffusion-controlled processes, Springer, Berlin, New York, 2007 651

[69] H.-J. Bargel, G. Schulze, Werkstoffkunde, Springer Berlin Heidelberg, Berlin, Heidelberg, 2018 544

[70] A.S. Nowick (Ed.), Diffusion in solids: Recent developments, Acad. Press, New York, NY, 1975 491

[71] S. Lynch, Hydrogen embrittlement phenomena and mechanisms, Corrosion Reviews 30 (2012) 105–123

[72] F.D. Fischer, G. Mori, J. Svoboda, Modelling the influence of trapping on hydrogen permeation in metals, Corrosion Science 76 (2013) 382–389

[73] M. A. V. Devanathan and Z. Stachurski, The adsorption and diffusion of electrolytic hydrogen in palladium, Proceedings of the Royal Society of London. Series A. Mathematical and Physical Sciences 270 (1962) 90–102

[74] ÖNORM EN ISO 17081-2014-10-01 EN ISO 17081, Elektrochemisches Verfahren zur Messung der Wasserstoffpermeation und zur Bestimmung von Wasserstoffaufnahme und -transport in Metallen, 2014

[75] W. Siegl, G. Mori, Hydrogen trapping in heat treated and deformed Armco iron, NACE International (2019), paper 13083

[76] The process of diffusion through a rubber membrane, Proceedings of the Royal Society of London. Series A, Containing Papers of a Mathematical and Physical Character 97 (1920) 286–307

[77] V.A. Somenkov, S.S. Shil'stein, Phase transitions of hydrogen in metals, Progress in Materials Science 24 (1980) 267–335

[78] Y. Fukai, The metal-hydrogen system: Basic bulk properties, Springer, Berlin, New York, 2005 497

[79] R. Kirchheim, Solid Solutions of Hydrogen in Complex Materials, In Solid State Physics, Elsevier (2004) 203–291

[80] R. Oriani, The diffusion and trapping of hydrogen in steel, Acta Metallurgica 18 (1970) 147–157

[81] M. Koyama, M. Rohwerder, C.C. Tasan, A. Bashir, E. Akiyama, K. Takai, D. Raabe, K. Tsuzaki, Recent progress in microstructural hydrogen mapping in steels: quantification, kinetic analysis, and multi-scale characterisation, Materials Science and Technology 33 (2017) 1481–1496

[82] H.E. Kissinger, Reaction Kinetics in Differential Thermal Analysis, Analytical Chemistry 29 (1957) 1702–1706

[83] L. Daoming, P. R. Gangloff, J. R. Scully, Hydrogen Trap States in Ultrahigh-Strength AERMET 100 Steel, Metallurgical and Materials Transactions 35A (2004) 849

[84] M. Dadfarnia, P. Sofronis, T. Neeraj, Hydrogen interaction with multiple traps: Can it be used to mitigate embrittlement?, International Journal of Hydrogen Energy 36 (2011) 10141–10148

[85] G.M. Pressouyre, A classification of hydrogen traps in steel, Metallurgical and Materials Transactions A 10 (1979) 1571–1573

[86] E. Hornbogen, H. Warlimont, B. Skrotzki, Metalle, Springer Berlin Heidelberg, Berlin, Heidelberg, 2019 429

[87] https://www.tec-science.com/de/werkstofftechnik/aufbau-der-metalle/gitterbaufehler-gitterdefekte-gitterfehler/ accessed on April 26, 2023

[88] J.P. Hirth, Effects of hydrogen on the properties of iron and steel, Metallurgical and Materials Transactions A 11 (1980) 861–890

[89] J. Friedl, On the electronic structure of hydrogen in metals: The possible electronic structure of hydrogen in ordinary metals and alloys, transitional metals and rare earth metals is discussed, with an emphasis on dilute solutions, Berichte der Bunsengesellschaft für physikalische Chemie - Electronic Properties 76 (1972) 828–831

[90] J.K. Tien, R.J. Richards, O. Buck, H.L. Marcus, Model of dislocation sweep-in of hydrogen during fatigue crack growth, Scripta Metallurgica 9 (1975) 1097–1101

[91] L. Chen, X. Xiong, X. Tao, Y. Su, L. Qiao, Effect of dislocation cell walls on hydrogen adsorption, hydrogen trapping and hydrogen embrittlement resistance, Corrosion Science 166 (2020) 108428

[92] T. Michler, J. Naumann, M. Hock, K. Berreth, M.P. Balogh, E. Sattler, Microstructural properties controlling hydrogen environment embrittlement of cold worked 316 type austenitic stainless steels, Materials Science and Engineering: A 628 (2015) 252–261

[93] M.R. Louthan, G.R. Caskey, Hydrogen transport and embrittlement in structural metals, International Journal of Hydrogen Energy 1 (1976) 291–305

[94] T. Michler, J. Naumann, Microstructural aspects upon hydrogen environment embrittlement of various bcc steels, International Journal of Hydrogen Energy 35 (2010) 821–832

[95] S. Bechtle, M. Kumar, B.P. Somerday, M.E. Launey, R.O. Ritchie, Grain-boundary engineering markedly reduces susceptibility to intergranular hydrogen embrittlement in metallic materials, Acta Materialia 57 (2009) 4148–4157

[96] X. Wang, Y. Zhao, G. Cheng, Y. Zhang, T.A. Venkatesh, Hydrogen adsorption in phase and grain boundaries of pearlitic steels and its effects on tensile strength, MRS Advances 7 (2022) 383–387

[97] M. Elboujdaini, W. Revie, Effect of Non-Metallic Inclusions on Hydrogen Induced Cracking, in: T. Boukharouba, M. Elboujdaini, G. Pluvinage (Eds.), Damage and Fracture Mechanics, Springer Netherlands, Dordrecht, 2009 11-18

[98] T. Das, S.K. Rajagopalan, S.V. Brahimi, X. Wang, S. Yue, A study on the susceptibility of high strength tempered martensite steels to hydrogen embrittlement (HE) based on incremental step load (ISL) testing methodology, Materials Science and Engineering: A 716 (2018) 189–207

[99] M. Asadipoor, A. Pourkamali Anaraki, J. Kadkhodapour, S. Sharifi, A. Barnoush, Macro- and microscale investigations of hydrogen embrittlement in X70 pipeline steel by in-situ and ex-situ hydrogen charging tensile tests and in-situ electrochemical micro-cantilever bending test, Materials Science and Engineering: A 772 (2020) 138762

[100] C.F. Dong, Z.Y. Liu, X.G. Li, Y.F. Cheng, Effects of hydrogen-charging on the susceptibility of X100 pipeline steel to hydrogen-induced cracking, International Journal of Hydrogen Energy 34 (2009) 9879–9884

[101] J.C. Villalobos, A. Del-Pozo, J. Mayen, S. Serna, B. Campillo, Hydrogen embrittlement suscetibility on X-120 microalloyed steel as function of tempering temperature, International Journal of Hydrogen Energy 45 (2020) 9137–9148

[102] H.K.D.H. Bhadeshia, Prevention of Hydrogen Embrittlement in Steels, ISIJ International 56 (2016) 24–36

[103] A. Turnbull, R.B. Hutchings, Analysis of hydrogen atom transport in a two-phase alloy, Materials Science and Engineering 177 (1994) 161–171

[104] L. Bacchi, F. Biagini, S. Corsinovi, M. Romanelli, M. Villa, R. Valentini, Influence of Thermal Treatment on SCC and HE Susceptibility of Supermartensitic Stainless Steel 16Cr5NiMo, Materials 13 (2020) 1643

[105] A. R.Troiano, The Role of Hydrogen and Other Interstitials in the Mechanical Behavior of Metals, Metallography, Microstructure, and Analysis 5 (2016) 557–569

[106] R. A. Oriani, A mechanistic theory of hydrogen embrittlement of steels, Ber Bunsenges Phys Chem 76 (1972) 848–857

[107] R.A. Oriani, P.H. Josephic, Testing of the decohesion theory of hydrogen-induced crack propagation, Scripta Metallurgica 6 (1972) 681–688

[108] H. Wriedt, R. Oriani, Effect of tensile and compressive elastic stress on equilibrium hydrogen solubility in a solid, Acta Metallurgica 18 (1970) 753–760

[109] Y. Liang, P. Sofronis, Toward a phenomenological description of hydrogen-induced decohesion at particle/matrix interfaces, Journal of the Mechanics and Physics of Solids 51 (2003) 1509–1531

[110] I.M. Robertson, P. Sofronis, A. Nagao, M.L. Martin, S. Wang, D.W. Gross, K.E. Nygren, Hydrogen Embrittlement Understood, Metallurgical and Materials Transactions A 46 (2015) 2323–2341

[111] J. Liu, M. Zhao, L. Rong, Overview of hydrogen-resistant alloys for high-pressure hydrogen environment: on the hydrogen energy structural materials, Clean Energy 7 (2023) 99–115

[112] S.P. Lynch, Hydrogen embrittlement (HE) phenomena and mechanisms, in: Stress Corrosion Cracking 2011, 90-130

[113] C.D. Beachem, A new model for hydrogen-assisted cracking (hydrogen "embrittlement"), Metallurgical and Materials Transactions B 3 (1972) 441–455

[114] I.M. Robertson, The effect of hydrogen on dislocation dynamics, Engineering Fracture Mechanics 64 (1999) 649–673

[115] S.P. Lynch, Metallographic and fractographic techniques for characterising and understanding hydrogen-assisted cracking of metals, in: Gaseous Hydrogen Embrittlement of Materials 2012, 274–346

[116] H.K. Birnbaum, I.M. Robertson, P. Sofronis, D. Teter, Mechanisms of Hydrogen Related Fracture - A Review, in: Corrosion-Deformation Interactions CDI'96, 172–195

[117] S.P. Lynch, Environmentally assisted cracking: Overview of evidence for an adsorption-induced localised-slip process, Acta Metallurgica 36 (1988) 2639–2661

[118] S.P. Lynch, Metallographic contributions to understanding mechanisms of environmentally assisted cracking, Metallography 23 (1989) 147–171

[119] N.J. Petch, The lowering of fracture-stress due to surface adsorption, Philosophical Magazine 1 (1956) 331–337

[120] J.A. Clum, The role of hydrogen in dislocation generation in iron alloys, Scripta Metallurgica 9 (1975) 51–58

[121] V. Madina, I. Azkarate, Compatibility of materials with hydrogen. Particular case: Hydrogen embrittlement of titanium alloys, International Journal of Hydrogen Energy 34 (2009) 5976–5980

[122] Z. Kacenka, M. Roudnicka, O. Ekrt, D. Vojtech, High susceptibility of 3D-printed Ti-6Al-4V alloy to hydrogen trapping and embrittlement, Materials Letters 301 (2021) 130334

[123] X. Liu, J. Wang, L. Gao, R. Li, X. Luo, W. Zhang, X. Zhang, X. Zha, Surface concentration and microscale distribution of hydrogen and the associated embrittlement in a near α titanium alloy, Journal of Alloys and Compounds 862 (2021) 158669

[124] Y. Chang, A.J. Breen, Z. Tarzimoghadam, P. Kürnsteiner, H. Gardner, A. Ackerman, A. Radecka, P.A. Bagot, W. Lu, T. Li, E.A. Jägle, M. Herbig, L.T. Stephenson, M.P. Moody, D. Rugg, D. Dye, D. Ponge, D. Raabe, B.

Gault, Characterizing solute hydrogen and hydrides in pure and alloyed titanium at the atomic scale, Acta Materialia 150 (2018) 273–280

[125] S.P. Lynch, Mechanisms and Kinetics of Environmentally Assisted Cracking: Current Status, Issues, and Suggestions for Further Work, Metallurgical and Materials Transactions A 44 (2013) 1209–1229

[126] https://www.h2inframap.eu/ accessed on April 25, 2023

[127] https://www.gasconnect.at/aktuelles/news-presse/news/detail/News/wasserstoff-importmoeglichkeiten-fuer-oesterreich-ab-2030 accessed on April 26, 2023

[128] N. Heinemann, M.G. Booth, R.S. Haszeldine, M. Wilkinson, J. Scafidi, K. Edlmann, Hydrogen storage in porous geological formations – onshore play opportunities in the midland valley (Scotland, UK), International Journal of Hydrogen Energy 43 (2018) 20861–20874

[129] H. Balat, E. Kırtay, Hydrogen from biomass – Present scenario and future prospects, International Journal of Hydrogen Energy 35 (2010) 7416–7426

[130] https://www.storengy.com/en/our-offers-and-services/underground-storage/our-types-storage-facilities accessed on April 17, 2023

[131] R. Tarkowski, Underground hydrogen storage: Characteristics and prospects, Renewable and Sustainable Energy Reviews 105 (2019) 86–94

[132] P. Carden, L. Peterson, Physical, chemical and energy aspects of underground hydrogen storage, International Journal of Hydrogen Energy 4 (1979) 559–569

[133] J. Michalski, U. Bünger, F. Crotogino, S. Donadei, G.-S. Schneider, T. Pregger, K.-K. Cao, D. Heide, Hydrogen generation by electrolysis and storage in salt caverns: Potentials, economics and systems aspects with regard to the German energy transition, International Journal of Hydrogen Energy 42 (2017) 13427–13443

[134] S. Foh, M. Novil, E. Rockar, P. Randolph, Underground hydrogen storage. Final report. [Salt caverns, excavated caverns, aquifers and depleted fields], 1979 108932922

[135] A. S. Lord, Overview of Geologic Storage of Natural Gas with an Emphasis on Assessing the Feasibility of Storing Hydrogen, Sandia National Laboratories (2009) 1-28

[136] N. Heinemann, J. Alcalde, J.M. Miocic, S.J.T. Hangx, J. Kallmeyer, C. Ostertag-Henning, A. Hassanpouryouzband, E.M. Thaysen, G.J. Strobel, C. Schmidt-Hattenberger, K. Edlmann, M. Wilkinson, M. Bentham, R. Stuart Haszeldine, R. Carbonell, A. Rudloff, Enabling large-scale hydrogen storage in porous media – the scientific challenges, Energy & Environmental Science 14 (2021) 853–864

[137] E.M. Thaysen, S. McMahon, G.J. Strobel, I.B. Butler, B.T. Ngwenya, N. Heinemann, M. Wilkinson, A. Hassanpouryouzband, C.I. McDermott, K. Edlmann, Estimating microbial growth and hydrogen consumption in hydrogen storage in porous media, Renewable and Sustainable Energy Reviews 151 (2021) 111481

[138] S.M. Jafari Raad, Y. Leonenko, H. Hassanzadeh, Hydrogen storage in saline aquifers: Opportunities and challenges, Renewable and Sustainable Energy Reviews 168 (2022) 112846

[139] Z. Bo, L. Zeng, Y. Chen, Q. Xie, Geochemical reactions-induced hydrogen loss during underground hydrogen storage in sandstone reservoirs, International Journal of Hydrogen Energy 46 (2021) 19998–20009

[140] E. Alireza, Characterization of geochemical interactions and migration of hydrogen in sandstone sedimentary formations: application to geological storage, University of Orleans, Dissertation, 2017

[141] M. Perera, A review of underground hydrogen storage in depleted gas reservoirs: Insights into various rock-fluid interaction mechanisms and their impact on the process integrity, Fuel 334 (2023) 126677

[142] https://www.gaffneycline.com/sites/g/files/cozyhq681/files/2022-07/gaffneycline_underground_hydrogen_storage_article.pdf accessed on May 6, 2023

[143] V. Reitenbach, L. Ganzer, D. Albrecht, B. Hagemann, Influence of added hydrogen on underground gas storage: a review of key issues, Environmental Earth Sciences 73 (2015) 6927–6937

[144] S.G. Hagemann, W.K. Witt, M. Fiorentini, Introduction to using research to benefit mineral exploration, Australian Journal of Earth Sciences 61 (2014) 1-3

[145] A.I. Slobodkin, J. Wiegel, Fe(III) as an electron acceptor for H2 oxidation in thermophilic anaerobic enrichment cultures from geothermal areas, Extremophiles life under extreme conditions 1 (1997) 106–109

[146] M. Panfilov, Underground Storage of Hydrogen: In Situ Self-Organisation and Methane Generation, Transport in Porous Media 85 (2010) 841–865

[147] P. Miga, Methanogenic bacteria as a key factor involved in changes of town gas stored in an underground reservoir, FEMS Microbiology Letters 73 (1990) 221–224

[148] F. Buzek, V. Onderka, P. Vancura, I. Wolf, Carbon isotope study of methane production in a town gas storage reservoir, Fuel 73 (1994) 747–752

[149] R. Cord-Ruwisch, H.-J. Seitz, R. Conrad, The capacity of hydrogenotrophic anaerobic bacteria to compete for traces of hydrogen depends on the redox potential of the terminal electron acceptor, Archives of Microbiology 149 (1988) 350–357

[150] Serge van Gessel, Hydrogen TCP-Task42, Underground Hydrogen Storage: Technology Monitor Report 2023, IEA 1–168

[151] E.M. Thaysen, S. McMahon, G.J. Strobel, I.B. Butler, B.T. Ngwenya, N. Heinemann, M. Wilkinson, A. Hassanpouryouzband, C.I. McDermott, K. Edlmann, Estimating microbial growth and hydrogen consumption in hydrogen storage in porous media, Renewable and Sustainable Energy Reviews 151 (2021) 111481

[152] R.N. Akondi, S. Sharma, R.V. Trexler, P.J. Mouser, S.M. Pfiffner, Microbial lipid biomarkers detected in deep subsurface black shales, Environmental science. Processes & impacts 21 (2019) 291–307

[153] R.A. Daly, M.A. Borton, M.J. Wilkins, D.W. Hoyt, D.J. Kountz, R.A. Wolfe, S.A. Welch, D.N. Marcus, R.V. Trexler, J.D. MacRae, J.A. Krzycki, D.R. Cole, P.J. Mouser, K.C. Wrighton, Microbial metabolisms in a 2.5-km-deep ecosystem created by hydraulic fracturing in shales, Nature microbiology 1 (2016) 16146

[154] K. Mongird, V. Viswanathan, J. Alam, 2020 Grid Energy Storage Technology Cost and Performance Assessment: ESGC Cost Performance Report, Energy Storage Grand Challenge (2020) 1-117

[155] https://www.voestalpine.com/stahl/Produkte/Grobbleche/Hochfeste-Grobbleche accessed on March 15, 2023

[156] K.G. Solheim, J.K. Solberg, Hydrogen induced stress cracking in supermartensitic stainless steels – Stress threshold for coarse grained HAZ, Engineering Failure Analysis 32 (2013) 348–359

[157] H. Addach, P. Berçot, M. Rezrazi, M. Wery, Hydrogen permeation in iron at different temperatures, Materials Letters 59 (2005) 1347–1351

[158] https://www.forschung-und-wissen.de/nachrichten/technik/gasleitungen-in-deutschland-sind-bereit-fuer-wasserstoff-13377194 accessed May 12, 2023

[159] ISO 15156-1:2020, Petroleum and natural gas industries: Materials for use in H2S-containing environments in oil and gas production: General principles for selection of cracking-resistant, Austrian Standards International, 2020

[160] Standard Compressed Gas Association (CGA)/ Gas - CGA G-5.6 Hydrogen Pipeline System, 2005

[161] F. D. Gregory, Safety Standard for hydrogen and hydrogen systems: Guidelines for Hydrogen System Design, Materials Selection, Operations, Storage, and Transportation, Office of Safety and Mission Assurance, NASA Document NSS 1740 (1997) 1-389

[162] ISO 15156-3:2020, Petroleum and natural gas industries — Materials for use in H2S-containing environments in oil and gas production: Cracking-resistant CRAs, Austrian Standards International, 2020

[163] J. Xu, Z. Hao, Z. Fu, X. He, H. Wang, G. Xu, Hydrogen embrittlement behavior of selective laser-melted Inconel 718 alloy, Journal of Materials Research and Technology 23 (2023) 359–369

[164] O. Faye, J. Szpunar, U. Eduok, A critical review on the current technologies for the generation, storage, and transportation of hydrogen, International Journal of Hydrogen Energy 47 (2022) 13771–13802

[165] P. Tao, F. Ye, W. Cen, J. Zhao, Y. Wang, J. Gong, Analysis of enhanced hydrogen embrittlement fracture for pre-strain hardening 2205 duplex stainless steel, Results in Physics 16 (2020) 102820

[166] T. Zakroczymski, E. Owczarek, Electrochemical investigation of hydrogen absorption in a duplex stainless steel, Acta Materialia 50 (2002) 2701–2713

[167] E. Owczarek, T. Zakroczymski, Hydrogen transport in a duplex stainless steel, Acta Materialia 48 (2000) 3059–3070

[168] ISO 15156-2:2020, Petroleum and natural gas industries — Materials for use in H2S-containing environments in oil and gas production: Cracking-resistant carbon and low-alloy steels, and the, Austrian Standards International, 2020

[169] https://www.vallourec.com/en/all-news/group-2022-hydrogen-materials accessed on May 12, 2023

[170] https://hystories.eu/wp-content/uploads/2022/05/Hystories_D4.4-0-Summary-report-on-steels-K55-L80-including-H2S-containing-atmosphere-and-a-quenched-reference-material.pdf accessed on January 12, 2022

8 Appendix

Table 13: Stereo microscope images of the welded steel J55 in different gases with and without an electrolyte at RT
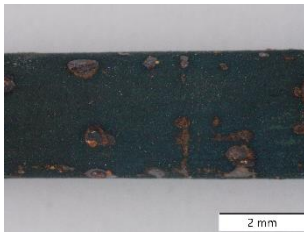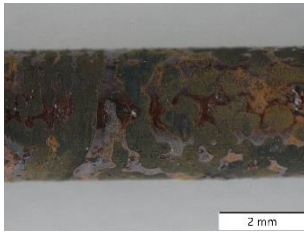
welded J55, 25°C	1 g/l NaCl	200 g/l NaCl
Gas A		
Gas B		
Gas C		
Gas D		

Table 14: Stereo microscope images of the welded steel J55 in different gases with and without an electrolyte at 120 °C
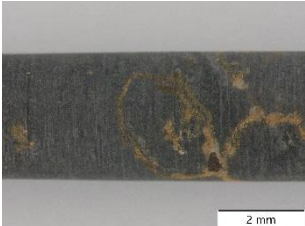
welded J55, 120°C	1 g/l NaCl	200 g/l NaCl
Gas A		
Gas B		
Gas C		
Gas D		
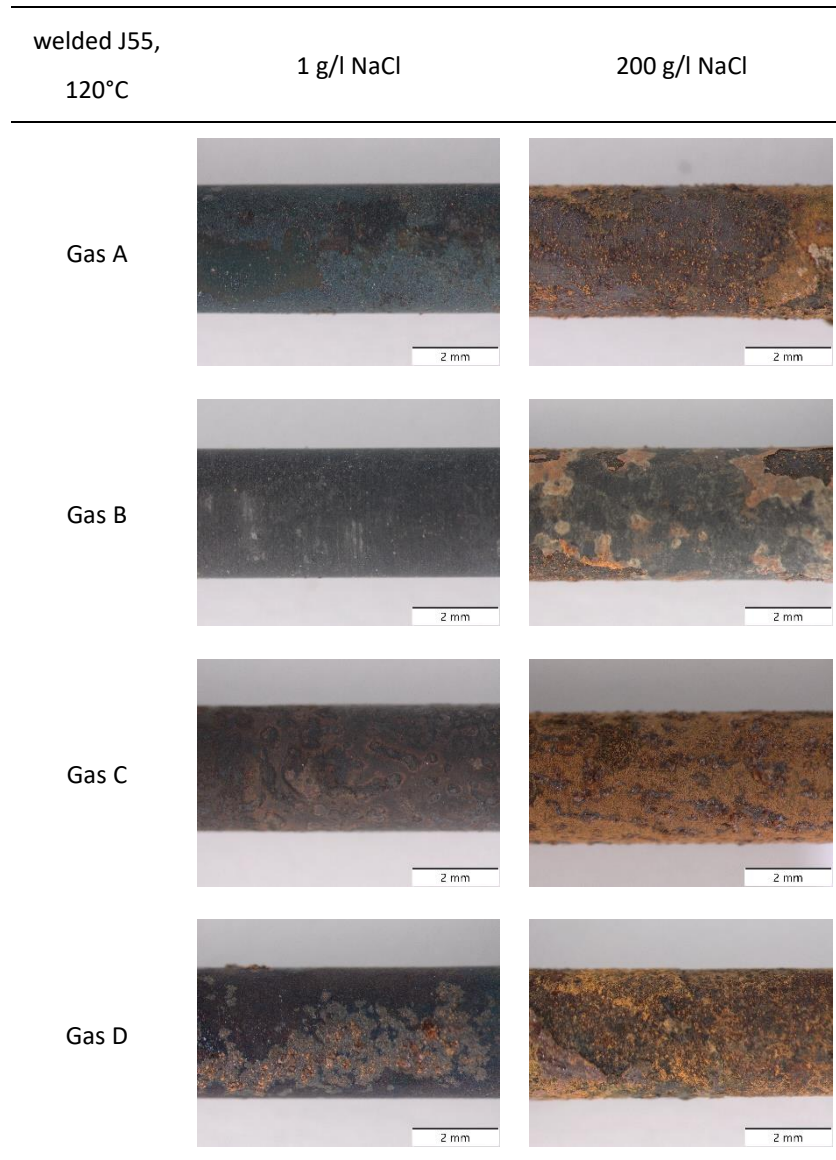
Table 15: Stereo microscope images of the welded steel J55 with a notched specimen in different gases with and without an electrolyte at RT

welded J55 notched, 25°C	dry	200 g/l NaCl
Gas A		
Gas B		
Gas C		
Gas D		
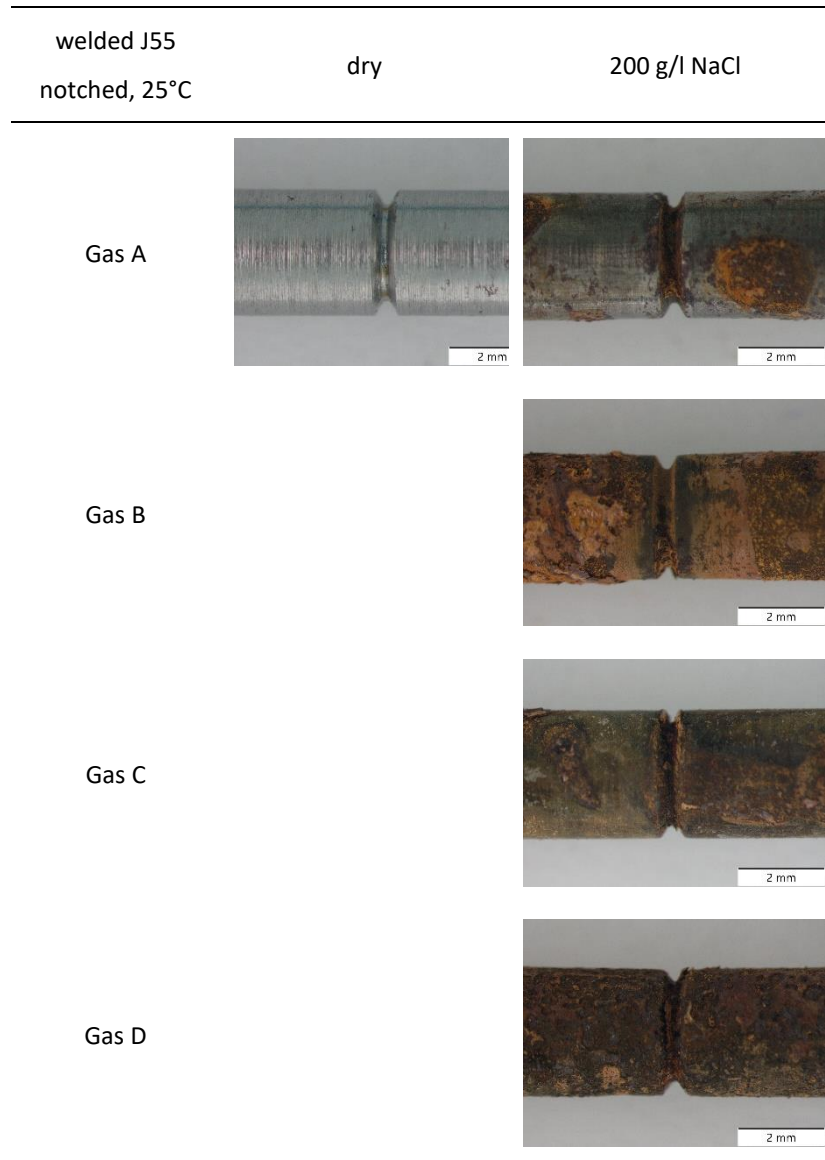
Table 16: Stereo microscope images of the pre-corroded welded steel J55 in different gases with and without an electrolyte at RT

welded J55, pre-corroded, 25°C	dry	200 g/l NaCl
Gas A		
Gas B		
Gas C		
Gas D		
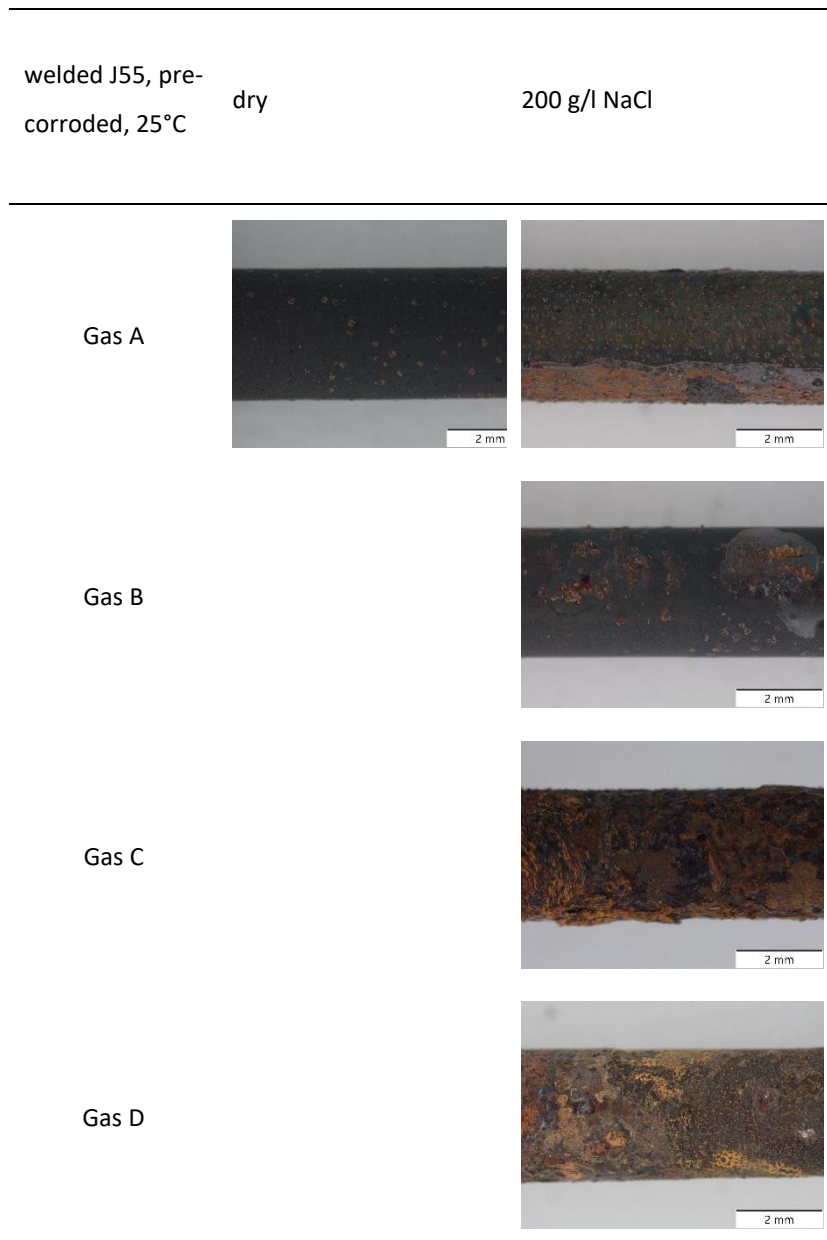
Table 17: Stereo microscope images of the steel K55 in different gases with and without an electrolyte at RT
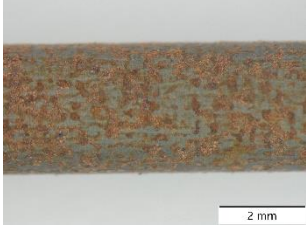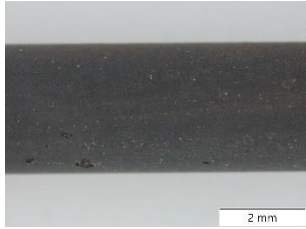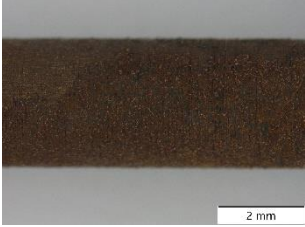
K55, 25°C	1 g/l [NaCl]	200 g/l [NaCl]
Gas A		
Gas B		
Gas C		
Gas D		

Table 18: Stereo microscope images of the steel K55 in different gases with and without an electrolyte at 120 °C
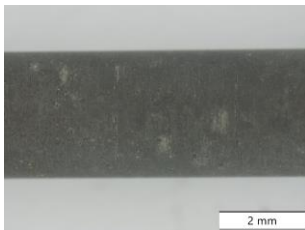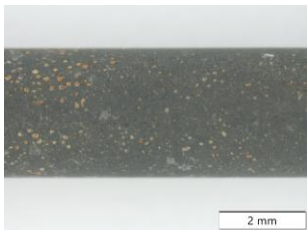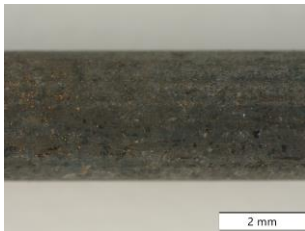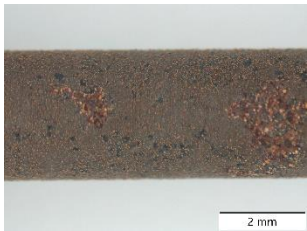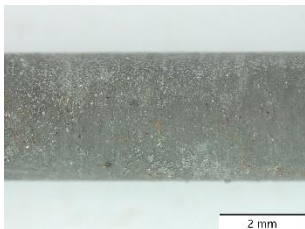
K55, 120°C	1 g/l [NaCl]	200 g/l [NaCl]
Gas A		
Gas B		
Gas C		
Gas D		

Table 19: Stereo microscope images of the steel K55 with a notch in different gases with and without an electrolyte at RT
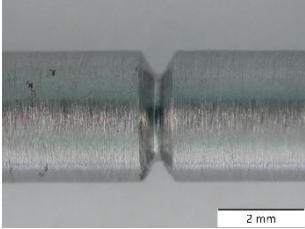
K55 notched, 25°C	dry	200 g/l [NaCl]
Gas A		
Gas B		
Gas C		
Gas D		
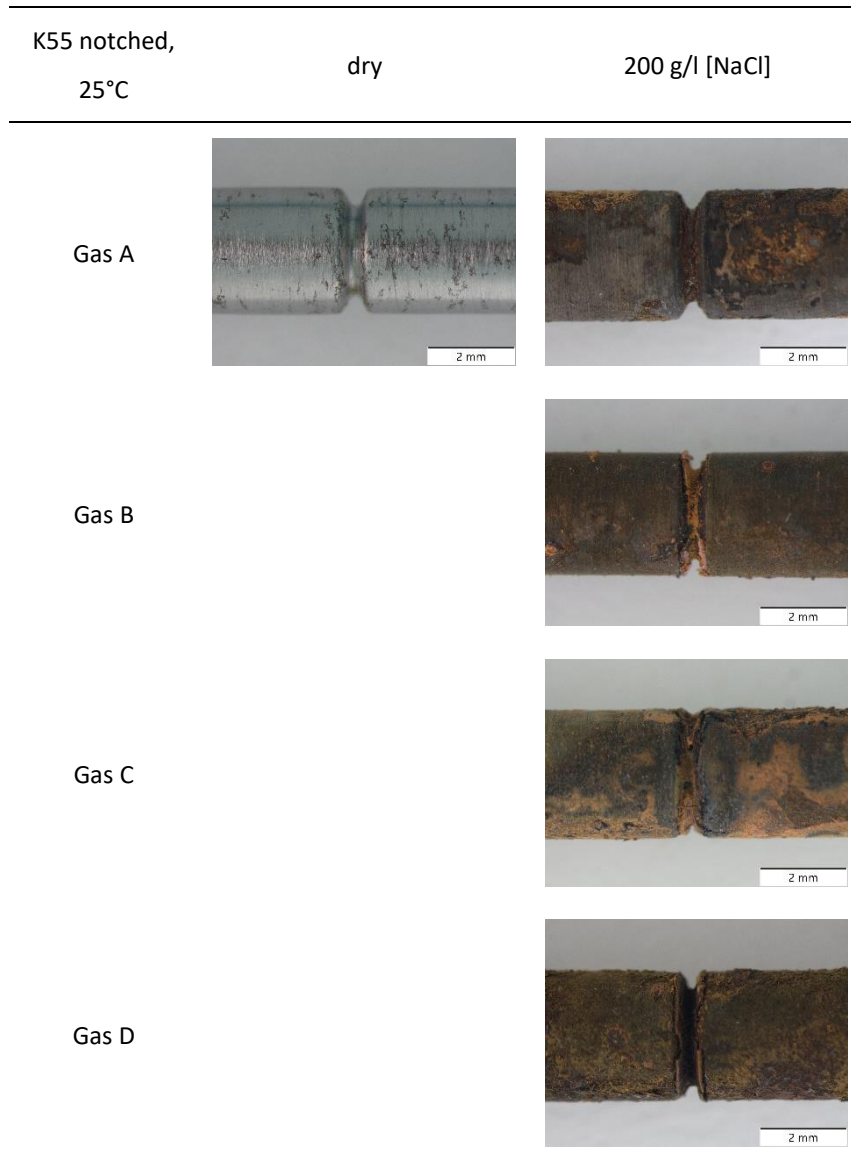
Table 20: Stereo microscope images of the pre-corroded steel K55 in different gases with and without an electrolyte at RT

K55 pre-corroded, 25°C	dry	200 g/l [NaCl]
Gas A		
Gas B		
Gas C		
Gas D		
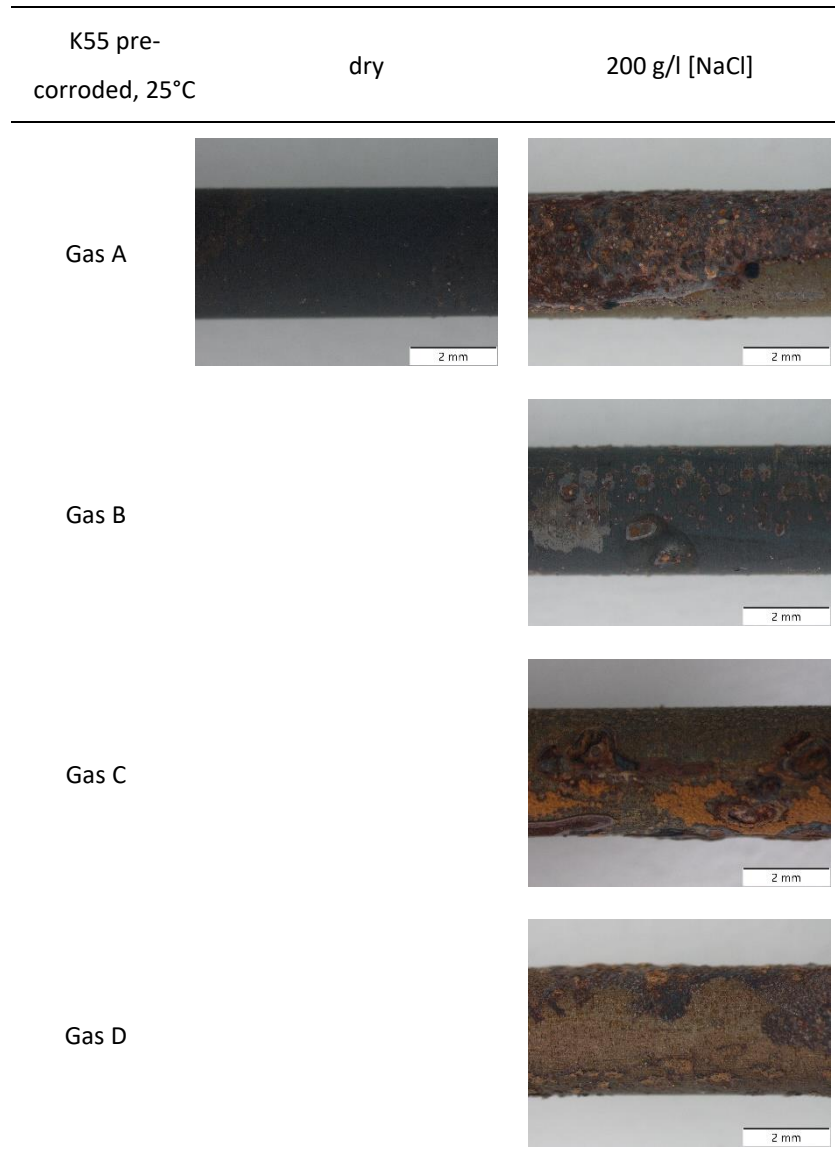
Table 21: Stereo microscope images of the welded steel K55 in different gases with and without an electrolyte at RT
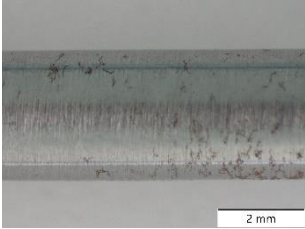
welded K55, 25°C	dry	200 g/l [NaCl]
Gas A		
Gas B		
Gas C		
Gas D		

Table 22: Stereo microscope images of the steel L80 in different gases with and without an electrolyte at RT
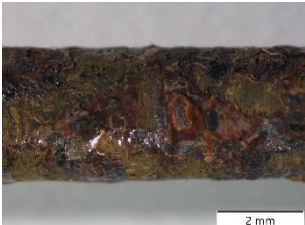
L80, 25°C	1 g/l [NaCl]	200 g/l [NaCl]
Gas A		
Gas B		
Gas C		
Gas D		

Table 23: Stereo microscope images of the steel L80 in different gases with and without an electrolyte at 120 °C
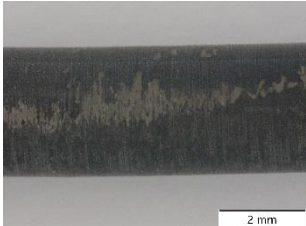
L80, 120°C	1 g/l [NaCl]	200 g/l [NaCl]
Gas A		
Gas B		
Gas C		
Gas D		

Table 24: Stereo microscope images of the steel L80 with a notch in different gases with and without an electrolyte at RT
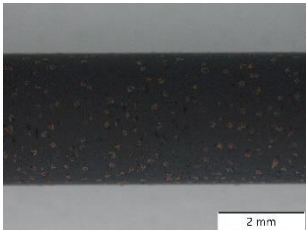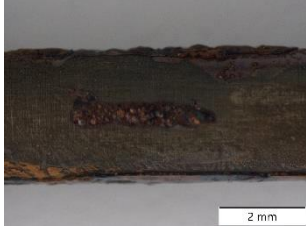
L80 notched, 25°C	dry	200 g/l [NaCl]
Gas A		
Gas B		
Gas C		
Gas D		

Table 25: Stereo microscope images of the pre-corroded steel L80 in different gases with and without an electrolyte at RT

L80 pre-corroded, 25°C	dry	200 g/l [NaCl]
Gas A		
Gas B		
Gas C		
Gas D		